

LEARNING AND APPLYING MATERIAL-BASED SENSING
LESSONS FROM NATURE

A Dissertation
Presented to
The Academic Faculty

by

Michael Edward McConney

In Partial Fulfillment
of the Requirements for the Degree
Doctor of Philosophy in the
School of Polymer, Textile, and Fiber Engineering

Georgia Institute of Technology
August 2009

LEARNING AND APPLYING MATERIAL-BASED SENSING
LESSONS FROM NATURE

Approved by:

Dr. Vladimir V. Tsukruk, Advisor
School of Polymer, Textile, and Fiber
Engineering
Georgia Institute of Technology

Dr. Yonathan S. Thio
School of Polymer, Textile, and Fiber
Georgia Institute of Technology

Dr. Meisha Shofner
School of Polymer, Textile, and Fiber
Engineering
Georgia Institute of Technology

Dr. Marc Weissburg
School of Biology
Georgia Institute of Technology

Dr. Mohan Srinivasarao
School of Polymer, Textile, and Fiber
Engineering
Georgia Institute of Technology

Date Approved: June, 29, 2009

“The point is to develop the childlike inclination for play and the childlike desire for recognition and to guide the child over to important fields for society. Such a school demands from the teacher that he be a kind of artist in his province”

-Albert Einstein

This is dedicated to my teacher, Vladimir. You taught me to be a scientist. You pushed me to make something of myself. Without you I would have continued to struggle for meaning and direction in life.

ACKNOWLEDGEMENTS

First, I would like to thank the love of my life, Stephanie; you are the thread that ties my life together. Madeline, thank you for bringing so much joy to my life, I love you. Mom and Dad, you both shaped me into the person I am, thanks for your love, encouragement, and strong example. Catherine, you are a great sister and a great aunt, your undying love, forgiveness, pride and loyalty for me, although undeserved, has been a source of solace during some of my tougher times, thank you. Sandra, your help for the past year has been truly invaluable, thanks. Thanks to the rest of my family and friends.

I would also like to thank Prof. Tsukruk, who pushed me to overcome my deficiencies. Special thanks goes to my dissertation committee, Prof. M. Srinivasarao, Prof. M. Shofner, Prof. Y. Thio, Prof. M. Weissburg, and Prof. J. Yen for providing very useful constructive criticism and insight.

My special thanks to the SEMA Group, especially Dr. S. Peleshanko, Dr. M. Ornatska, Dr. M. Julian, Prof. C. Jiang, Dr. M. Lemieux, Mr. K. Anderson, Mr. D. Lu, Prof. S. Singamaneni, whose participation in this work was critical. I would also like to thank all my collaborators, with whom this work would not be possible; thanks to Prof. F. Barth, Mr. C. Schaber, Prof. S. Coombs, Prof. J.A.C. Humphrey, Mr. W.C. Eberhardt, Prof. C. Liu, Dr. N. Chen, Mr. A. Hu, Mr. C. Tucker, Dr. Y. Yang, Prof. D.H. Reneker, Dr. T. Han. I would also like to thank Prof. V. Milam and B. Baker for technical assistance with rheological measurements and Prof. V. Breedveld for useful discussions. My thanks also go to the following agencies for supporting this work: DARPA, AFOSR, AFRL, and NSF.

TABLE OF CONTENTS

ACKNOWLEDGEMENTS	iv
LIST OF TABLES	ix
LIST OF FIGURES	x
LIST OF SYMBOLS AND ABBREVIATIONS	xiii
SUMMARY	xviii
CHAPTER 1 INTRODUCTION	1
1.1 Flow and Vibration Sensing Background	5
1.1.1 Flow Sensors	6
1.1.2 Flow Sensing in Fish	8
1.1.3 Vibration and Flow Sensing in Spiders	14
1.1.3.1 Vibration Sensing in Spiders	15
1.1.3.2 Air-Flow Sensing in Spiders	17
1.2 Photo-thermal Sensing Background	20
1.2.1 Thermal-based Infrared Imaging	20
1.2.2 Thermal Sensing of the Fire Beetle	22
1.3 Background Synopsis	25
CHAPTER 2 GOALS, OBJECTIVES AND OVERVIEW	26
2.1 Goals	26
2.2 Specific Technical Objectives	27
2.3 Dissertation Overview	28
CHAPTER 3 MATERIALS AND METHODS	32
3.1 Atomic Force Microscopy	32
3.2 Force Spectroscopy for the Mechanical Characterization of Polymers	34
3.2.1 Force-distance Curves and Mapping	35
3.2.2 Force Spectroscopy Calibrations	37
3.2.2.1 Calibrating the Photodiode Sensitivity	37
3.2.2.2 Measuring Cantilever Spring Constants	39
3.2.2.3 Tip Radius Measurements	41
3.2.3 Elastic Modulus and Contact Models	42
3.3 Electrospinning	44

3.4 Layer-by-Layer deposition	45
3.5 Other Methods	46
CHAPTER 4 SPIDER VIBRATION RECEPTOR STUDY	47
4.1 Introduction	47
4.2 Materials and Methods	49
4.3 Results and Discussion	51
4.3.1 Receptor Pad Surface Topography	51
4.3.2 Receptor Pad Force-Spectroscopy	53
4.3.3 Receptor Pad Elastic Modulus	55
4.3.4 Receptor Pad Frequency Response	57
4.4 Conclusion	62
CHAPTER 5 SPIDER AIR FLOW RECEPTOR STUDY	63
5.1 Introduction	63
5.2 Materials and Methods	65
5.2.1 Sample Preparation	65
5.2.2 SFS-Hair deflection Measurements	66
5.2.3 Theoretical determination of the viscoelastic model parameters	71
5.2.3.1 Two-parameter Kelvin solid model	71
5.2.3.2 Three-parameter solid model	73
5.2.4 Testing Methodology: Nanoshaving	74
5.2.5 Testing Methodology: Location of the axis of rotation	75
5.2.6 Testing methodology: Deflection of a rigid hair	77
5.3 Results	78
5.3.1 Measuring the torques resisting hair motion	78
5.3.2 Viscoelastic model parameters	81
5.4 Discussion	86
5.4.1 Comparison with fluid mechanic modeling studies	86
5.4.2 Modeling of the viscoelastic hair suspension	88
5.4.3 Sources of hair suspension viscoelasticity	90
5.4.4 Biological relevance	91
5.4.5 Relevance to Bio-inspired Materials Approaches to Sensing	93

5.5 Conclusion	95
CHAPTER 6 BIO-INSPIRED MATERIAL FOR FLOW SENSING	96
6.1 Introduction	96
6.2 Materials and Methods	98
6.2.1 Fish Preparation and Care	98
6.2.2 Force-Spectroscopy	99
6.2.3 Artificial Cupula Preparation	99
6.3 Results and Discussion	100
6.3.1 Fish Cupula Material Study	100
6.3.2 Fish Inspired Artificial Cupula	101
6.3.2.1 Development of Artificial Cupula Material	101
6.3.2.2 Artificial Cupula Material Study	103
6.3.2.3 Sensing Performance of Artificial Cupula	104
6.4 Conclusion	108
CHAPTER 7 BIO-INSPIRED STRUCTURE FOR FLOW SENSING	109
7.1 Introduction	109
7.2 Materials and Methods	112
7.2.1 Fish Cupula Aspect Ratio	112
7.2.2 Controlled Drop Casting for Hydrogel Shape Control	113
7.3 Results and Discussion	117
7.4 Conclusion	119
CHAPTER 8 CUPULA ARRAYS AND FIBRILS FOR FLOW SENSING	120
8.1 Introduction	120
8.2 Materials and Methods	122
8.2.1 Hair Substrates	122
8.2.2 Shape Control and Patterning	122
8.2.3 Electrospinning	123
8.3 Results and Discussion	126
8.3.1 Cupula Shape Control	126
8.3.2 Electrospun Fibrils and Cupula Aspect Ratio	130
8.4 Conclusions	134

CHAPTER 9 FIRE-BEETLE INSPIRED PHOTO-THERMAL SENSING	135
9.1 Introduction	135
9.2 Materials and Methods	137
9.2.1 Layer-by-Layer Deposition	137
9.2.2 Interferometry-based Transduction	139
9.3 Results and Discussion	141
9.3.1 Thermal-Pneumatic IR-Imagers	141
9.3.2 Polymeric Thermal-Buckling Based Sensor Arrays	145
9.4 Conclusion	151
CHAPTER 10 GENERAL CONCLUSIONS AND BROADER IMPACT	152
10.1 Summarized Specific Conclusions	152
10.2 General Conclusions	155
10.3 Significance and Broader Impact	157
10.4 Refereed Publications and Information Directly Related to this Dissertation	160
10.5 Other Relevant Publications	161
10.6 Oral Presentations Related to Dissertation	162
REFERENCES	163
VITA	186

LIST OF TABLES

	Page
Table 5.1: Experimental Conditions for SFS Measurements	71
Table 5.2: Angular velocity $\dot{\theta}$, torque T , and torque rate of change \dot{T} (mean \pm <i>r.m.s.</i> values) for a shortened trichobothrium originally 950 μm long at a deflection angle fixed to $\theta_{tot} = 1.226 \times 10^{-3}$ rad (N=1, n=81) ¹	84

LIST OF FIGURES

	Page
Figure 1.1: The Micro-fabricated Flow Sensors.	7
Figure 1.2: A Schematic of the Lateral Line System.	9
Figure 1.3: A Schematic of a Hair Cell.	11
Figure 1.4: Blind Cave Fish Neuromast Schematic.	13
Figure 1.5: The Wandering Spider.	14
Figure 1.6: A Schematic of the Slit Sense Receptor	16
Figure 1.7: Trichobothria	18
Figure 1.8: Trichobothria Transduction Physiology and Response	19
Figure 1.9: The Golay Cell	21
Figure 1.10: The Fire Beetle	22
Figure 1.11: Fire Beetle Sensing	23
Figure 2.1: Aiming to combine Materials Science, Biology, and Sensor Engineering	26
Figure 3.1: Schematic of a Sample Scanning AFM System	32
Figure 3.2: Force-Distance Curves	36
Figure 3.3: Cantilever Spring-on-Spring Constant Calibration	39
Figure 4.1: The Wandering Spider Vibration Receptor and Associated Pad	48
Figure 4.2: The Receptor Pad Surface	52
Figure 4.3: Characteristic Force-distance Curve	53
Figure 4.4: Stiffness and Young's Modulus Histograms	56
Figure 4.5: Force-distance and Load-penetration with Probing Frequency	58
Figure 4.6: The Correlation between Elastic Modulus and Nervous Response	59
Figure 4.7: Schematic of Pad Signal Filtering	61

Figure 5.1: The Spider and Trichobothria	66
Figure 5.2: Hair Shaft Morphology	69
Figure 5.3: Hair Parameters used for the Calculations	70
Figure 5.4: “Spring” and “dashpot” Representations	72
Figure 5.5: Hair Shaving	75
Figure 5.6: Locating the Pivot Position	76
Figure 5.7: Hair Shaft Bending	79
Figure 5.8: High Resolution Hair Shaft Deflection Measurements	81
Figure 5.9: Dependency of Load-Deflection and Work on Angular Velocity	82
Figure 5.10: Comparison of Measurements and Empirical Fits	83
Figure 5.11: Comparison between Measurements and Models	85
Figure 5.12: Hair Response to Natural Stimuli	88
Figure 5.13: Relevance to Sensor Engineering	94
Figure 6.1: The Fish Lateral Line, Neuromasts and Bio-inspired Sensors	97
Figure 6.2: Fish Cupula Material Testing	100
Figure 6.3: Artificial Cupula Fabrication	102
Figure 6.4: Comparison of Load-Penetration ^{3/2} of Fish Cupula and Artificial Cupula	103
Figure 6.5: The Performance of The Dome-shape Cupula	105
Figure 7.1: The High Aspect Ratio Superficial Cupula	111
Figure 7.2: Precise Drop Casting	114
Figure 7.3: High Aspect Ratio Artificial Cupula	116
Figure 7.4: Testing of the High Aspect Ratio Artificial Cupula	117
Figure 7.5: The Performance of the High Aspect Ratio Cupula	118
Figure 8.1: An Array of Neuromasts, Cupula Fibrils and Anisotropic Cupula	121
Figure 8.2: The Electrospinning Setup	125

Figure 8.3: An Elliptical Shaped Cupula	127
Figure 8.4: A Crescent Shaped Cupula	128
Figure 8.5: Parallel Fabrication of Multiple Cupula	129
Figure 8.6: Conventionally Electrospun Fibers onto a SU-8 Hair	131
Figure 8.7: Schematic Showing Effect of Biased Coils on the Electric Field	132
Figure 8.8: The Cupular Fibrils and Cupula Supported by Fibrils	133
Figure 9.1: The Fire Beetle Photo-thermal Receptor	136
Figure 9.2: The chemical structure of polyions used to make LbL films	138
Figure 9.3: Membrane Fabrication Process	138
Figure 9.4: Membrane Interferometer Testing	140
Figure 9.5: Thermal-pneumatic IR Sensing	142
Figure 9.6: Cooling Induced Buckling	144
Figure 9.7: Pneumatically-Guided Out-of-Plane Buckling	146
Figure 9.8: Thermal-Buckling Transduction Experimental Schematic	147
Figure 9.9: The Fast Response of the Thermal-Buckling	148
Figure 9.10: Response of Thermal-Buckling Sensors	150

LIST OF SYMBOLS AND ABBREVIATIONS

AFM	atomic force microscopy
B	hair bending distance
BBM	buckling-based metrology
BCF	blind cave fish
cm	centimeters
C	constant
C_B	cantilever deflection in hair bending regime
C_D	cantilever deflection in hair deflection regime
D	hair deflected length
D_c	cupula diameter
d	center deflection
d_h	hair diameter
E	elastic modulus
E_S	sample elastic modulus
E_T	tip elastic modulus
E'	composite modulus
F	drag force
Fig	figure
f-d	force-distance
f-v	force-volume
F_{cup}	cupula drag force
F_{hair}	hair drag force
FFT	fast-Fourier transform

GNP	gold nanoparticles
GPa	giga-Pascal
h	sample vertical penetration distance
h_h	hair height
H_c	cupula height
Hz	Hertz
I	moment of inertia
IR	infrared
J	Joules
JKR	Johnson-Kendall-Roberts
k	cantilever spring constant
k_B	Boltzmann constant
kHz	kilo-Hertz
k_{known}	known cantilever spring constant
k_M	materials stiffness
k_{unknown}	unknown cantilever spring constant
kPa	kilo-Pascal
k_1	transduced cantilever spring constant
k_2	sample cantilever spring constant
L	Length from pivot-axis to probe tip
LbL	Layer-by-layer
mg	milligramss
mL	milli-liters
mm	millimeters

mV	millivolts
mW	milli-Watts
MPa	mega-Pascal
Mw	molecular weight
nm	nanometer
nN	nano-Newton
P	applied force
Pa	Pascal
PAH	poly(allylamine hydrochloride)
PCL	polycaprolactone
PDMS	polydimethylsiloxane
PEG	poly(ethylene glycol)
PEG-TA	poly(ethylene glycol) tetra-acrylate
pN	pico-newton
PSS	poly(sodium 4-styrenesulphonate)
r	tip-surface contact radius
R	damping constant
rad	radians
ref	reference
r.m.s.	root mean squared
R_{2p}	2 parameter damping constant
R_{3p}	3 parameter damping constant
R_T	tip radius
S	torsional constant
S_{2p}	2 parameter torsional constant

S_{3p}	3 parameter torsional constant
S_{3p}'	3 parameter torsional constant
s	second
sec	seconds
SEM	scanning electron microscopy
SPM	scanning probe microscopy
SFS	surface force spectroscopy
t	film thickness
T	torque
\dot{T}	rate of change of torque
TCB	trichobothria
U	fluid flow velocity
UV	ultraviolet
wt.	weight
WS	wandering spider
Z_{defl}	cantilever deflection distance
Z_{defl1}	transduced cantilever deflection distance
Z_{defl2}	sample cantilever deflection distance
Z_{pos}	vertical piezo position displacement
2p	2 parameter
3p	3 parameter
μL	microliter
μm	micrometer
μ	dynamic fluid viscosity
θ	angular deflection

$\dot{\theta}$	angular velocity
$\ddot{\theta}$	angular acceleration
θ_{Tot}	total angular deflection
ν	Poisson's ratio
ν_S	Sample Poisson's ratio
ν_T	Tip Poisson's ratio
$^{\circ}\text{C}$	degrees Celsius
$^{\circ}\text{K}$	degrees Kelvin

SUMMARY

The work presented in this dissertation was aimed at understanding biology's application of soft materials to enhance sensing abilities and initiate innovative bio-inspired material-based approaches for flow (fluidic and air) sensors and photo-thermal sensors. A key aim is to help strengthen this niche of functional materials science referred to, here, as bio-inspired materials in sensing roles. The work aspires to traverse the boundaries of the subject in order to provide a strong foundation for future scientific explorations of the subject. The studies presented here, include studies of flow sensing in fish and implementing a bio-mimetic approach to microfabricated flow sensors. The work also includes studies of material based signal filtering in spiders, as well as, bio-inspired photo-thermal transduction mechanisms. The capabilities of the methodology are demonstrated with successful engineering studies.

CHAPTER 1

INTRODUCTION

Biologically inspired design is a non-traditional problem solving approach which often results in uniquely engineered solutions for complex practical problems. Furthermore, this approach can often work to catalyze development through the use of a bi-directional approach to problem solving, where both the problem and potential solutions are analyzed simultaneously.^{1,2} Through, analyzing and hypothesizing the role of functional physiology, engineered design approaches can often be stimulated. Bio-inspirational design can be likened to reverse-engineering. Essentially, one should probe the structural and functional design principles of the biological examples to help develop a design for an engineered system. A successful bio-inspired design should understand and implement the important biological principles and strategies. Furthermore, by understanding the principles and strategies employed by the biological system one can tailor these principles towards an engineered system, instead of simply replicating the biological lessons. There are many examples of the successful application of bio-inspired design, the inch-worm inspired piezoelectric inchworm motor,³ materials capable of legless motion inspired by the anisotropic friction of snake locomotion,^{4,5} inorganic crystallization that mimics the formation of the skeletons of sponges,^{6,7,8} the ability to defy gravity by walking on walls inspired by the setae of geckos,^{9,10,11} micro-lenses inspired by brittlestars,^{12,13} and adhesive materials inspired by mussels.^{14,15} Greater understanding in broad fields has also been gained with the use of bio-inspiration including materials fabrication,¹⁶ locomotion,¹⁷ and signal processing.¹⁸

Although, there are many examples of success stories involving bio-inspired design, the rules and the methods of this approach are still evolving. Nonetheless, it seems quite apparent that the exploration of biological ingenuity and the inspiration of engineering design is a symbiotic relationship. In order to fully leverage this bi-directional approach it is important to understand the fundamental differences in the approach to problem solving and differences in their inherent constraints to design. Generally, nature's approach is to continuously improve past designs and make changes to solve new challenges; whereas engineers, often literally start their designs from the drawing board.^{1,2} Biology often uses the same tools with small changes for very different roles and these small changes can often be very insightful as to the particular specialization of a system.

Natural selection fuels design by using natural heritable variations to solve new problems. If a small heritable variation enhances an animal's ability to survive, then that animal has a better chance of reproducing. Then multiple offspring having inherited that new varied trait also have a better chance of survival and reproduction, therefore leading to exponential growth of the new trait. Therefore, it should be evident that survival and reproduction are key components to problem solving in biology.¹⁹ Through just a simple analysis of the amazing capabilities of biology it is quite evident that this strategy is quite powerful.^{20,21} It should be straightforward to think that man could learn quite a bit by looking to biology's billions of years of experience in designing solutions. Modern manufacturing strategy is aimed at eliminating any variations to engineered products.²² Furthermore, manufactured products rarely, if ever, are used to manufacture the same product. In other words, modern manufacturing implements production, not reproduction

(in the biological sense). By that fact, the survivability of a product does not have a direct effect on the future products manufactured. Natural selection leads to a design scenario where solutions are designed and manufactured simultaneously, whereas engineered manufacturing generally has a separate design and manufacture stage.

There are major differences in the constraints facing design development in nature and man. Biology faces some stringent constraints on designing solutions. All designs in nature must evolve from slight random variations on previous designs to develop a new solution. These random variations are mostly limited by heredity. Complex systems to grow, reproduce, function and survive in a complex world have been developed by biology and these systems severely limits new solutions because the chance that a variation will interfere with one of these previous developments is quite high.² Man on the other hand, has very few design constraints. Essentially, it could be said that man's designs are limited by physics, resources, and ingenuity. Despite man's ability to design something revolutionary, limited resources and limited ingenuity are often quite restrictive for humans design.² Keeping these differences of design approach and constraints in mind, in this dissertation I have focused on using bio-inspiration to help guide the design process of engineering design by enhancing human ingenuity.

Specifically, the research contained in this thesis is aimed at developing novel ways to apply functional soft materials to fulfill roles in sensing. This research depended on the insight offered by different biological systems. Appropriate biological systems were primarily selected based on the relevance to the particular problem that we were interested in solving, the availability of literature and logistical issues were also considered. Much of the biological clues came from sensory biology literature, but

several biological studies were conducted to test hypotheses and aid in the design of engineered solutions. In order to enhance underwater flow sensing abilities with a material-based approach we looked to blind cave fish for inspiration. Blind cave fish were chosen because of their reported hydrodynamic imaging abilities. Furthermore, by having to adapt to an environment with little to no light they seem ideal specimens in search of specializations that would enhance hydrodynamic imaging capabilities. Wandering spiders were chosen to investigate novel approaches to apply materials in passive signal processing roles. The Wandering spiders depend on vibrational information for prey-detection and reproduction, but yet have relatively simple nervous systems. Therefore, spiders were investigated to gain insight into their ability to cope with large amounts of sensory information with a relatively simple nervous system. In fact these spiders have already demonstrated novel structural approaches to signal filtering. The spiders were also investigated because these arachnids were well studied by our collaborator, Prof. Barth, whose insight and experience was invaluable. Literature related to infrared imaging and sensing in biology was investigated with a focus on fire-beetles because they use a thermal-mechanical approach which is highly suited to inspiring a polymeric-based transduction, unlike some other infrared sensing approaches, which are more likened to thermal-electrical transduction. Furthermore, the fire-beetle's infrared pit sensing organ was researched to better understand the receptors' seeming ability use thermal-pneumatic transduction that has high-sensitivity and a very small footprint, which will hopefully provide clues to improve current engineered thermal-pneumatic based infrared sensors.

1.1 Flow and Vibration Sensing Background

Sound is essentially pressure fluctuations in a transmitting medium accompanied with an oscillation of the medium particles, which is created by things moving or vibrating in the surrounding environment, as well as other energetic phenomena. Therefore, it is no surprise that sound is a ubiquitous phenomenon, with broad sweeping importance as an environmental cue. Although, sound can travel through all forms of matter, including plasma, important environmental sounds usually travel through the ground, the air, or the water. The importance of hearing sounds is emphasized by the fact that there is no evidence of any vertebrates that lived without hearing.²³ Hearing serves a critical role in predator avoidance and prey detection, especially because it always watchful and monitors the environment beyond the line of sight. Sound is fairly easy for animals to create and therefore, hearing also plays a crucial role in communication, which is important for reproductive purposes, social group purposes.²³

This dissertation includes work associated with a relatively large project motivated to develop a compact flow-visualization system that is capable of acting as a passive sonar system for a variety of application including guidance of autonomous underwater vehicles (AUVs). It should be apparent that this is no small task. It involves developing a suitable flow visualization system and developing signal processing techniques. Some of the work presented in this dissertation involves supporting these efforts through the investigation of biology and development of new approaches using materials-based knowledge and techniques.

1.1.1 Flow Sensors

The overall motivation for the flow sensor project is to develop a compact flow-visualization system that is capable of acting as a passive sonar system for a variety of applications, including guidance of autonomous underwater vehicles (AUVs). Although the major focus is on underwater sensing capabilities, aerial sensing capabilities are also important for applications such as unmanned aerial vehicles (UAVs).

Flow measurement is a very basic area of measurement, capable of utilizing many different physical relationships.^{24,25} Although, flow measurement is basic, flow visualization, the 2D and 3D imaging of flow fields (velocity and/or vorticity fields), is not so simple. Typically, hydrodynamic visualization is used for experimental fluid dynamics studies, but there are many other applications including navigation and obstacle avoidance of autonomous underwater vehicles, underwater surveillance, seismic monitoring to mitigate tsunami-related loss, oceanographic studies, mine reconnaissance, monitoring pollution, drag-minimization of submarines, passive sonar, wake-following and many other applications.^{26,27} An in-depth description of flow-visualization is beyond the scope of this dissertation, see relevant reviews for a fuller summary.^{28,29}

The current work involves developing a surface-based flow visualization system composed of an array of mechanical-based flow sensors. A major advantage over this technique compared to more common bulk-based (free-flow) techniques, such as Doppler shift, is the highly passive nature. A major disadvantage is that the sensing is taking place near the stagnant boundary layer of the surface, which significantly increases the need for very sensitive sensors that still do not considerably interfere with the flowing environment.

The flow sensors system is currently based on a sensor system developed by and fabricated by Prof. Chang Liu and his group at Northwestern University. They have gone through several different designs over more than 6 years^{.30,31,32,33,34,35,36}

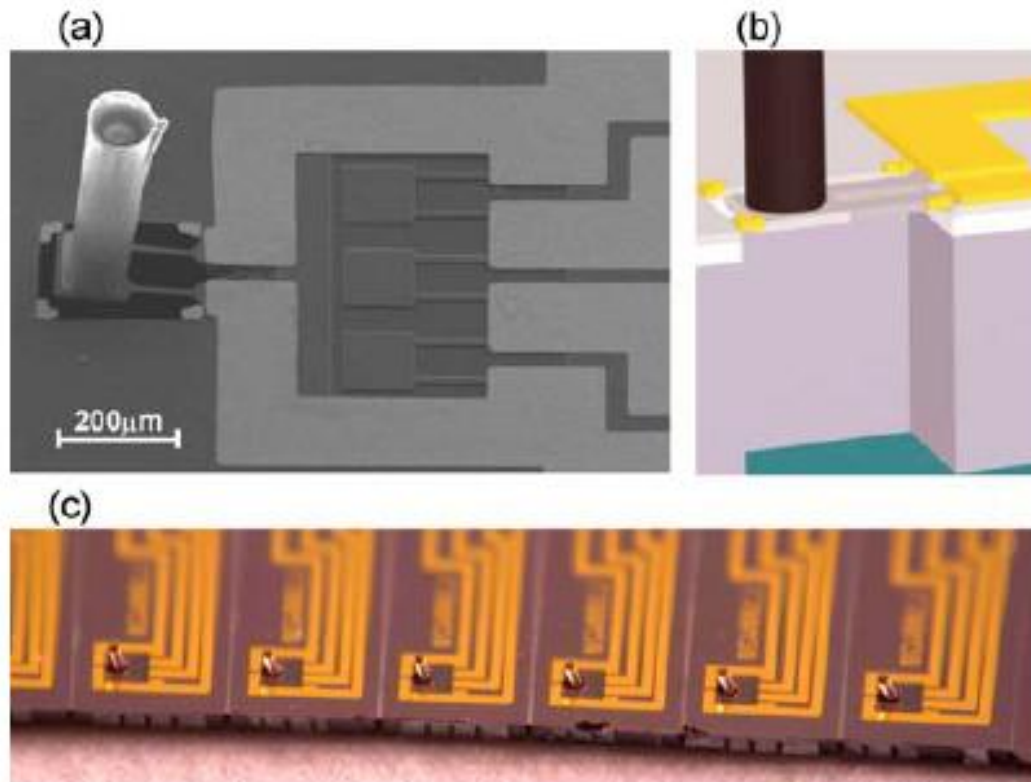


Figure 1.1: The Micro-fabricated Flow Sensors. A) SEM micrograph of pre-existing flow sensors, showing the piezo-resistive circuit with the associated Wheatstone bridge B) Schematic of flow sensors C) An array of flow receptors for flow-based imaging (From Reference 33)

The sensors, shown in figure 1.1, are mechanical-based piezoresistive hair sensors that were inspired by fish flow lateral line flow receptors.³³ The current sensors consist of an SU-8 hair on a silicon-based microcantilever with a gold circuit patterned on the silicon surface. The whole sensor is covered in parylene, which water proofs the sensor by acting as a pin-hole free dielectric. The hair on the sensors absorbs mechanical energy from the surrounding water flow, which is transmitted to the adjacent cantilever. The cantilever bends in response to the hair-transmitted mechanical energy and the flow-

derived signal is transduced through a bending-induced resistance change of the circuit embedded in the cantilever. These sensors have a water flow optimum minimum detection threshold of 0.1 mm/s, which is considered too low to accomplish the ambitious goals of this project.³³ Maximizing the sensitivity and minimizing the detection threshold is very important for many reasons including maximizing the distance that the system can “see” and maximizing the distance between sensors, which has signal processing implications. Another major issue is that the signal processing load from an array of these sensors requires hardware that is not considered portable.

1.1.2 Flow Sensing in Fish

Fish rely on flow and vibration receptors for navigation, hunting prey, schooling and other functions. It is relatively well-known that certain fish species that are blind or have been blinded have been able to still avoid collisions with stationary objects.^{37,38} Behavioral studies on blind cave fish have shown that these fish are able to detect the location of bars on grids with spacing as small as 1.5mm with 70% certainty.³⁸ The ability of fish to measure water motion is quite impressive. In general, fish are able to sense water flow with minimal velocities on the order of $\mu\text{m/s}$.^{39,40} Measurements have shown that the lateral line is quite sensitive to the local flowing environment.⁴¹

This work aims to better understand the design that endows fish with high-sensitivity and low minimum threshold detection to water flow. The lateral line system is a series of pores and canals in the head and along the body of fish that contain neuromasts, which are the basic flow sensing unit in fish (figure 1.2).⁴²

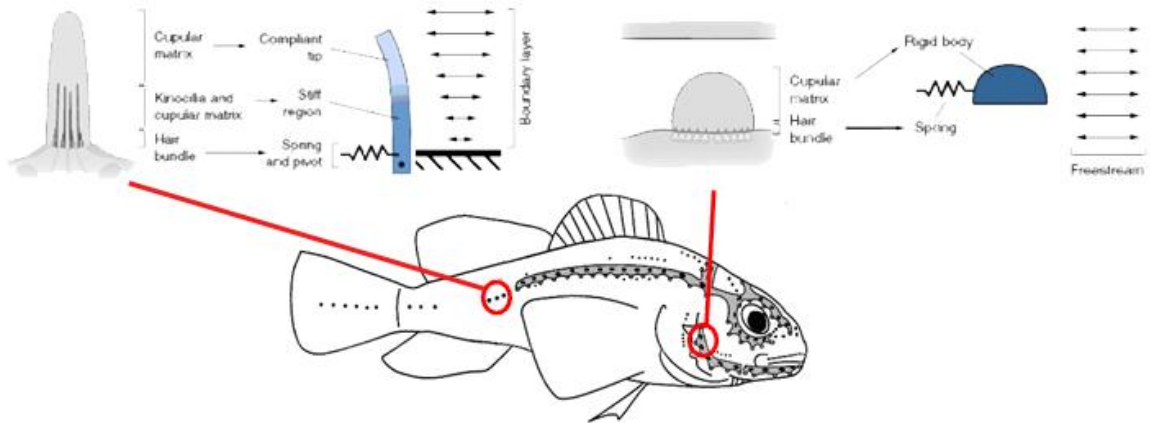


Figure 1.2 A Schematic of the Lateral Line System. Top left: Superficial neuromasts are situated on the outside surface of the fish and undergo a bending deformation. Top right: Canal neuromasts are below the surface of the fish in tunnels and depressions. They respond to stimuli by sliding along their surface. (Adapted from Reference 27 and 43)

A neuromast is composed of a dense localized area of mechanosensing hair cells and support cells covered by a single hydrogel-like cupula. There are usually ~50 – 1000 hair cells per a neuromast.⁴⁴ Neuromasts are located on the surface extending into the water (superficial neuromasts) and in the lateral line of the fish (canal neuromasts).⁴⁵ The diameter of the superficial neuromasts is generally below one hundred micrometers, which is much smaller than the canal neuromasts that grow up to several hundred micrometers. The superficial neuromast cupula bend and deflect in response to stimuli (figure 1.2). The canal cupulae are semi-rigid structures that slide across surface of the canal in response to stimuli (figure 1.2). Superficial neuromasts tend to be more sensitive to flow velocity, whereas the lateral line neuromasts are more sensitive to acceleration.⁴⁴ The frequency sensitivity of these receptors likely comes from the canal, boundary layer at the surface, and the structural behavior of the cupula.

The mechanosensing hair cells have asymmetric hair bundles that usually grow in pairs of opposite orientation. The hair cell of neuromasts have a single long hair, shown in detail Figure 1.3, that are called kinocilium and a series of the shorter hairs are called stereovilli.⁴⁶ The kinocilium acts to support the hair bundle, transmit stimuli, and is capable of exerting an opposing force on the hair bundle in response to stimuli, essentially acting as a component of a feedback mechanism, which keeps the cell sensitive to minute stimuli while preventing signal saturation from large stimuli. The stereovilli are small cellular protrusions that occur in bundles. The tips of the stereovilli within a hair bundle are connected via protein linkages. One end of the linkage is connected to a mechanically gated ion channel (or valve).⁴⁷ The tip-linkage act to transmit mechanical stimuli to the ion channel, which opens in response to stress. Upon opening ions pass into the cell, thereby setting off an action potential. The other end of the tip linkage is connected an adjacent stereovilli. A motor protein allows the tension between the stereovilli to change, which is also a component of the cellular feedback mechanism.⁴⁸

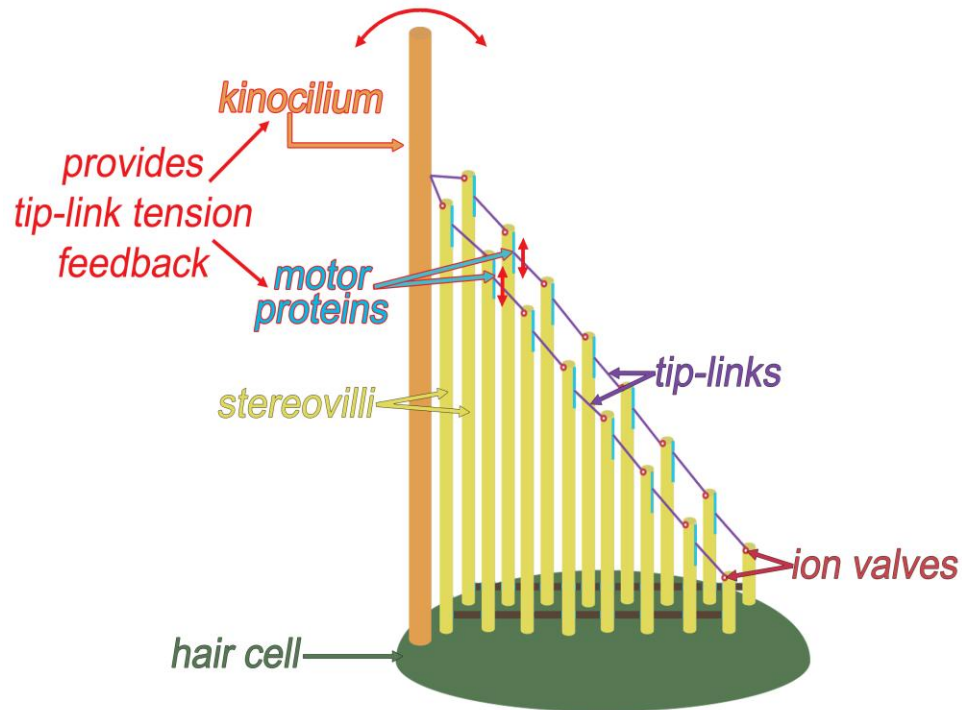


Figure 1.3: A schematic of the Hair Cell. (kinocilium not to scale)

It should be apparent that the hair cell is quite complex and amazing. The asymmetry of the hair bundles imparts the hair cell with a directional response to stimuli. If the flow is in the direction, such that the stereovilli are bent towards the kinocilium, then the frequency of action potentials will increase, the opposite can also be said.⁴⁴ A full discussion of the details regarding hair-cell's complex hierarchical sensing approach and the amazing sensing capabilities can be found in several reviews.^{49,50,51,52,53,54}

It is important to note that hair-cells are not exclusively used by fish; in fact biology uses the hair cell as a ubiquitous mechano-receptor that it applies to many different mechanosensing applications. A simple example of the hair-cells ubiquitous nature is the human ear, which uses hairs cells in the vestibular system to maintain balance and hairs cells in the cochlea to sense sound. As mentioned, when implementing biological-inspired design it is important to elucidate the associated components'

functional roles in order to hypothesize and interpret probable design strategy implemented through natural selection. In this case, when comparing hair-cell receptor systems transducing different stimuli through a brief rudimentary phylogenetic analysis, the author has noticed large differences in the structures associated with the hair cell, while the actual hair cells have remained fairly similar throughout the evolutionary process. Therefore, it seems that much of the design changes and specialization were made to the structures associated with the hair cell. Therefore, the unique components associated with the hair-cell receptors of the lateral deserve particular attention to successfully implement bio-inspired design of an underwater flow sensing system.

Cupulae are usually around 100-1000 μm long, but their size and properties vary greatly.⁵⁵ Cupulae couple the mechanosensing hair cells to the surrounding water flow by essentially enhancing the drag of the neuromasts, thereby enhancing the signal to noise ratio. The cupulae enhance the drag of the neuromast through several ways, specifically these structures increase the overall surface area of the neuromast. Furthermore, the effective sensing distance from the surface of the fish is increased, which allows the fish to sense beyond the boundary layer created by the fish surface. The hydrophilicity and the porosity of hydrogel-like material that makes up the cupulae may enhance the signal to noise ratio also, through an enhanced friction factor associated with the material. Furthermore, it has been suggested that the cupula improves the signal-to-noise ratio by diminishing the effects of Brownian motion of the hair cell.⁴²

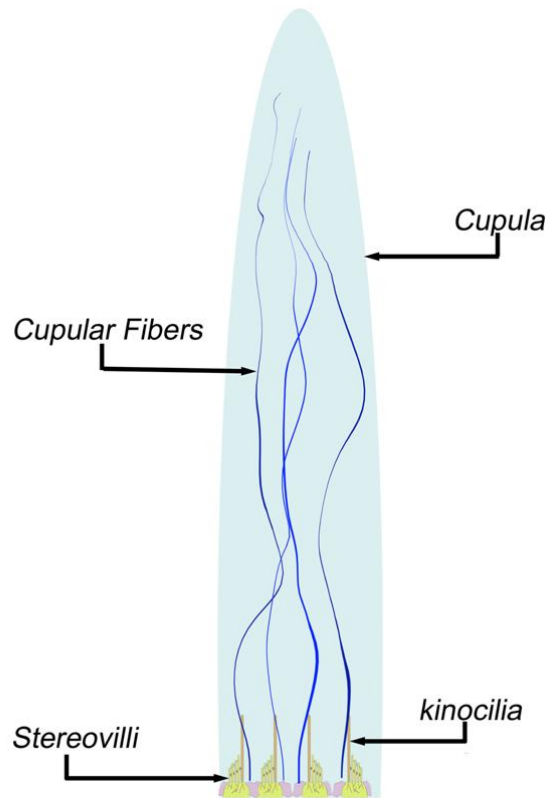


Figure 1.4: Blind Cave Fish Neuromast Schematic.

Some fish, such as blind cave fish have cupula with embedded fibrils in their superficial neuromasts, as shown in figure 1.4. It is not immediately clear why some fish have these cupular fibers and others do not. The function of these cupular fibers appears to be that it offers structural support for the cupula allowing the cupula to grow out further away from the stagnant boundary layer of the surface of the fish. These fibers may also aid in coupling the hair cells to the hydrogel cupula, essentially transmitting the energy from cupula to the hair cells.^{56,57} Through these comparative physiological comparisons, we decided to focus our bio-inspired material-based approach towards

underwater flow sensing on developing an artificial cupula for micro-fabricated underwater flow sensors.

1.1.3 Vibration and Flow Sensing in Spiders

Most spiders use webs to catch their prey, but wandering spiders (*Cupiennius*) are a genus, which do not use webs for hunting.⁵⁸ Instead, wandering spiders (WS) catch their prey through more conventional hunting methods. These spiders usually wait motionless until prey is within a few centimeters, then it attacks and supposedly they take roughly 200-700 ms to react, capture and bite the prey.⁵⁸



Figure 1.5 The Wandering Spider. (From Reference 58)

The larger species of WS have been known to occasionally eat small frogs and lizards. Much of their hunting abilities rely on their highly developed vibration sensing receptors and wind-sensing receptors. Although, wandering spiders have an exquisite

vibration sensing ability and wind-sensing ability, they have relatively simple nervous systems. Wandering spiders have brains that are roughly three times smaller than the migratory locust and almost nine times smaller than the honey bee.⁵⁸ Therefore, understanding the ability of the wandering spider to efficiently process information may inspire novel solutions to signal processing problems associated with large arrays of sensors.

1.1.3.1 Vibration Sensing in Spiders

Vibrations play an important role in the lives of spiders, which use them for prey detection, communication during courtship and other behaviors.^{59,60} The major vibration receptor organ of spiders is the slit sense organ. These slit sense organs are essentially composed of an elongated cavity or cleft embedded in the exo-skeleton. This cavity is covered by a ~250 nm thick membrane supported by cuticular ridges. These slits have lengths ranging from 8-200 μm long and widths ranging from 1-2 μm .⁵⁸ This anisotropic shape leads to a lower stiffness and preferential sensitivity to force applied perpendicular to the slit's long axis, see figure 1.6. The dendrite of the nerve cell is connected to the membrane of the slit receptor via a tubular coupling structure. These slit receptors occur in three different types of groupings, single receptors (>100 μm separating receptors), grouped receptors (<100 μm separating receptors) and so-called composite lyriform organs (<10 μm separating receptors). All lyriform organs are associated with a joint. These lyriform slit sense organs belong to a class of sensory receptors that are embedded in the spider's exoskeleton and measure the minute strains occurring due to muscle activity, haemolymph pressure, vibrations and other types of mechanical stimuli.⁵⁸ The

vibration sources are transmitted through their substrate, which are often plants of certain species.

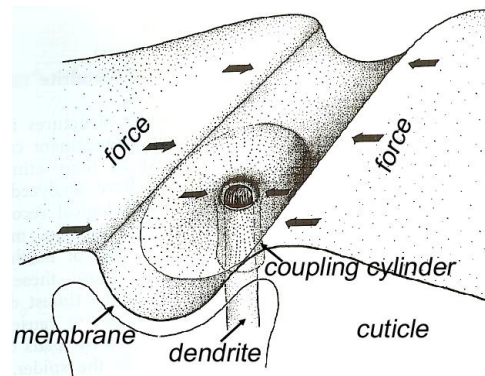


Figure 1.6: A Schematic of the Slit Sense Receptor (From Reference 58)

The metatarsal lyriform organ is a well-studied, but unique lyriform organ. It is the only lyriform organ, which is situated such that the long axis of the receptor is perpendicular with the long axis of the leg and it is positioned directly in the center of the dorsal surface of the leg. From the orientation of the slits in the metatarsal organ, it appears that it functions primarily as an external vibration sensor as opposed to receptor used to feel the leg position or movement. Slit receptors that are oriented with the long axis parallel with the long axis of the leg, are situated so that stress from muscles and haemolymph pressure efficiently deform the lyriform organs.⁵⁸ Furthermore, the metatarsal organ is the only lyriform organ situated adjacent to a large pad. The metatarsal organ is also unique in that the threshold vibrations exhibit pronounced high-pass characteristics, with low sensitivity for frequencies approximately below 30 Hz and steeply increasing threshold sensitivity at higher frequencies.^{58,61} Other than this change in sensitivity, the organs are not tuned to specific frequencies within the biologically relevant range. The dramatic change in sensitivity was found to be physiologically

important for the spider, because it provides filtering of biologically irrelevant background noise, and at the same time preserves good sensitivity to biologically relevant vibrations like vibratory courtship signals and vibrations produced by prey motion.⁵⁸

A pad cushioning the joint between the tarsus and metatarsus is located at the distal end of the metatarsus. This pad is crescent shaped and its cuticle is approximately 100 μm thick. It is believed that this pad might be a mechanical source of the physiological high-pass filtering. Substrate vibrations naturally received and transmitted by the tarsus are detected by the slits of the metatarsal lyriform organ when the proximal end of the tarsus pushes against the distal end of the metatarsus, which in turn compresses the slit receptors. Therefore, this pad seems ideally placed to mechanically filter the stimuli to the lyriform organ through frequency-dependent damping of the mechanical vibrations.

1.1.3.2 Air-Flow Sensing in Spiders

Highly sensitive trichobothria (hair receptors) air-flow receptors are a major asset to these spiders for sensing their vibrational environment. These hair receptors are found on the legs and pedipalps of the spider. The hair receptors have a large range in lengths ranging from 100-1400 μm in length, whereas the diameter of the hairs are much more similar, ranging from 5-15 μm at the base.⁵⁸ The mass of the hair is on the order of 10^{-9}g .⁶² The resonance ranges from 40-600 Hz and depends on the length of the hair and not the mass.^{63,64} The shorter hair receptors are more sensitive to velocity, whereas the longer hairs are more sensitive to acceleration.⁶⁵ Often the hairs are arranged in arrays, which are made up of hairs of differing lengths (figure 1.7). By using different length

hairs, the array of hairs is able to act as band-pass filters. This is accomplished through utilizing the stagnant boundary layer at the surface of the spider leg. This stagnant layer grows thinner at higher velocities thereby stimulating shorter hairs.⁶⁵ Therefore, by using arrays of hairs with varying lengths, the spider is able to process the stimuli through a structural-based approach before it is processed by the CNS.

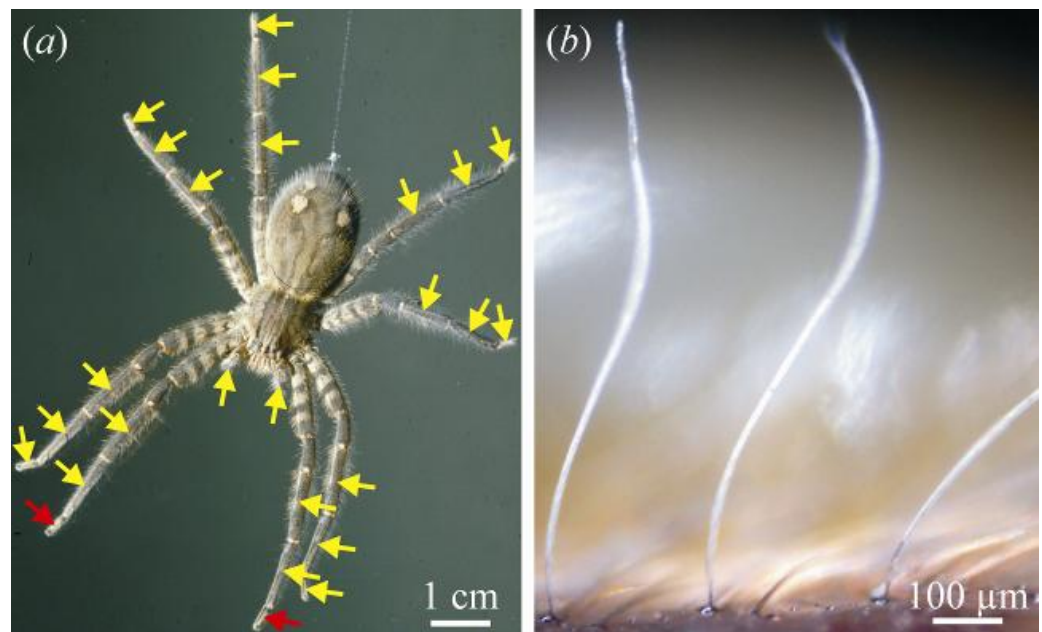


Figure 1.7: Trichobothria. a) *Cupiennius Salei* with Trichobothria locations indicated with arrows, red arrows indicate the location of hair receptors shown in b. b) An optical micrograph of trichobothria on the pedipalp.

The receptor hairs are covered with small perturbations (hairs on the hair), which decrease in length and number distally along the length of the hair. These perturbations are $1\mu\text{m}$ - $6\mu\text{m}$ in length. The perturbations increase the surface area (drag) to mass (inertia) ratio of the hair, thereby increasing the coupling between the hair and the flowing air. The hair shaft does not bend, but instead pivots about a membrane that supports the hair. When the hair pivots in response to air stimulus it deforms the nerve through a nerve coupling structure at the proximal end of the hair (figure 1.8). The

maximum bending angles of the TCB are $\sim 25^{\circ}$ - 35° , independent of the length of the hair.⁵⁸

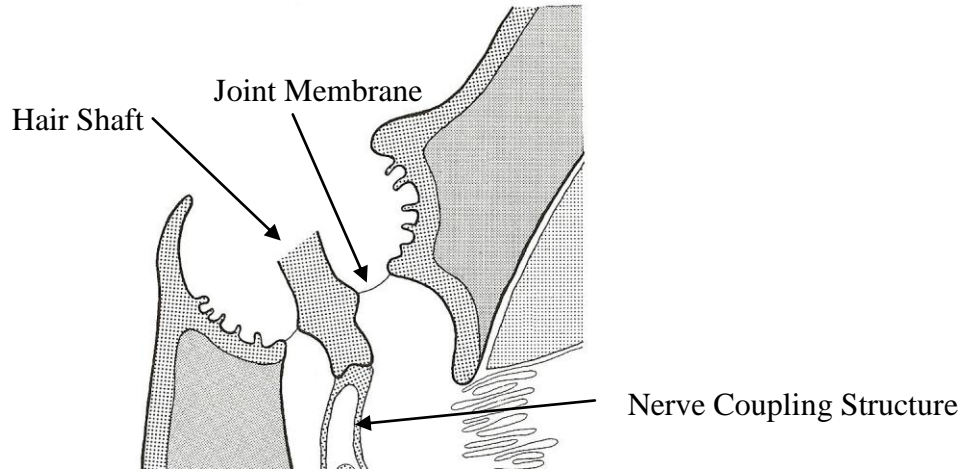


Figure 1.8: Trichobothria Transduction Physiology and Response. A) The Trichobothria physiology showing the support membrane and nerve coupling structure. B) The threshold deflection to elicit a nervous response, indicating a high-pass behavior for frequencies above 30Hz. (From Reference 58)

The TCB-membrane connection is more flexible than any other hair sensilla thus measured.⁶⁵ Fluid dynamics simulations put the torsional constant of the hair pivoting on the order of 10^{-12} Nm/rad; furthermore, there is a slight non-linearity of pivoting in

response to loading rate, with the damping constant modeled to be on the order to 10^{-14} Nms/rad.⁶⁶ Insect and arthropod mechanoreceptors will produce an action potential at deflections on the order of 1 nm.⁶⁷ This combination of high flexibility and low threshold deflection, makes for an incredibly sensitive flow receptor, in fact it has been estimated that work needed to stimulate the receptor is in the range of 2.5×10^{-20} to 1.5×10^{-19} J, which is on the order of a single photon of infrared light.⁶⁵ Threshold deflection measurements indicate a high-pass nature at very low frequencies, approaching DC (figure 1.8B).⁵⁸

1.2 Photo-thermal Sensing Background

1.2.1 Thermal-based Infrared Imaging

The approaches to infrared (IR) imaging technology can generally be broken into two major groups, photon-based and thermal-based.^{68,69,70} Generally, most photon-based imagers transduce IR radiation via photoconductivity by creating electron-hole pairs in semiconductors directly from infrared photon absorption. Thermal-based sensors transduce the heat created from infrared absorption, of which there are a variety of approaches. Initially, when infrared imaging was first being explored thermal-based technology was discounted because, until very recently, photo-thermal based approaches were considered very slow and insensitive. Therefore, the major developments in the last 60 years have been in photon based technologies. Over that time, photon based methods have proven to be incredibly fast and sensitive, but they have also proven to be expensive and bulky, with the high-end imagers requiring cryogenic cooling. Whereas, thermal sensors in the past were known as being fairly insensitive and relatively slow, now that

the technological focus has shifted. The thermal-based sensors are making a new name for themselves as being cheap, portable, sensors with good sensitivity at TV-rate scanning speeds.^{68,69,70}

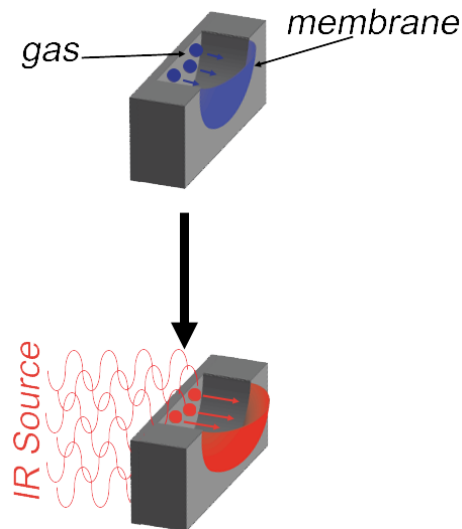


Figure 1.9: The Golay cell. A Thermal-pneumatic sensor (cross-section view)

Conventional thermo-pneumatic IR sensors, called Golay cells are made up of a micrometer scale thick membrane covering a macroscale (cm or larger) air filled cavity.^{68,69,70} When the air is heated upon IR absorption, the pressure increases thereby deflecting the membrane see figure 1.9. Recently, smaller microfabricated sensors have been developed, but with significant loss in sensitivity caused by the increased stiffness associated with the smaller diameter membranes (see equation 9.1 in section 9.2.2).^{71,72,73} The more sensitive sensors report deflections being up to 14 nm/K, which is quite low.⁷³ For more information regarding Infrared imagers refer to the following books and reviews.^{68,69,70}

1.2.2 Thermal Sensing of the Fire Beetle

Melanophila acuminata, or commonly called “fire beetles” are attracted to forest fires from great distances, at least 0.5-3 miles and maybe even up to 50-100 miles away (figure 1.10A).^{74,75,76,77,78} They mate and lay their eggs in freshly smoldering trees, which appears (based on observations) to make for a good environment for their larvae to develop.^{79,80}

These beetles find these far off fires by using infrared (IR) pit organs located near where their middle legs meet their thorax. Each organ is made up of about 75 spherical shaped receptors (figure 1.10B). These spherical receptors are commonly broken into 3 main parts (figure 1.10C), an amorphous core with (labeled 1 in Figure 1.10C), porous cuticular region (labeled 2 in Figure 1.10C), and an outer lamellae region (labeled 3 in Figure 1.10).⁷⁹ The cuticular sphere is covered by a protoplasmic layer, which is roughly 300nm thick, which is covered by a thin outer cuticle above the surface of the beetle. Supposedly, “from a biomechanical point of view, the sphere (region 1) hangs freely in a cavity within the cuticle, suspended from above only by a small stalk.”⁷⁹

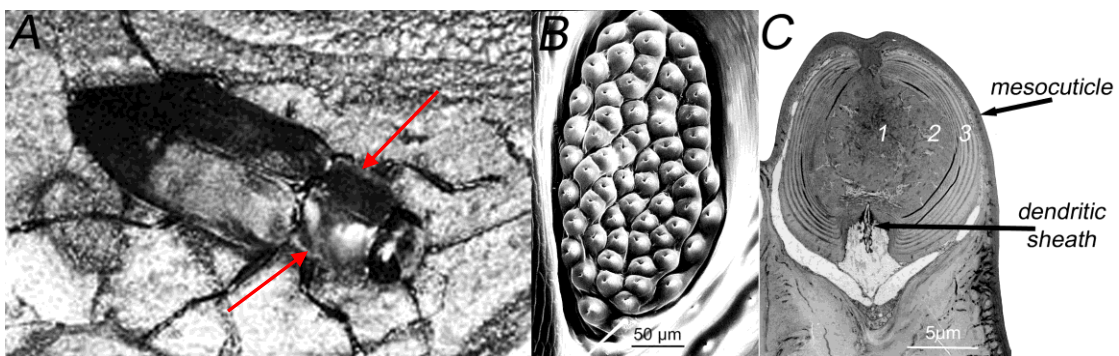


Figure 1.10: The Fire Beetle. A) A fire beetle, the arrows indicate location of receptors B) An infrared pit organ composed of an array of receptors C) A cross-section of an infrared receptor (Adapted from Reference81)

There is general agreement and good evidence that these IR receptors are thermal-mechanical based, are phasic in response, and are likely modified hair mechanoreceptors (much like trichobothria).^{79,82} Again, we see this approach of slightly modifying functional support structures of receptors to transduce different stimuli. It is not completely clear, which part of the receptor is primarily leading to this photo-mechanical deformation of the nerve. But, it is generally agreed that the stimulus is thermal-mechanical based, as opposed to thermal based, like the IR receptors of pit-vipers.⁸³ The intricate details surrounding the transduction mechanism are still to be revealed, the accepted explanation is that the material making up the receptors absorbs infrared radiation at a peak wavelength of about $3\mu\text{m}$ that heats the receptor and through thermal expansion, the spherule volume increases and the dendritic tip is deformed, thereby sending off an action potential. A possible detailed explanation is that the inner amorphous region (area 1 figure 1.10C) is a hollow gas-filled region (see figure 1.11A), which is responsible for providing the increased pressure upon thermally expanding.^{83,84}

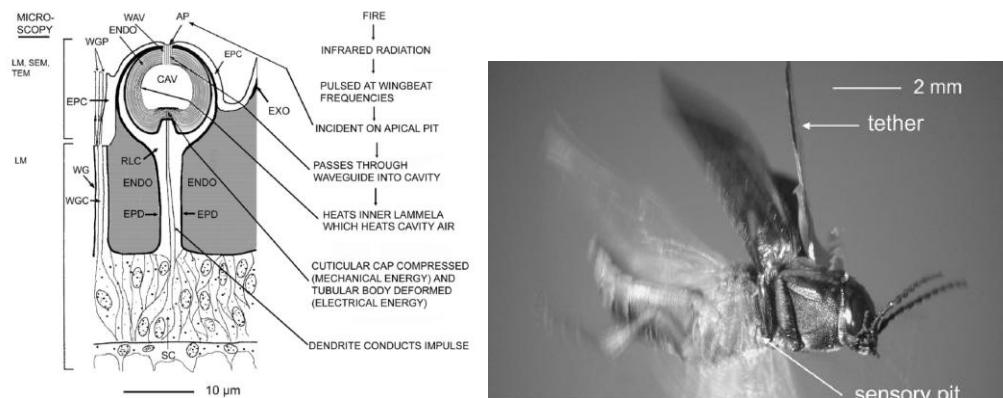


Figure 1.11: Fire Beetle Sensing. A) Schematic with possible air expansion sensing mechanism B) An optical picture showing the shuttering mechanism of the beating wing. (From Reference 84)

The receptors' threshold deflection a stimulus is time dependant, but is quoted to be between 0.06-5 mW/cm² and responding after 2ms or more.^{75,78,85} Saturation of the receptors has been reported to be around 300mW/cm², which leads to the estimation that the receptors would saturate from a forest fire at a distance of 100m or more.⁸⁵ Most studies are presented in terms of power density, instead of temperature. Furthermore, there is some speculation as to different cooling mechanisms, which depending on experimental conditions, could affect measurements that correlate response time with power density exposure. It has been speculated that the receptor lymph could function as a cooling system.⁸⁴ Speculation exists to the purpose of the wax filaments (not shown), including a convective cooling role.⁷⁹ Beetles cover the IR pit organs, when they walk with their legs, but when they fly the IR sensing organs are exposed. As the beetle is flying, the wings are continuously beating in front of the IR sensing receptors, thereby likely acting as a shutter, which allows the phasic receptors to properly sense the stimuli and allows for the receptor to cool, thereby preventing saturation, see figure 1.11B.^{77,84} Furthermore, it is very possible that the beating of the wings further cools the receptors via convective cooling. In fact it is well known that insect flight has a dramatic effect on the body temperature of the insects.⁸⁶ Usually, most insect flight convectively cools the insects to room temperature, although in some larger insects the heat created by the muscles during flight can cause body temperatures to rise.⁸⁶ Furthermore, haemolymph temperature control is also common.⁸⁶ Despite, what might be the case; it should be quite evident that a temperature control system would be quite powerful for a thermal-based IR sensing system, such as the fire beetle IR receptor pit. Temperature control would

essentially allow the insect to tailor the sensing range defined by the minimum stimuli threshold and saturation level.

1.3 Background Synopsis

- Current mechanical-based flow sensors are relatively insensitive and have high minimum detection thresholds
- Biology uses hair cells as a ubiquitous receptor and it tailors the surrounding structures to transduce the stimuli into appropriate mechanical stimuli for the hair cell receptor.
- Fish use a hydrogel-like structure called a cupula to enhance flow-sensing properties of the embedded hair cells
- Blind cave fish neuromasts also contain cupular fibrils that likely support a tall high-aspect ratio cupula and act to transmit the mechanical stimuli to the relatively short hair-cell receptors
- Signal processing involved in transducing and interpreting the information from an array of flow receptors requires non-portable hardware
- Wandering spiders have a well-developed sense of air-flow sensing and vibration sensing, but have a relatively simple nervous system. Therefore, their ability to cope with the high signal processing loads is impressive.
- The Wandering spider metatarsal lyriform organ is important for measuring vibrations of external stimuli. It has a high-pass nature that may be caused by an adjacent viscoelastic material.
- Wandering spider trichobothria are air-flow receptors that are incredibly sensitive, occur in arrays and may have high-pass characteristics as well.
- Current microfabricated thermo-pneumatic IR sensors lack sensitivity in their miniaturized form.
- The fire beetle uses a similar thermal-pneumatic transduction principle, but accomplishes this task with high sensitivity and a small foot-print. It appears that a nm-scale thick bulb is responsible for the signal transduction
- The fire-beetle uses the beating of their wings to act as a shutter to alter the stimulus to be appropriate for phasic sensing. Furthermore, this wing-beating may act as a temperature controller that enables the fire-beetle to have some degree of control over the sensing range.

CHAPTER 2

GOALS, OBJECTIVES AND OVERVIEW

2.1 Goals

The goal of this work is to gain understanding of biology's application of soft materials to enhance sensing abilities and initiate innovative bio-inspired material-based approaches for flow (fluidic and air) sensors and photo-thermal sensors. This research is inherently multi-faceted and while it aims at solving engineering problems, this goal is just a by-product of successfully implementing lessons taught by investigating functional soft material use in biology. A key aim is to help strengthen this niche of functional materials science referred to, here, as bio-inspired materials in sensing roles. The work aspires to traverse the boundaries of the subject in order to provide a strong foundation for future scientific explorations of the subject. In other words, the studies intentionally are aimed at several different areas of sensing in order to demonstrate the versatility of the scientific approach. The capabilities of the methodology are demonstrated with successful engineering studies.

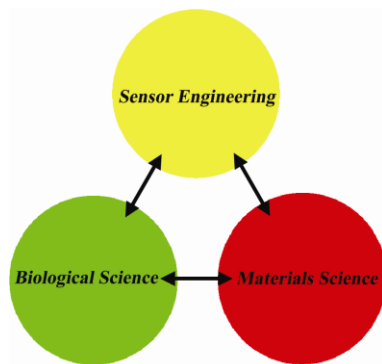


Figure 2.1: Aiming to combine materials science, biology and sensor engineering

2.2 Specific Technical Objectives

The technical objective of this work are summarizing as the following:

- Investigate morphology and microstructure of Blind Cave Fish receptors to understand the material-associated sensing strategies that biology utilizes for flow monitoring
- Fabrication of structured functional soft materials to implement the bio-inspired sensing strategies to underwater flow sensors
- Understand the impact that the bio-inspired structures have on the sensing performance of the artificial hair underwater flow sensors through testing and characterization
- Design and fabricate structures with consideration to commonalities and differences between the engineered sensors and their biological analogue
- Test the bio-inspired soft material structures to gauge their ability to improve sensing performance and to provide feedback to improve the original design.
- Investigate the role soft materials play in signal absorption and filtering in air flow and vibration reception of Wandering Spiders *Cupiennius salei* by testing and use these results to suggest novel strategies to further enhance air flow sensors
- Fabricate photo-thermal sensors based on ultra-thin films and investigate signal transduction strategies based on existing research of the fire-beetle IR receptors

2.3 Dissertation Overview

Chapter 1 is an analytical review of the bio-inspired design strategies as they pertain to sensing and materials. This chapter includes a synopsis of the current state of bio-inspired design, a forward-looking analysis of the evolution of bio-inspired design, and discussion of unresolved issues pertaining to the philosophy and implementation of bio-inspired design.

This chapter, **Chapter 2**, includes a concise description of the goals and technical objectives of the work presented in this dissertation. Furthermore, it provides a brief overview of the organization of the dissertation, with brief descriptions of the contents of each chapter.

Experimental techniques that played a critical role in the studies presented in this dissertation are described in detail in **Chapter 3**. The presentation of these methods includes 2 categories, material fabrication processes and characterization techniques. Material fabrication processes include spin-assembled layer-by-layer polyion deposition, electrospinning, drop-casting, photo-crosslinking and biological sample preparation protocols. Characterization techniques include atomic force microscopy, force-spectroscopy, scanning electron microscopy, optical interferometry, dipole-source flow testing and optical microscopy-based signal transduction. Several chapters include supplement this chapter with specific protocols used for the particular studies presented.

Chapter 4 presents the investigation of a functional material associated with spider strain receptors. The results of this study strongly support the hypothesis that this material plays a critical role in signal filtering, thereby leading to the high-pass nature of the vibration receptors. This investigation included surface-force spectroscopy studies

on live spiders. The measured elastic modulus of the material was time-dependant and increased with probing frequencies. The time-dependant trend of the minimum deflection to elicit a nervous response was the opposite of the elastic modulus trend, thereby indicating enhanced signal transmission is associated with the material stiffening. This appears to be the first evidence that biology uses viscoelasticity to filter out mechanical noise.

Studies on air-flow sensing receptors of spiders are presented in **Chapter 5**. This study involved performing force-spectroscopy measurements on the end of the hair-receptors. These measurements provided data, which validated previous fluid-dynamics models of the hair-receptors response to air stimuli. Furthermore, the data indicated that hair-receptors had a stronger time-dependant behaviour than was previously known. This data was used to develop a new material model for the receptor support material.

Fish flow reception studies are presented in **Chapter 6**, as well as subsequent bio-inspired underwater flow sensor development. The biological studies involved preliminary chemical studies of the cupula associated with the fish flow receptors by enzyme treatment. Furthermore, the mechanical properties of the cupula were also characterized with colloidal probe spectroscopy. A hydrogel with similar properties was developed by photo-crosslinking acrylate-functionalized poly-ethylene oxide. The material was also characterized with colloidal probe spectroscopy and found to have relatively similar properties as that of the fish cupula material. Having developed a bio-inspired cupula material, the material was applied to micro-fabricated flow sensors and found to significantly improve the flow sensing ability of the sensors.

Chapter 7 presents work that builds off the work presented in the last chapter. A method to deposit the bio-inspired hydrogel material to form a high-aspect ratio structure on the sensor was developed. This was accomplished by using a precise method to dropcast the hydrogel-solution on the hair without wetting the sensor substrate. The method provided the capability to control the height and width of the cupula structure. The resulting high-aspect bio-inspired structures dramatically improved the sensing ability of the flow sensors. The sensitivity and the minimum threshold deflection were both improved by almost 40 times. The capped sensors could sense flow on the order of $\mu\text{m/s}$, which competes with the capabilities of fish receptors.

Chapter 8 presents several fabrication techniques that expand the capabilities of the bio-inspired cupula approach. To further improve, the structure, bio-inspired cupular support fibrils were fabricated with a focused electrospinning methods. These fibrils supported much taller cupula, which should further improve signal absorption capabilities. The array work focuses on using the UV-photo crosslinking process to fabricate arrays of artificial cupula to cap sensor arrays. Fish utilize arrays of hair cell receptors to distinguish and interpret spatial flow information. The ability to “see flow” relies on arrays of receptors that are spaced over the fish body. Work was also focused on shaping the lateral dimensions of the cupula in more complicated shapes, like those seen in fish. Often superficial fish neuromasts contain hair-cells that are oriented along a single axis, endowing the neuromast with directional flow sensing abilities. Some fish have laterally anisotropic shaped cupula associated with these neuromasts can enhance the directional sensing capabilities by enhancing signal absorption along the hair-cell orientation and reducing signal absorption perpendicular to this direction. The

cantilever-based flow sensors are inherently more sensitive to flow parallel to the long axis of the cantilever. In order to enhance the directional sensitivity of the engineered system, we worked to implement this bio-inspired lesson by reproducing laterally anisotropic shapes, which will result in enhanced signal absorption perpendicular to the long axis of the structure.

Chapter 9 presents studies aimed at creating photo-thermal sensors based on ultra-thin freely suspended films, which is similar in structure to that of the anatomy of the IR receptors of fire-beetles. This study includes characterizing the IR sensing ability when the sensors were operated in a thermal-pneumatic transduction mode. They were also tested while operating in a thermal-strain based buckling transduction mode. The buckling transduction proved to be very sensitive. The exact details regarding the transduction mode of IR receptors in fire-beetles is unknown. These results indicate that certain conditions thermal-strain can be quite sensitive and can even out perform thermal-pneumatic transduction.

Concluding remarks, the overall significance of the dissertation and prospective applications of the work are presented in **Chapter 10**.

CHAPTER 3

MATERIALS AND METHODS

3.1 Atomic Force Microscopy

Atomic Force Microscopy (AFM) and force-spectroscopy play a key role in several studies in this dissertation through its ability to address localized materials and probe the mechanical properties of the material. AFM is microscopy method capable of atomic resolution, which was invented by Binnig et al. in 1986.⁸⁷ AFMs are conventionally composed of a laser, a photo-detector, a piezo tube, a reflective microfabricated cantilever with a tip and circuitry for feedback control and data analysis. The piezo tube usually contains 5 piezo-electric crystals, 2 piezos for each axis parallel to the sample surface (raster scan movement) and one piezo for the axis perpendicular to the sample (surface tracking movement). Depending on the location of the piezo tube, AFM systems can be sample scanning or tip scanning. Figure 3.1 is a schematic of the basic architecture of a sample scanning AFM.

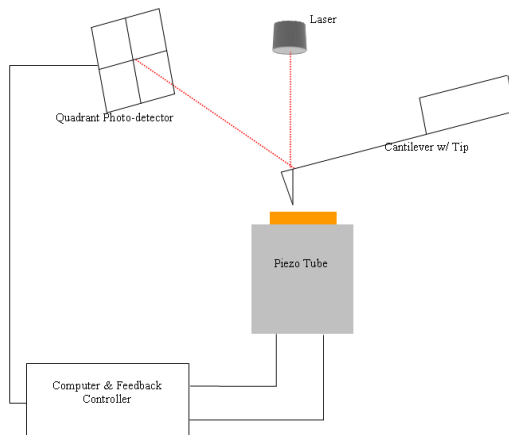


Figure 3.1: Schematic of a Sample Scanning AFM System.

The scanning can be done in several different modes, such as contact, tapping and non-contact, with tapping being the most common mode. Laser light is bounced off the cantilever into a position sensitive photo-detector. The position sensitive photo-detector gives a relative value of the deflection of the cantilever. The signal from the photo-detector is used to maintain a feedback loop with the z-component of the piezo tube. The AFM is a form of scanning probe microscopy (SPM). The first scanning probe microscope was the scanning tunneling microscope, then many different methods soon followed all using a scanning probe.^{88,89,90} These many different microscopy systems can obtain information about many different material properties, such as thermal properties, conductivity, and magnetic properties.

Since the birth of AFM over 20 years ago, it has revolutionized science.⁹¹ The unprecedented lateral and vertical resolution offered by scanning probe microscopy techniques enables the visualization of micro, nano and molecular-scale structure of polymer surfaces and interfaces. Apart from the advantages such as true 3D topology, minimal sample preparation, SPM techniques enable imaging the polymer samples in ambient conditions, under fluid, controlled environment and temperature. This ability to probe the polymer surfaces in variety of environmental conditions provides obvious advantages compared to traditional electron-based microscopic techniques such as scanning electron microscopy and transmission electron microscopy, which require vacuum conditions, and sample preparation such as microtoming, sputtering, and staining. Though AFM has capabilities like no other tool in the science repertoire, there are still some limitations and it is not perfect for every sample. It is often very hard to scan samples with a height change over 7 μ m. It is also difficult to scan regions over

100 μm^2 , although rarely scans can be obtained larger than 150 μm^2 . AFM is a technique that requires making contact with a sample, (or at least close enough for electrons to repel each other), therefore samples should be fully secured. If a sample is not properly immobilized it can be difficult to get good images. Nonetheless, various SPM techniques enable simultaneous probing of the structure and mechanical, electrical, thermal, or magnetic properties. This provides invaluable insight into the structure-property relationship of materials. Force-spectroscopy is a key technique used to probe the mechanical properties, adhesion and chemical-related information with the atomic force microscope.

3.2 Force Spectroscopy for the Mechanical Characterization of Polymers

Force-spectroscopy plays a very important role in this dissertation by providing the capability to measure the mechanical properties of small local regions, such as fish flow receptors. The atomic force microscope is capable resolving forces orders of magnitude less than chemical bonds.⁹² The photo-detector has sub-angstrom sensitivity, resulting in the theoretical ability to measure forces down to 0.1 pN, but noise from thermal, electronic and optical sources limits the force sensitivity in ambient conditions to about 1 pN.⁹² Therefore, it should be quite evident that the AFM has the potential to address materials and molecules with minimal forces over minimal surface areas. The importance of this method for this dissertation and the specialized nature of the measurements demand an in-depth review and explanation of the methodology.

Force-spectroscopy is a multi-step process, which should be done with great care to ensure accurate results. Without care, force-spectroscopy measurements can be very inaccurate, while results may still be quite precise. Therefore, it is quite important to fully understand the process and the sources of error. A complete in-depth review of the subtleties of force spectroscopy including contact theories and complex force curve interpretation is beyond the scope of this dissertation, but several in-depth reviews are available.^{93,94}

3.2.1 Force-distance Curves and Mapping

A single force curve, commonly called a force-distance curve, is a plot of tip-sample force vs. piezo movement (figure 3.2A). Figure 3.2B shows the plotting of the deflection data with time. Figure 3.2C is a schematic explaining the particular regions of force curves. Force-mapping (sometimes referred to as force-volume) is a spatial map of force-distance curves. This force-distance curve matrix can be used for sampling statistics, as well as relating surface features to mechanical properties.

Force-distance curves are obtained by monitoring the applied force while extending the vertical piezo to diminish the probe-sample distance until the cantilever is deflected by a set amount (trigger), followed by retraction of the vertical piezo. Unless otherwise stated, for the following discussion the convention of a sample-scanning AFM is used, where the vertical piezo actuator moves the sample with respect to the tip, as opposed to a tip scanning AFM.

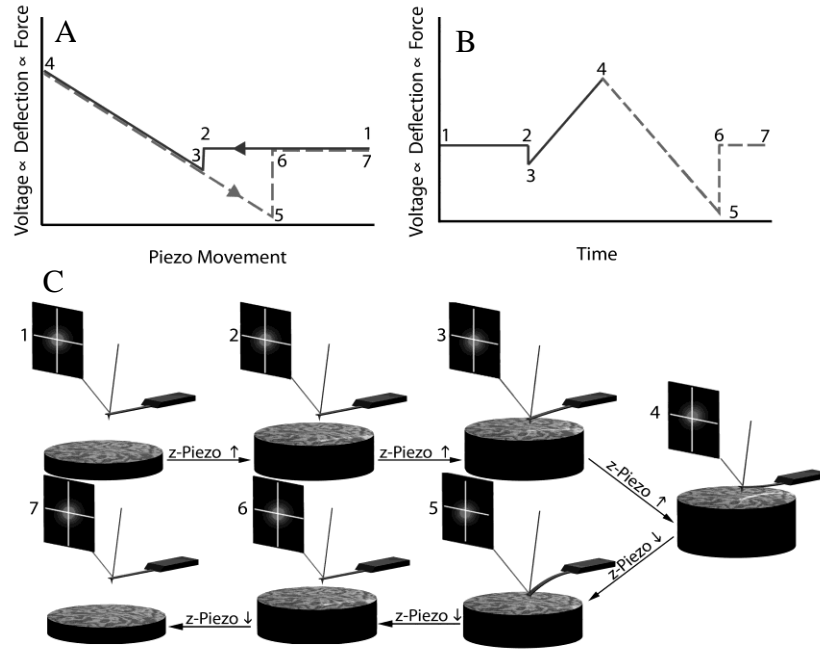


Figure 3.2: Force-Distance Curves. A) A Typical force-distance curve B) A corresponding curve showing applied force vs. time C) A schematic showing the individual steps of acquiring a Force-distance Curve, particular attention should be paid to the cantilever bending, the piezo position, and the laser spot.

Figure 3.2A, is an ideal force-distance curve plotted in the conventional manner. The x-axis can be understood as the distance between the tip and the surface and/or a measure of the interaction between the sample and the probe. The larger the piezo position value the farther the probe is from the surface. First, the vertical piezo is moved in the extension direction, which is depicted in the solid line in figure 6A and 6B. In the curve, line 1-2 is called the extension zero-line, which corresponds to the region when the sample is not in contact with the tip, but is moving towards the probe. Line 2-3 corresponds to the “jump to contact” region (also known as the snap-to region), when the probe is initially attracted to the sample surface, thereby bending the cantilever downward. The surface is also deformed slightly towards the tip. This is an unstable

region, like the snap from which is not monitored. As the piezo moves the sample surface closer towards the tip the cantilever passes the zero deflection and is further bent up. The deflection of the cantilever, when in contact with the sample surface, is indicated by the line 3-4. Point 4 indicates the end of the tip extension sequence and the beginning of the tip retraction sequence. Ideally, the line 3-4 and 4-5 will partially overlap and have the same slope during extension and retraction. Generally, line 5-6 represents the force of adhesion, the “snap from contact” region. Line 6-7 is again a region where the cantilever is free from the surface.

It is important to note that the applied force is indirectly measured by the AFM. The microscope itself only monitors the movement of the laser spot in the photodiode, which is related to the cantilever deflection via the photodiode sensitivity. The photodiode sensitivity, expressed in units of nm/V, must be calibrated for each set of measurements, which is described in the next section. The cantilever deflection is related to the applied force via the cantilever spring constant, which is expressed in units of N/m or nN/nm. The cantilever spring constant must also be calibrated for each set of force measurements, which is described in a later section.

3.2.2 Force Spectroscopy Calibrations

3.2.2.1 Calibrating the Photodiode Sensitivity

The vast majority of commercial microscopes use optical transduction of cantilever bending, which must be calibrated for force-spectroscopy. The photo-detector sensitivity relates the vertical photo-detector signal to the cantilever deflection.

Conventional imaging does not require this calibration because the height image is constructed from the feedback controlled piezo movement. Calibrating the photodiode sensitivity involves obtaining force-curves on a material with a stiffness that is much greater than the cantilever stiffness and therefore can be considered “infinitely hard”. Typically, a freshly prepared piece of silicon wafer is used, which is piranha-solution cleaned. Piranha solution is prepared by adding 30% hydrogen peroxide (1 part) to concentrated sulfuric acid in a ratio (3 parts) (as opposed to the convention of adding acid to a base), USE CAUTION in preparation! Silicon substrates are immersed for 30 min, followed by several washings under deionized water and then drying under filtered dry nitrogen gas. It is important to be stringent with cleaning of the calibration sample, to ensure that no surface contaminants interfere with the accuracy of the photodiode calibration. Error in the photodiode sensitivity causes an overall shift in all of the data. Therefore, while the precision will remain unchanged, the accuracy of the results of the data will be completely compromised.

The photo-diode sensitivity calibration is based on relating the known movement of the vertical piezo to the cantilever deflection. In the contact regime, the piezo position displacement, Z_{pos} , cantilever deflection, Z_{defl} and the sample penetration, h are related through:

$$z_{pos} = z_{defl} + h \quad (\text{Equation 3.1})$$

where the relationship holds for the contact regime. The actual calibration is obtained by taking the inverse of the slope of the photodiode voltage versus extensional piezo movement plot in the contact regime. Many microscopes have a simple curve fitting routine to perform the calibration. After calibrating the photodiode sensitivity, it is

important to ensure that the sensitivity does not change throughout a set of measurements.

3.2.2.2 Measuring Cantilever Spring Constants

There are several well developed methods for measuring cantilever spring constants, the most common methods are the added-mass method,⁹⁵ geometry-based methods,^{96,97,98} the spring-on-spring method,⁹⁹ and the thermal tuning method.¹⁰⁰ The discussion here is limited to the most convenient and most accurate methods, namely the spring-on-spring method and the thermal tune method.

The spring-on-spring method can be used to measure cantilever spring constants by performing force curves on a previously calibrated cantilever. This procedure does require that the photodetector sensitivity be calibrated for the cantilever acting as the probe. The measurements should be performed in a manner so that the tip is near the end of the other cantilever, as is shown in figure 3.3. Although, it is typical to use the unknown cantilever as the probe, this is not critical as long as the unknown tip is close to the end of the cantilever as is typical.

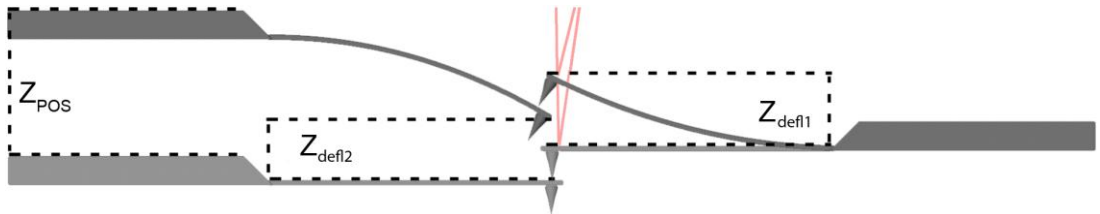


Figure 3.3: Cantilever Spring-on-Spring Constant Calibration

The spring-on-spring method utilizes the force balance between the two tips described as:

$$k_1 * z_{defl1} = k_2 (z_{pos} - z_{defl1}) = k_2 * P = k_2 * z_{defl2} \quad (\text{Equation 3.2})$$

where the subscript 1, refers to variables associated with the cantilever that is acting as the probe (the deflection transduced with laser-photodetector) and the subscript 2 refers to variables associated with the cantilever that is acting as the sample, being probed. To calculate the spring constant it is a simple matter of plugging in the calibrated spring constant into

$$k_{unknown} = k_{known} \left(\frac{z_{known}}{z_{unknown}} \right) \cong \left(\frac{dz_{known}}{dz_{unknown}} \right) \quad (\text{Equation 3.3})$$

where the z refers to cantilever deflection and the subscript known and unknown refers to variables associated with the calibrated cantilever and unknown cantilever, respectively.⁹⁹ This method has good accuracy, roughly 10%, when performed with care and is relatively easy to perform.

The thermal tuning method involves measuring the mean squared deflection of the cantilever caused by thermal motion. This method also requires the photodetector sensitivity to be calibrated. A cantilever spring constant can be described with the following relation:

$$k = \frac{k_B T}{\langle \Delta z_{defl}^2 \rangle} \quad (\text{Equation 3.4})$$

where k_B is the Boltzmann constant and T is the temperature in degrees Kelvin.¹⁰¹ In equation 3.4 above, the mean squared deflection is the sum over all of the harmonic modes of the cantilever. Usually thermal tuning is performed by obtaining the data for the first harmonic mode, and therefore a correction factor must be applied. The thermal tuning method and spring-on-spring have a similar accuracy of roughly 10%. The thermal tune is generally the easier to perform, but is not available on all

microscopes.^{102, 103} Although some commercial AFM have the electronics to perform thermal tuning, many do not or have a limited resonant frequency range, but those that have the capability have a simple routine to perform the measurements.

3.2.2.3 Tip Radius Measurements

It is well known that the tip dimensions distort the feature sizes of images. Furthermore, tip shape is often the source of common scanning artifacts, such as doubled-features. Although, this is a common imaging problem, in this section we are concerned with tip dimension measurements regarding the tip-sample contact area during force spectroscopy measurements. The accuracy of quantitative force measurements strongly depends on an accurate estimation of the tip-sample contact area. The tip-sample contact area is modeled as a function of the sample penetration, which is described later in this chapter. The most common models assume a spherical tip profile.

The size and shape of the tip must be known to quantify the applied force per area. Several methods have been used to measure the tip size and shape, including scanning electron microscopy (SEM) and transmission electron microscopy (TEM) using the so-called shadow technique.^{104,105} Another common method involves calculating tip dimensions from images obtained by scanning samples with known dimensions under tapping mode-AFM. Scanning standard gold nanoparticles (GNP) of diameters from 5-30 nm has proven to be quite accurate at characterizing the very end most portion of the tip. This method is quite appropriate for force spectroscopy measurements involving small penetration depths (several nm), required to elastically deform polymers with conventional probes (radii<100nm). Such nano-particle samples can be prepared relatively easily from commercially available kits (Ted Pella). The nanoparticles are

embedded in a poly-lysine coating, which when scanned appears to help to remove tip contamination. This scanning based method involves calculating the convolution of the particle shape from the tip shape and calculating the tip-size. This routine has been well-established in Dr. Tsukruk's lab.

3.2.3 Elastic Modulus and Contact Models

When performed with care data, elastic modulus from force spectroscopy has shown very good agreement with known samples, but should be considered accurate within an order of magnitude or a little better. It should be stated that characterizing the elastic modulus of a material with SFS is quite tedious and should be done with the utmost care. There are many samples that SFS-based elastic modulus measurements are the only viable option, but other options should always be considered, such as buckling based metrology (BBM).¹⁰⁶ BBM is much less time-consuming and has about the same accuracy as SFS. BBM was used for initial developments of freely-suspended films, but is not a critical technique to the work presented in this dissertation. Freely-suspended films can also be characterized using the so-called bulging approach. Each of these techniques has their own set of limitations and issues to consider.

In order to calculate the elastic modulus from applied force and sample penetration data, equations are derived from a quasi-static spring-on-spring, or force balance approach as

$$z_{defl}k = P(h) \quad \text{(Equation 3.5)}$$

where P is the applied force and h is the sample penetration as already defined.^{107, 108} Assuming a spherical tip, flat surface and no plastic deformation, one can define an effective spring constant or stiffness for a material as:

$$k_M = \left(\frac{\partial P}{\partial h} \right) = 2r \frac{E}{1-\nu^2} \quad (\text{Equation 3.6})$$

where r is the tip-surface contact radius, E is the material elastic modulus, ν is the material Poisson's ratio.¹⁰⁹ Unfortunately, even after determining the tip radius, there is currently no known way to measure the contact radius in real time as the measurements are performed.

Instead, contact models are used based, which generally differ in the tip-surface interaction's contribution to the contact area. For the sake of brevity, here we will only present the Hertzian contact model in regards to calculating elastic modulus, but there are other models that can be more appropriate, considering tip-surface interactions. For in-depth discussions of contact models see the following reviews.^{93,94}

The Hertzian contact model assumes that the adhesion forces are zero and that at zero applied loads the contact area is also zero. The force as a function of penetration depth is described by the Hertzian model as:

$$P = \frac{4}{3} R_T^{1/2} h^{3/2} E' \quad (\text{Equation 3.7})$$

where R_T is the tip radius and E' is the composite modulus defined as

$$\frac{1}{E'} = \frac{3}{4} \left(\frac{1-\nu_S}{E_S} + \frac{1-\nu_T}{E_T} \right) \quad (\text{Equation 3.8})$$

where the subscript S and the subscript T refer to sample and tip related variables, respectively. The modulus associated with the probe is generally assumed to be much

larger than the elastic modulus of the surface. Therefore, a simplified equation for the elastic modulus based the Hertzian approximation can be expressed as:

$$E = \frac{3}{4} \left(\frac{1-\nu^2}{R_T^{1/2}} \right) \left(\frac{dP}{d(h^{3/2})} \right) \quad (\text{Equation 3.9})$$

Therefore, when plotting the penetration raised to the 3/2 power versus the deflection (or the applied force) a straight line should result from data taken with a spherical tip and little to no surface-tip interaction, commonly referred to as Hertzian coordinate plot. This plot provides both individual elastic moduli measurements for each point as a function of penetration, as well as the overall slope provides a measure of the elastic modulus.

3.3 Electrospinning

Electrospinning is being explored to fabricate cupular support fibers, like those present in the superficial neuromasts of blind cave fish. Electrospinning is a method to spin polymeric fibers with diameters ranging from micron scale to nanometer scale. Electrospinning is usually performed by applying a high voltage potential between a syringe filled with a polymer and a substrate; it is this voltage difference that drives the electrospinning process. In general, electrospinning can be performed with a very simple setup, which includes a syringe, a metal collecting plate and a high voltage power supply. Although, electrospinning setups can be relatively simple, controlling the variables and properties of the fibers can be very difficult and complicated. Furthermore, despite intensive research in electrospinning, the understanding of this highly dynamic process remains incomplete. Some of the relevant variables are voltage, polymer concentration, solvent volatility, solvent viscosity, solvent surface tension, solvent conductivity, syringe

pressure, temperature, collector distance and much more. The popularity of this method has fueled the development of many complicated setups, which help in controlling the properties of the fiber and collecting the fibers. An in-depth review of this subject is beyond the scope of this proposal, but one may refer to relevant papers and reviews.^{110,111,112,113}

3.4 Layer-by-Layer deposition

Layer-by-Layer (LbL), re-discovered in the early 1990's, is a method that most often utilizes electrostatic interactions between ions (often polyions) of opposite charge, but LbL can utilize other interactions such as hydrogen bonding.^{114,115} Alternating cation and anion layers are deposited to form multilayer films. LbL films are thermodynamically unstable materials, but the strong ionic bonding creates a long term kinetically stable material. LbL film fabrication is quick, economical, and simple. To say the least, the LbL deposition method is versatile and adaptable. Depending on many variables, polyelectrolyte bilayers thicknesses can be made from sub-nm scale to sub- μm scale, but are often several nm thick. Much of the control of the thickness of the individual bilayers comes from the solution properties of polyions and their ability to have straight backbones or random coil conformation. In most cases the thickness of the multilayer is linearly dependant on the number of bilayers (although the first few layers are thinner and don't follow the linearity).¹¹⁶ Therefore, the total thickness of the multilayer films thickness can be precisely controlled, even at up 1 nm resolution. Furthermore, LbL can be used to precisely control the surface energy of a substrate.^{117,118} It should be stated that although LbL deposition is incredibly simple to perform, the

physics and understanding of the process is less straightforward.^{119,120} A full discussion of LbL deposition is beyond the scope of this proposal, for more information see the following reviews and articles.^{117,118,119,120,121,122,123,124,125,126}

3.5 Other Methods

The primary experimental methods that lead to the results presented in this dissertation are presented in this chapter and the experimental sections of the remaining chapters. Although, there are many other methods that were used in preliminary studies including scanning electron microscopy, cupula enzyme treatments and staining for SEM preparations, ellipsometry, buckling based metrology, and viscometry.

CHAPTER 4

SPIDER VIBRATION RECEPTOR STUDY

4.1 Introduction

Vibrations play an important role in the life of spiders, which use them for prey detection, communication during courtship, and other behaviours.^{127,128} The key vibration receptor organ of spiders is the metatarsal organ. It represents a compound or lyriform slit sense organ and belongs to a class of sensory receptors embedded in the spider's exoskeleton and measuring the minute strains occurring in it due to muscle activity, hemolymph pressure, vibrations and other types of mechanical stimuli.¹²⁹ The threshold vibrations necessary to elicit a nervous response of the sensory cells supplying individual slits in this organ are known to exhibit pronounced high-pass characteristics, with low sensitivity for frequencies below about 30 Hz and steeply increasing threshold sensitivity at higher frequencies.¹³⁰ Other than this change in sensitivity, the organs are not tuned to specific frequencies within the biologically relevant range. The dramatic change in sensitivity was found to be important physiologically for the spider, because it provides filtering of biologically irrelevant background noise, and at the same time preserves much higher sensitivity to biologically relevant vibrations like vibratory courtship signals and vibrations produced by prey motion.¹²⁹

Located at the distal end of the metatarsus just in front of the metatarsal lyriform organ is a pad cushioning the joint between the tarsus and metatarsus (figure 4.1a-d). This pad is crescent shaped and its cuticle approximately 100 μm thick. It is believed that this pad might be a mechanical source of the physiological high pass filtering. Substrate vibrations naturally picked up by the tarsus are detected by the slits of the metatarsal lyriform organ when the proximal end of the tarsus pushes against the distal end of the metatarsus, which in turn compresses the slits (figure 4.1b). Therefore, this pad seems ideally placed to mechanically filter stimuli to the lyriform organ through frequency dependent damping of the mechanical vibrations. The present study is undertaken to support or reject this hypothesis.

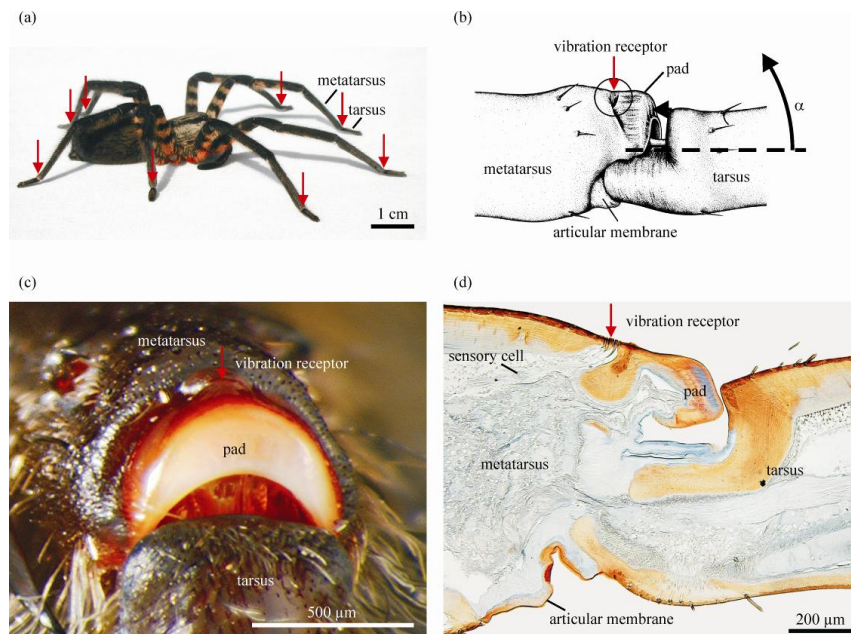


Figure 4.1: The Wandering Spider Vibration Receptor and Associated Pad. (a) Adult female wandering spider *Cupiennius salei*. The damping pad examined and the vibration receptor organ are located on the metatarsus at the joint with the tarsus (see red arrows). (b) Deflection of tarsus by an angle α exceeding 25° leads to pressure on the pad in front of the vibration receptor. (c) Vibration receptive lyriform organ located between the pad and the stiff cuticle of the metatarsus. (d) Sagittal section of the joint, Mallory stained. The pad consists of layers of different types of cuticle; the blue colour indicates soft, moderately sclerotized cuticle. Slits of the vibration receptor are innervated by bipolar sensory cells.

The low forces applied in atomic force microscopy (AFM) and surface-force spectroscopy (SFS) allow very soft materials to be probed with nanoscale resolution, while avoiding plastic deformation of the material.^{131,132} There have been several previous studies investigating viscoelastic properties of polymeric and biological materials using AFM.^{133,134,135,136} The indentation depths of AFM are on the order of tens of nanometres under nano-Newton forces unlike in conventional microindentation with micrometer indentation depths under micro-Newton forces. This allows limiting the indentation to the selected surface areas of the material of interest without contributions from surrounding structures or materials. In addition, the small size of the AFM probes (nanometres for regular tips and micrometers for colloidal probes) defines small contact areas (diameters of the order of a fraction of a nanometre or a micrometer) and allows high spatial resolution when probing the material properties across the pad.

4.2 Materials and Methods

Live adult females of *Cupiennius salei* (Ctenidae), which is a large (leg span ca. 10 cm) Central American wandering spider, were immobilized on a solid substrate and fixed to the stage below the scanning probe.¹²⁹ The tarsus of an individual leg was then deflected away from the metatarsus in order to expose the joint pad for the measurements. AFM topographical data and force-distance curves (including SFS) were obtained with a Dimension 3000 microscope (Digital Instruments, Inc.). The AFM

images were obtained using established procedures of the light tapping mode scans in air with scan rates below 2 Hz and an overall resolution of 512 x 512 pixels for scans ranging from 1 x 1 μm to 30 x 30 μm .^{137,138} For these scans, standard silicon tips (MikroMasch, NSC11) were used.

The viscoelastic properties of the pad material were probed by acquiring both force-distance and force-volume curves using 5 μm spherical Borosilicate microsphere probes (Novascan) to reduce local pressure in the contact area. All loads were applied in the proximad direction (similar to natural stimulation) to the distal joint region with the AFM tips approaching and retracting from the pad surface at different velocities. Spring constants were chosen between 1 and 3.6 N/m.¹³⁹ The cantilevers were calibrated applying the accepted spring on spring technique and using a manufacturer calibrated reference tip (MikroMasch) with a spring constant of 4.5 N/m.^{140,141}

Force-distance data was collected in air at ambient temperature and humidity in force-volume mode, which included consecutive probing of selected surface areas (16 x 16 points, number of force-distance curves = 256). In this way multiple force distance curves were obtained at each surface location and different deflection thresholds studied in order to monitor any changes in the material properties due to plastic deformation by the following AFM scans of the surface area probed. After, obtaining multiple force curves, no changes in the force curve shape was observed, thus confirming the non-damaging character of our measurements. Force distance curve maps were then taken at 3 to 5 locations on each joint pad and the data averaged over these locations and thus for several hundred indentations. The frequencies chosen for probing elastic responses (0.1 –

112 Hz) were limited by the sampling rates of the AFM scanner and its resonant frequencies. However, they cover a significant part of the biologically relevant range.¹²⁹

Force-volume analysis was employed according to established procedures. The elastic modulus was calculated from this data by fitting the loading curves according to the Hertzian contact mechanic model, which describes the interactions between the tip and the sample under the assumption of elastic deformation, small contact areas, and negligible adhesive forces.¹⁴² Alternatively, the model of Johnson, Kendall and Roberts, which considers adhesive properties, and Sneddon's model, which considers different tip shapes and the contact areas, were applied to derive the elastic modulus values.^{143,144} However, the results obtained with different models were well within the error associated with the method and simplicity we used the results obtained with the Hertzian model. The adhesive forces were determined from force-distance curves at the pull-off point.

4.3 Results and Discussion

4.3.1 Receptor Pad Surface Topography

AFM topographical images confirmed that the surface of the studied pad was consistently smooth with small bumps that are generally uniform and have a diameter of 200 to 400 nm and a height of 10 to 30 nm. There are several larger surface bumps as well (figure 4.2a,b). The phase image shows the same contrast level for both the surface and the surface bumps, therefore the bumps have similar composition.¹⁴⁵ The bumps are located above the openings of the pore canals, through which the topmost lipid layers of the epicuticle are secreted. Their distribution matches with that of the pore canals shown

in previous transmission electron microscopy studies of the cuticle of *Cupiennius salei*.¹⁴⁶ The mechanical tests were performed to include these surface features; because they are included (or the substances smeared in the contact area) as well when the spider's tarsus contacts the pad under natural conditions.

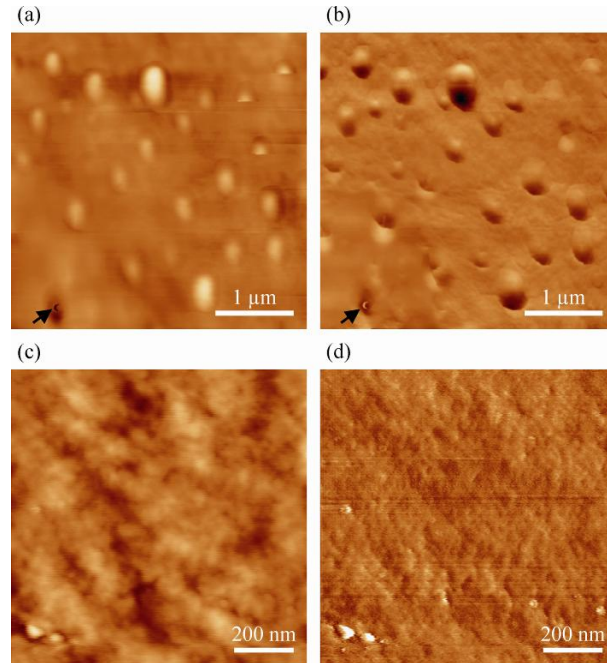


Figure 4.2: The Receptor Pad Surface. (a) AFM height image of the pad surface with 100 nm height range; (b) phase image of the same surface area with 60 degree phase range. The dome shaped structures are droplets of epicuticular substances, which are secreted through openings of pore canals. The arrows point to an individual pore canal opening. (c) Height image of the pad material at high magnification, 10 nm height range, and (d) phase image of the same surface area with 30 degree phase range.

The concurrent high-resolution phase image clearly shows a fine texture of globular aggregates with lateral dimensions below 100 nm (figure 4.2c,d). The RMS (root mean square) micro roughness within a 1 x 1 μm surface area was calculated to be very low with 0.8 nm. This value is on par with molecularly smooth surfaces with local

variations not exceeding two diameters of molecular backbones and very common for soft, amorphous polymeric materials with uniform chemical composition.¹³⁸

4.3.2 Receptor Pad Force-Spectroscopy

Figure 4.3 shows typical force-distance curves obtained for the pad material and for the same tip probe on a silicon substrate used as a reference surface. The force-distance curve taken for the silicon surface was used to calibrate the sensitivity of the AFM measurements. This curve shows a very linear shape in the region of direct contact between the tip and surface. A relatively high adhesion (high pull-off forces) is caused by strong capillary interactions between the hydrophilic AFM tip and the hydrophilic substrate under conditions of ambient humidity.

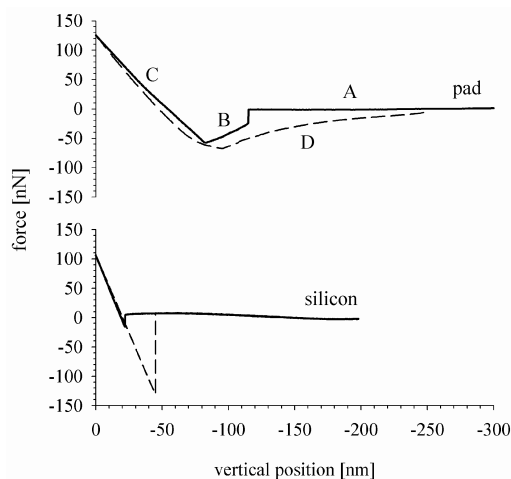


Figure 4.3: Characteristic Force-distance Curve. (Top) on the pad material and (Bottom) a typical force-distance curve on silicon used for sensitivity calibrations. The solid lines represent data acquired while the tip was approaching the surface and has to be read from right to left according to convention. The dashed lines represent data acquired while the tip was retracting from the surface and has to be read from left to right, again according to convention. Therefore, the start (and end) region is at the right end of the curve, whereas its left end marks the point where the probe tip changes direction. Region A, approaching the sample; region B, contact with the sample; region C, increasing force applied to the sample; region D, adhesive forces between the pad and the tip.

Unlike in the case of the substrate force-distance data for the stiff and hydrophilic silicon, a sharp jump-in event with an extended area of negative tip deflection was consistently observed for the compliant pad surface (region B of figure 4.3). Direct mechanical contact was followed by a positive deflection (region C of figure 4.3) and a broad pull-off region with lower forces (region D of figure 4.3). At region A of the curve, the probe is approaching the surface and any attractive forces between the surface and the tip are negligible compared to the cantilever stiffness thus generating a zero-deflection response. In region B of figure 4.3, we see the expected quick jump into contact, followed by a less expected shallow deflection of the cantilever towards the surface, an unusual phenomenon for clean elastic surfaces. This behaviour is indicative of the tip passing through an extremely compliant viscous material that is not slowing its deflection towards the surface but also generates attractive forces caused by the wetting of the glass probe with the topmost viscous layer (capillary phenomenon). Our data suggest that this topmost layer is viscous, polar, and hydrophilic (gel-like) to wet the glass bead attached to the AFM cantilever. Moreover, its presence is shown on the curve for probe retraction, where instead of a sharp pull-off event a gradual decrease of adhesive forces is observed, which corresponds to the typical capillary behaviour (region D of figure 4.3).

As the AFM probe is withdrawn from the surface, the attractive forces between the probe and the indented surface are overcome by the stiffness of the cantilever and the probe begins to return to its zero deflection resting point with a gentle deflection finally followed by a small sharp “snap from” region (figure 4.3). Again, this indicates that the

tip is passing through a viscous material and the long-range capillary forces are involved causing gradual thinning of the viscous meniscus before final rupture. The thickness of this surface viscous layer can be estimated from the tip deflection to be within 20 – 40 nm for different locations and probe frequencies. The appearance of such a viscous surface layer can be directly related to the presence of the oriented lipid layers, which lie above the cuticulin layer and the dense layer of the epicuticle of *Cupiennius*.¹⁴⁶

At the positive slope of the force-distance curves (region C of figure 4.3, which has to be read from right to left), the tip has made contact with a stiffer elastic material with a measurable resistance to compression. The tip is deflected upwards as the probe pushes into the surface. This is the deformation region of the force curve, which reflects both tip deflection and surface deformation and can be used to analyze the elastic behaviour of the material probed.

4.3.3 Receptor Pad Elastic Modulus

As mentioned above, the force curves indicated that there was significant wetting and adhesion between the tip and pad surface. In such a situation the Hertzian approximation would tend to underestimate the contact radius, thereby leading to a slightly higher elastic modulus than is the case (usually between 5 – 10 % for elastic materials with modest adhesion). Generally, a better choice to calculate the elastic modulus of such a material would be the JKR model, which assumes high adhesion.¹⁴⁷ As will be discussed later, the adhesion decreased significantly with increased frequencies. This means that when using the JKR model the change in increase in modulus due to material properties would be slightly exaggerated, whereas using the

Hertzian model will slightly underestimate the change in modulus with frequency. Although there was significant adhesion with several of the lower frequency measurements, using the JKR method leads to a more conservative estimation of the material's mechanical filtering abilities. Our estimation showed that for larger elastic deformations the result obtained from both models (as well as from Sneddon's model) converge, the difference being insignificant for the purpose of this study. Thus, for the sake of clarity and consistency, we applied the Hertzian model to analyze all our data. To this end, we analyzed the shapes of the loading curves and fitted them for penetrations not usually exceeding 20 – 30 nm for loading forces below 200 nN. The 30 nm of displacement of the pad's dorsal edge corresponds to a change of the angle between metatarsus and tarsus of the spider leg by 0.007° and a displacement of the tarsus tip by about $0.4 \mu\text{m}$.¹⁴⁸ This value represents the sensory threshold of individual slits of the metatarsal organ for substrate vibrations at 70 Hz (slit 6) up to 170 Hz (slit 7).¹³⁰

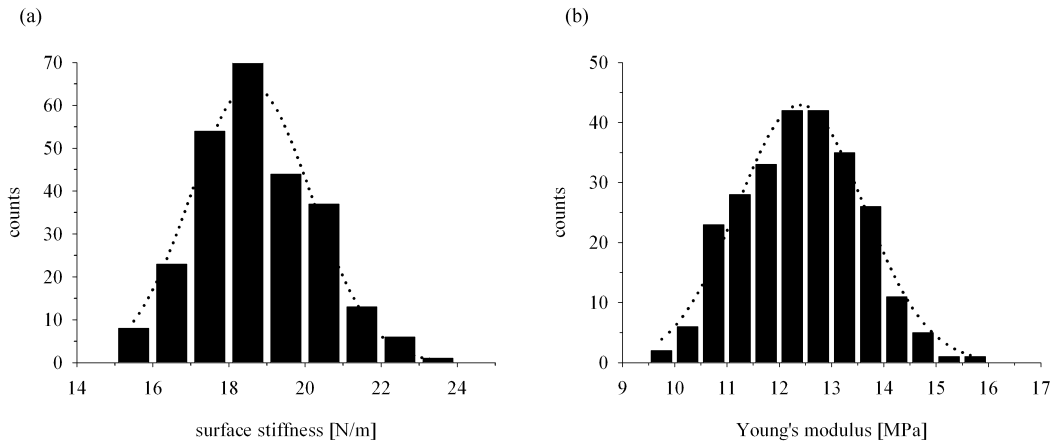


Figure 4.4: Stiffness and Young's Modulus Histograms. Typical distribution of values for surface stiffness (a) and Young's modulus (b) for the same pad at 13.9 Hz loading frequency derived from force-volume data taken in a 16×16 array of $1 \mu\text{m} \times 1 \mu\text{m}$ ($N=1$, $n=256$).

Figure 4.4a shows a representative histogram of the surface stiffness data obtained at 13.9 Hz and calculated as the overall slope of the force-distance curve in the direct physical contact regime in linear approximation. The surface stiffness of the pad material at moderate probing frequencies of 13.9 Hz was about 18 N/m with a distribution in between the range of rubbery and glassy macromolecules.¹⁴⁹ The distribution of values of the elastic modulus received for $16 \times 16 = 256$ overlapping locations of a $1 \mu\text{m}^2$ area for each spider was very uniform (figure 4b). The loading curves (penetration versus loading force) used for fitting analysis were smooth for all surface locations with indentation depths of up to 30 – 35 nm for loading forces below 200 nN. The value of the elastic modulus for these indentation depths is within a range common for compliant elastic macromolecular materials with low cross-linking density and above the glass transition temperature. The relatively narrow distribution of the surface stiffness (standard deviation within $\pm 5\%$ in most cases) indicated a very uniform elastic response of the pad materials under the probed conditions and with the contact area between the probe and the surface below $0.2 \mu\text{m}^2$.

4.3.4 Receptor Pad Frequency Response

Finally, we analyzed the mechanical response of the pad surface at different probing frequencies ranging from 0.1 to 112 Hz (the frequency being limited by thermal drifts and piezo-element resonances), corresponding to a tip velocity from very slow (50 nm/sec) to modest (25 $\mu\text{m}/\text{sec}$). Figure 4.5a shows the characteristic force distance curves (*a*) obtained at different frequencies and their corresponding loading curves

(figure 5b). At frequencies below 30 Hz the force curves obtained have the characteristic shape discussed above with little variance. However, at higher frequencies, this shape changes significantly due to the change of the overall slope. The hysteresis between the approach and retraction curves caused by the hysteresis of the piezo-element at high frequencies became clearly visible. Examination of this hysteresis on silicon samples showed that the slope of the force-distance curves changed by less than 5 percent for this frequency range. This is insignificant compared to the change of the slope for pad materials itself we observed here. Therefore, the frequency-dependent elastic behaviour is a feature typical of the biological material examined.

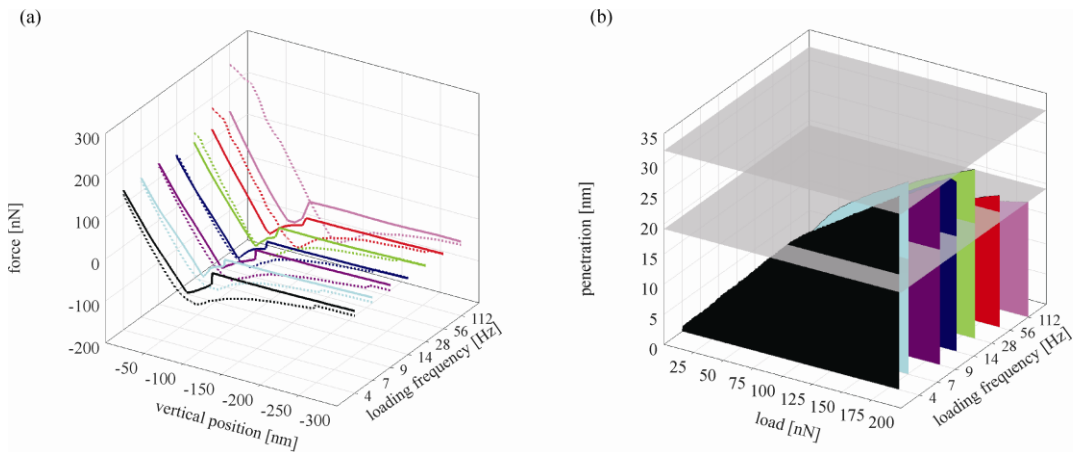


Figure 4.5: Force-distance and Load-penetration with Probing Frequency (a) Force-distance curves at different probing frequencies; solid lines are approach data, dotted lines are data for the retraction of the probe; (b) loading curves obtained at different frequencies for the pad surface at the same location. The grey planes are drawn at the maximum penetration at 4 Hz loading frequency, and the maximum penetration at 112 Hz loading frequency, respectively.

Force distance curves measured at frequencies lower than 10 Hz consistently resulted in values of Young's modulus between 10 and 20 MPa for the pad surfaces of

five spiders probed at various locations (Figure 4.6a). There was some variance in this value between different specimens; however, the modulus at each spot on the pad varied insignificantly between 0.1 Hz and 10 Hz and all values calculated fell within 15 ± 5 MPa for all varieties of conditions tested. However, above 10 Hz, the value for Young's modulus gradually increased up to 70 MPa for the highest frequencies with a dramatic increase occurring at circa 30 Hz and higher. Interestingly, the adhesive forces which were very high at low frequency, dropped significantly by ca. 40 % in the same frequency range. This confirms the trend toward a more apparently resistant surface, which effectively decreases the contribution of the tip wetting for short contact times (Figure 4.6c).

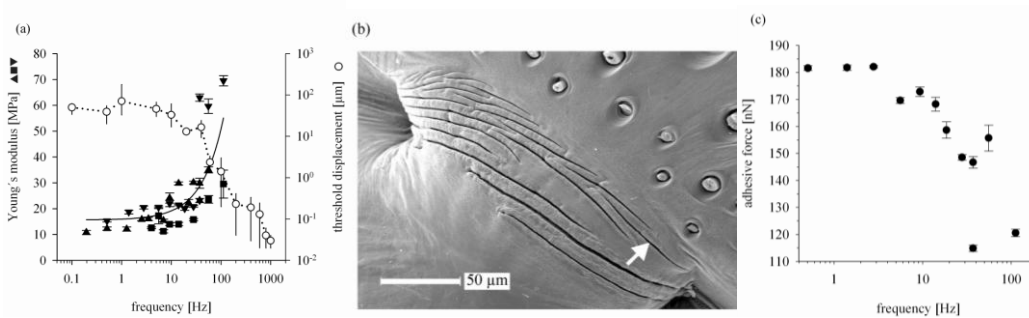


Figure 4.6: The Correlation between Elastic Modulus and Nervous Response (a) Frequency dependence of Young's modulus (filled symbols) and of sensory thresholds of slit 7 of the metatarsal lyriform organ (open circles). The different datasets of Young's modulus are from 3 locations on joint pads of 2 spiders. Each data point represents 10 – 15 force-distance curves. Sensory threshold curve adapted from a previous publication.¹³⁰ (n=16). (b) SEM micrograph of the metatarsal organ of *Cupiennius salei* (picture by R. Müllan). The arrow points to slit 7. (c) Adhesive forces measured at different loading frequencies at one location of a joint pad.

The frequency dependence observed here is attributed to the viscoelastic behaviour of the pad material caused by the time-dependent relaxation of the macromolecular

materials in the vicinity of the glass transition.¹⁵⁰ In fact, very similar frequency dependencies have been observed for elastomeric materials and were related to the lowered glass transition temperature of the surface caused by the presence of the swollen topmost surface layer.¹⁵¹

Thus, the change of the elastic modulus with shorter contact times follows common trends well-known for viscoelastic macromolecular materials in the vicinity of the glass transition temperature.¹⁵⁰ Upon elastic deformation of any material some of the energy is stored and some of it is lost in the form of heat, or essentially absorbed. The storage modulus is a measure of the amount of energy stored upon deformation, whereas the loss modulus is a measure of the amount of energy released as heat upon deformation. The ratio of energy absorbed to energy stored reaches a maximum right in the vicinity of the glass transition region, which constitutes a viscoelastic damping phenomenon. When the temperature of a material goes below the glass transition temperature or the deformation rate becomes faster than the polymer's relaxation time the elastic modulus dramatically increases. Therefore, materials with a glass transition temperature near the intended operating conditions, such as the spider's pad in the vicinity of room temperature, makes very good energy absorbing materials with maximum energy dissipation at low frequencies.¹⁵⁰

Importantly, the frequency-dependence of the elastic response observed here for the pad material is opposite to the frequency-dependence of the sensory threshold reported previously for the metatarsal lyriform organ (figure 4.6a,b).¹³⁰ The deflection of the tarsus needed to elicit a nervous response (action potential) measured between ca. 100 μm to 10 μm at vibration frequencies up to 40 Hz and dropped steeply to values as low as

0.01 μm to 0.001 μm at 1 kHz.¹⁵² Figure 4.7 is a schematic meant to indicate the pads role in breaking the transmission of low-frequency mechanical stimuli.

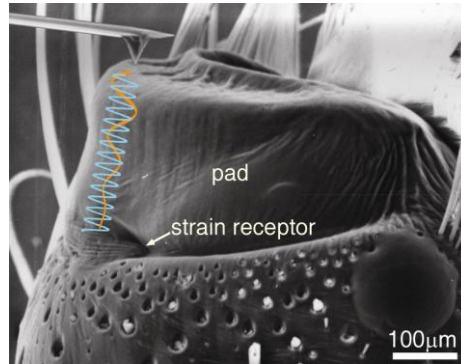


Figure 4.7: Schematic of Pad Signal Filtering (Adaptation of a picture from Prof. Barth).

The frequencies of wind-induced vibrations of the leaves of the dwelling plants of *Cupiennius* are significantly lower than 30 Hz. On banana plants and bromeliads they do not exceed 7 Hz.¹⁵³ However, for higher frequencies of mechanical perturbations, such as prey generated substrate vibrations or the vibratory signals of a sexual partner, the viscoelastic pad material partially loses its viscous nature effectively becoming stiffer, and, thus transmitting external mechanical stimuli with higher efficiency (low dissipation). Vibrations of the dwelling plants of *Cupiennius salei* induced by prey like a crawling cockroach have a broad frequency spectrum containing frequencies higher than 200 Hz. Male abdominal courtship vibrations peak at ca. 75 Hz, whereas male drumming and scratching on the leaf results in vibrations of 250 Hz and higher. The dominant frequency of the female courtship vibration answering male signals is about 30 Hz.^{129,152}

The average daily temperatures in the habitats of *Cupiennius salei* in Central America are around 20° C, with frequent daily maxima above 30° C all the year round.¹⁵⁴ During the day, when the ambient temperature is high, the spiders rest hidden in their

retreats on the dwelling plants. Their hunting activity starts after sundown, when the temperature is moderate. The pad should be stiffer due to the lowered temperature at night, and the metatarsal vibration receptive organ more sensitive to vibrations than during the rest period of the spider.

4.4 Conclusion

Spiders strongly rely on substrate vibrations for the guidance of prey capture, predator avoidance, and mating behaviour. These signals must be separated from the environmental noise. The most important vibration receptor organ in spiders is the metatarsal lyriform organ, which is relatively insensitive at frequencies below 30 Hz, but increasingly sensitive at higher frequencies. When deflected by vibrations the tarsus first transmits the stimulus to a soft material pad, which in turn passes it on to the metatarsal vibration sensor immediately behind it. The pad material was found to be highly viscoelastic with its highest compliance and high energy dissipation at frequencies below 30 Hz. At frequencies above 30 Hz the pad material quickly becomes stiffer, which allows better transmission of vibrations to the metatarsal lyriform organ. However, the pad material becomes stiffer if the deformation time is relatively short, the vibration frequency is relatively high, or the temperature is well below the glass transition temperature. Under these conditions the effective Young's modulus will increase, and mechanical losses will go down tremendously. These properties of the pad material make it an ideal high-pass filter, which filters out environmental noise and makes the frequency range of vibrations relevant for the spider most effective.

CHAPTER 5

SPIDER AIR FLOW RECEPTOR STUDY

5.1 Introduction

Trichobothria are wind sensing hair-like sensilla on the legs and pedipalps of spiders capable of absorbing the energy of air flowing around them with outstanding efficiency.^{129,155,156} They serve the spider to detect and localize prey and predators. The measurements reported to date on spider trichobothria have been used in physical-mathematical models describing mechanical hair behaviour for oscillating air flows in the biologically relevant frequency range between 10 and 950 Hz. In earlier studies the frequency dependence of hair deflection was explained considering factors such as the relation of hair morphology to boundary layer thickness and inertial effects. The hair suspension torsional restoring constant, S , and the damping constant, R , were calculated to be extremely small, being $S = 5.77 \times 10^{-12} \text{ Nm rad}^{-1}$, and $R = 2.20 \times 10^{-15} \text{ Nm s rad}^{-1}$ for a 750 μm long hair, and $S = 0.62 \times 10^{-12} \text{ Nm rad}^{-1}$, and $R = 0.27 \times 10^{-15} \text{ Nm s rad}^{-1}$ for a 250 μm long hair.¹⁵⁷

To date, trichobothria have been modelled using data acquired by conventional optical microscopy, scanning electron microscopy, and laser Doppler anemometry.^{157,158} The mechanical hair behaviour was modelled using fluid mechanics to predict the amount of mechanical energy transferred from the air flow to the hair.^{156,157,159,160,161,162,163} These considerations quantitatively described the air-hair phase relationship, which allows the

torsional restoring force of the hair suspension to be calculated under various assumptions related to air–hair interactions. From the minimum deflection (measured with the optical microscope) that elicits an action potential combined with estimates of the torsional restoring constant S , the minimum mechanical energy that effectively elicits a nervous response was estimated to be between 1.5×10^{-19} and 2.5×10^{-20} J.¹⁶² These are extremely small values indicating that trichobothria are among the most sensitive biological receptors.

In the present study the mechanical properties of the trichobothrium suspension and of the hair shaft proper are measured directly. Mechanical stimuli were applied in different spatial and temporal regimes for both small nanoscale deflections and larger, microscale deflections, and for a wide range of angular deflection velocities ranging from 0.0004 to 0.26 rad s⁻¹ at triangular wave frequencies ranging from 0.07 to 102 Hz (calculated as the reciprocal value of the duration of the triangular displacement). Moreover, this study is conducted with particularly high experimental precision (fraction-of-nanometre) by utilizing surface force spectroscopy (SFS) and the application of directly calibrated forces in the range of nano-Newtons. SFS provides a force spectrum with pico-Newton precision, nano-Newton applied forces, and nanoscale deflections.¹⁶⁴ SFS has already proven to be an invaluable tool for studying biological receptors and the structures associated with them.^{165,166,167,168} Here we report on a methodology that combines representing the suspension of a trichobothrium as a linear viscoelastic material with direct measurements to determine the values of the three-parameter ($3p$) and two-parameter ($2p$) viscoelastic models explored. These are the torsional restoring constants, S_{3p} and S'_{3p} , and the damping constant R_{3p} , and the torsional restoring constant S_{2p} and

the damping constant R_{2p} , inherent to the trichobothrium suspension represented by the spring and the dashpot elements of the models. The angles and velocities of the trichobothrium deflections measured are within the range relevant for the spider to distinguish air flow stimuli originating from prey, mates, and predators from its noisy environment.

5.2 Materials and Methods

5.2.1 Sample Preparation

Live adult female *Cupiennius salei* (Ctenidae) spiders, see figure 5.1a, from the Vienna laboratory stock were anesthetized with a CO₂/air mixture for 5 minutes and then attached to a Perspex substrate using adhesive tape (3M Micropore), such that the metatarsus and tarsus of one of their first legs protruded beyond the substrate. Trichobothria on the tarsus of the first walking leg were identified optically (TaD group; for details of trichobothria topography see a prior publication¹⁵⁷) and other hairs in their vicinity removed (figure 5.1b). Particularly two to four of the most distal trichobothria in the most frontal row on the tarsus were prepared in this way. For technical reasons the tarsus was secured on a metal sample mounting disk, so that the long axes of the trichobothria were oriented horizontally. To avoid mechanical interference with the atomic force microscope's (AFM) cantilever and to minimize air drag forces the trichobothria were cut to lengths of about 100 μm and less using micro-scissors. The lengths of the trichobothria were measured using an optical microscope (Leica DM4000M) before and after the cutting procedure. A piece of silicon wafer cleaned with "piranha solution" (1:2 hydrogen peroxide: sulphuric acid) was mounted beside the

spider's tarsus on the metal disk. This was done to calibrate the sensitivity of the photodetector which measures the cantilever deflection used in SFS experiments. This is explained in detail in section 5.2.2. Following the SFS measurements, the tarsus together with the trichobothrium tested was examined in a scanning electron microscope (JEOL JSM-6060V) for changes of the hair's surface structure due to the interaction with the AFM cantilever probe.

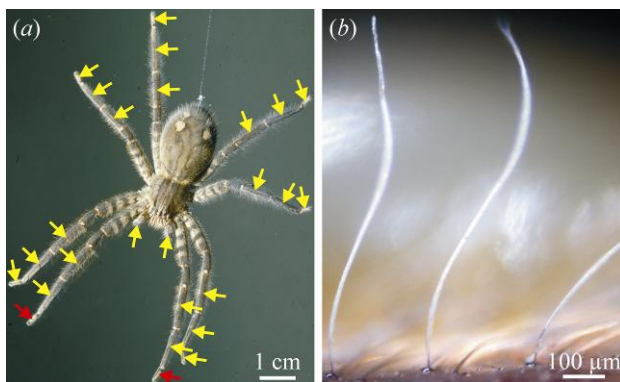


Figure 5.1: The spider and Trichobothria. (a) An adult female *Cupiennius salei*. The yellow arrows point to the leg segments carrying trichobothria. The red arrows point to the tarsi of the first walking legs whose trichobothria were examined in this study. (b) Three trichobothria in a row on the dorsal side of the first walking leg tarsus

5.2.2 SFS-Hair deflection Measurements

All AFM and SFS measurements were performed using a Multimode, Nanoscope IIIa microscope with a Picoforce module and a Dimension 3000, Nanoscope IIIa microscope in accordance with well established procedures.^{169,170,171}

The AFM was warmed up by actuating the piezo-elements for at least 30 minutes before the measurements began in order to prevent piezo thermal drift. The quadrant photodiode, which measured the deflection of the AFM cantilever, was calibrated by relating the distance of the cantilever tip deflection and the change in position of the laser

light shone on the photodiode. To calibrate the sensitivity of the photodiode, force curves were determined on a clean piece of silicon. A simple equation was used, $P + D = PM$, which relates the sum of the cantilever tip penetration into the substrate, P , and its deflection, D , to the movement of the piezo-element PM . The freshly cleaned silicon was considered an infinitely hard surface. Thus the cantilever tip penetrated into the silicon by a negligible amount ($P = 0$), and the piezo movement equalled the deflection of the cantilever tip ($PM = D$). The voltage change in the photodiode was due to the same amount of deflection of the cantilever as the movement of the piezo-element. Therefore, the photodiode was calibrated by setting the slope of the force-distance curve on silicon to 1. The photodiode was calibrated every time a new cantilever was used. Further details regarding calibration procedures are presented in Chapter 3.

For the measurements silicon cantilevers back-side coated with aluminium and with silicon nitride tips (nanometre-scale radius of cantilever tip end curvature) were used. Initially, microsphere-tipped probes seemed the most appropriate to prevent penetration into the hair surface, but due to the large surface contact area adhesion of the hair to the microsphere persisted between two measurement cycles. The loss of contact between two measurements provided a reference point when quantifying the total deflection of the hair during a measurement. The spring constants of the AFM cantilevers were calibrated using the standard “tip-on-tip” method, as well as the thermal tuning method for softer cantilevers.^{140,172,173,174,175}

For all measurements, the trichobothria were loaded by deflecting them in a triangular way at a constant angular velocity, with a predetermined repeat frequency and perpendicular to the long axis of the hair shaft. The hair shaft was deflected towards the

posterior aspect of the tarsus. In oscillating air the mechanical directional characteristics of hair deflection are nearly isotropic for the hairs examined here, with only a slight preference for the anterior-posterior plane (large to medium sized hairs).¹⁵⁷

The trichobothria and the AFM cantilever were positioned under optical control (fibre optics, magnification by objective lens $\times 50$ with large working distance, observation on video monitor). The metal disk, with the sample and the silicon, was placed onto the magnetic sample holder so that the long axis of the hair and the cantilever were in parallel. The micro-positioning stage of the AFM was used to position the cantilever with respect to the hair. Then the tip position was fine adjusted to land in the centre of the hair. This was achieved by adjusting the offset of the horizontal plane piezo-elements of the AFM to minimize the torsional deflection of the cantilever (monitored with the quadrant photodiode). The torsional motion was caused by a twisting motion of the cantilever when it contacted the hair not on its centre.

All hairs (of 910, 923, 950 μm length before cutting) were initially loaded using soft AFM cantilevers (spring constants between 0.018 and 0.045 N m^{-1}) to limit the forces applied to several nano-Newtons and to keep deflections below 100 nm. However, after the initial engagement, the force-distance curves showed significant instabilities caused by interactions between the AFM cantilever tip and the microtrichs on the main hair shaft (figure 5.2a,b). Repetition of the loading with the AFM cantilever tip at 1 Hz effectively micro-shaved the hair shaft due to the cantilever's slight horizontal displacements relative to the hair shaft, making the selected surface areas smooth and acceptable for stable engagement of the AFM cantilever tip (figure 5.2c). Because this horizontal displacement of the AFM cantilever (which can change the effective distance

to the pivotal point and thus the resistance forces measured) was very small, it did not affect the calculations. Indeed, for hair deflection angles below 0.1 deg for high resolution measurements, and below 12 deg for large deflection measurements, the corresponding correction factor was estimated to fall within 1 to 10 %. All critical experimental conditions are summarized in table 5.1. The cantilever force-distance curves were converted to hair loading curves (hair deflection vs. normal load) by taking into account the preceding cantilever calibration. The contact point was defined in accordance with an adaptation of the well established approach given in a previous publication.¹⁷⁶ Specifically, we utilized the minimum deflection point of the approach curve, where the cantilever “snaps into” the surface of the hair.

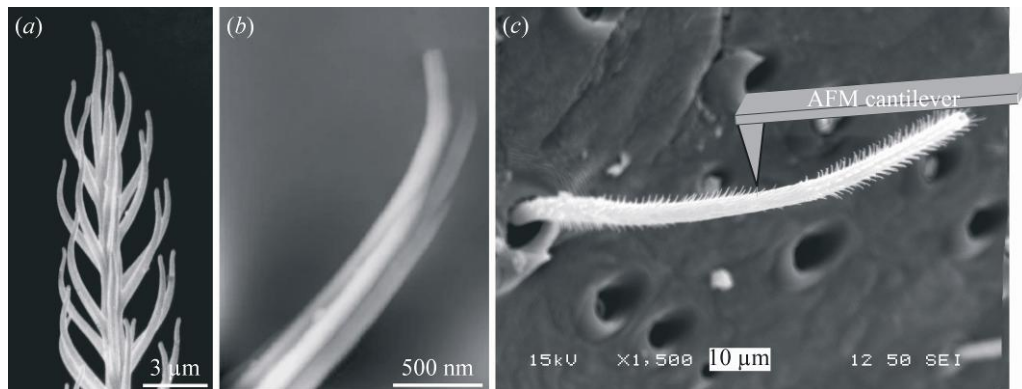


Figure 5.2: Hair shaft morphology. (a) SEM micrograph of the tip of a trichobothrium; notice the hairs-on-hair morphology (microtrichs). (b) High resolution AFM image of a single microtrich (z-range 100 nm). Notice that several striations make up a single microtrich. (c) SEM micrograph of a trichobothrium with partially removed microtrichs in the area close to the cantilever tip. Notice the bald spot where the microtrichs were rubbed off by the cantilever tip (nanoshaving).

After performing the high resolution SFS measurements within the limited range of deflections and forces, the soft AFM cantilever (spring constant $\leq 0.045 \text{ N m}^{-1}$) was replaced with a stiffer cantilever that had a spring constant of 8.9 N m^{-1} . The stiff

cantilever allowed for loading forces exceeding $0.5 \mu\text{N}$ and led to hair deflections from 1 nm to $10 \mu\text{m}$. The measurements done with large hair deflections and the shaft-bending measurements were performed with and without a deflection trigger point (which is the maximum cantilever deflection before the displacement of the piezo-element changes direction) to achieve the widest possible ranges of deflections and bending, respectively (figure 5.3, table 5.1).

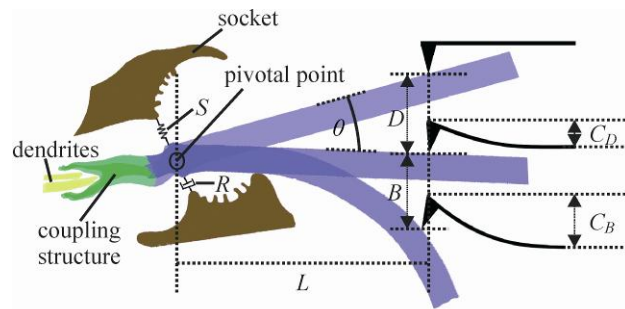


Figure 5.3: Hair parameters used for the Calculations. The drawing defines the geometrical variables for the two regimes investigated: hair pivoting (deflection only) D and bending B , and the corresponding cantilever deflections C_D and C_B . L denotes the distance of the AFM cantilever tip from the pivotal point, θ denotes the deflection angle. The torsional restoring element S is represented by a spring, and the damping element R by a dashpot.

For the theoretical considerations in the following paragraph it is important to state that each force measurement curve was obtained at a constant angular velocity ($\dot{\theta}$) and thus zero angular acceleration ($\ddot{\theta}$).

Table 5.1. Experimental Conditions for SFS measurements

testing variables	length, L^* (μm)	AFM cantilever stiffness (N m^{-1})	ramp size** (nm)	velocity ($\mu\text{m s}^{-1}$)	trigger*** (nm)
small forces (< 10 nN)	20 – 50	0.018 – 0.045	3000 – 5000	0.05 – 41.9	10 – 150
large forces (> 500 nN)	21 – 62	8.9	5000 – 20000	5 – 20	60 – none

* The position of the cantilever on the hair is essential for the calculation of the torque.

** Ramp size is the maximum distance that the sample can travel vertically when a single force-distance curve is measured. Ramp sizes had to be very large to ensure that the cantilever loses contact with the hair between measurements.

*** The trigger defines the maximum deflection of the cantilever when recording a force-distance curve.

5.2.3 Theoretical determination of the viscoelastic model parameters

In this section we obtain two equations for the angular momentum of a trichobothrium. One, based on a three-parameter solid model for the viscoelastic hair suspension, will be shown to apply over the entire range of angular velocities explored ($4 \times 10^{-4} < \dot{\theta} < 2.6 \times 10^{-1} \text{ rad s}^{-1}$). The other, based on a two-parameter Kelvin solid model, will be shown to predict the motion of a hair with much better accuracy for angular velocities $\dot{\theta} > 0.05 \text{ rad s}^{-1}$, which is in the biologically most relevant range. For ease of presentation, we describe the two-parameter model first.

5.2.3.1 Two-parameter Kelvin solid model

In this approach, the suspension supporting the hair is approximated as a two-parameter Kelvin solid model consisting of a spring and a dashpot element connected in

parallel (figure 5.4a). The hair is assumed to behave as a simple forced damped harmonic oscillator for which the conservation of angular momentum is given by

$$I\ddot{\theta} + R_{2p}\dot{\theta} + S_{2p}\theta = T \quad (\text{Equation 5.1})$$

where I ($\text{Nm s}^2 \text{rad}^{-1}$) is the hair's moment of inertia, R_{2p} (Nm s rad^{-1}) is the hair damping constant, S_{2p} (Nm rad^{-1}) is the hair's torsional restoring constant, T (Nm) is the torque applied to the hair, and θ (rad), $\dot{\theta}$ (rad s^{-1}), and $\ddot{\theta}$ (rad s^{-2}) are the hair's deflection angle, angular velocity, and angular acceleration, respectively. The subscript notation “2p” denotes “two-parameter” model. Using this model, we show in the appendix that the torque terms associated with air friction and air added mass are negligible relative to the torque T_{SFS} imposed by the mechanical probe. The smallness of these effects is further confirmed by the fact that the loading curves showed no non-linearities that could be due to these two medium-related forces.

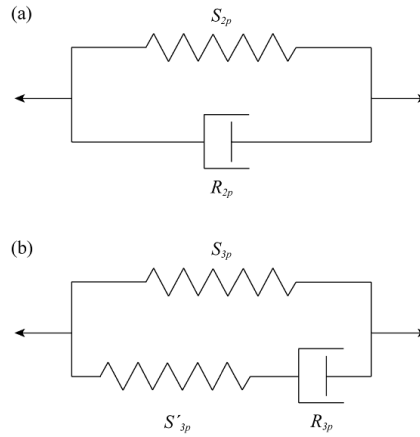


Figure 5.4: “Spring” and “dashpot” Representations. of (a) the two-parameter and (b) the three-parameter viscoelastic models representing the trichobothrium suspension material. In (a) the spring constant S_{2p} and the dashpot constant R_{2p} refer to the two-parameter model constants. In (b) the two spring constants S_{3p} and S'_{3p} , and the dashpot constant R_{3p} refer to the three-parameter model constants.

Each experiment was conducted at a predetermined constant angular velocity $\dot{\theta}$, and as a consequence, equation 5.1 simplifies to

$$R_{2p}\dot{\theta} + S_{2p}\theta = T_{SFS} \quad (\text{Equation 5.2})$$

Using the experimentally determined data for $\dot{\theta}$ and T_{SFS} at a fixed angle θ a multiple linear regression was performed using equation 5.2 to determine the model parameters.

5.2.3.2 Three-parameter solid model

The inability of the two-parameter model to correctly capture the variation of the hair's torque over the full range of angular velocities prompted us to explore a three-parameter solid model consisting of a spring element in parallel with a spring and a dashpot element in series (figure 5.4b). This type of linear viscoelastic model is documented in several publications,^{165,177,178} for example, and the corresponding angular momentum equation for a trichobothrium is given by

$$I\ddot{\theta} + R_{3p}\left(1 + \frac{S_{3p}}{S'_{3p}}\right)\dot{\theta} + S_{3p}\theta = T + \frac{R_{3p}}{S'_{3p}}\dot{T} \quad (\text{Equation 5.3})$$

In this case the model parameters are the damping constant R_{3p} (Nm s rad⁻¹) and two torsional restoring constants S_{3p} (Nm rad⁻¹) and S'_{3p} (Nm rad⁻¹). Here the subscript notation “3p” stands for “three-parameter”, and was chosen to distinguish from the “2p” of the “two-parameter” model. The quantity $\dot{T} = \left(\frac{dT}{dt}\right)$ is the time rate of change of the torque. This is estimated from the relation $\dot{T} \cong \frac{T_{tot}\dot{\theta}}{\theta_{tot}}$ where $\dot{\theta}$ and θ_{tot} are, respectively, the angular velocity and the total angular deflection of a hair during a measurement, T_{tot}

(= T_{SFS}) being the corresponding experimentally determined torque for these conditions. As mentioned above, for the conditions of this study $\dot{\theta}$ is fixed to different but constant values and equation 5.3 simplifies to

$$R_{3p} \left(1 + \frac{S_{3p}}{S'_{3p}} \right) \dot{\theta} + S_{3p} \theta = T_{SFS} + \frac{R_{3p}}{S'_{3p}} \dot{T}_{SFS} \quad (\text{Equation 5.4})$$

Again, as in the two-parameter model, a multiple linear regression analysis was performed on the experimental data using equation 5.4 to determine the model parameters.

5.2.4 Testing Methodology: Nanoshaving

All SFS measurements were done with live animals. The micro-hairy surface (microtrichs) on the shaft of the trichobothrium added a significant challenge (figure 5.2). As mentioned above, the hairs-on-hair morphology initially prevented the acquisition of stable force-distance curves appropriate for further analysis. After taking many force-distance curves, their quality improved significantly as a result of nanoshaving. The linear region of the extension curves after engagement of the cantilever tip had identical slopes before and after this routine indicating that the fundamental hair resistance did not change (figure 5.5a,b).

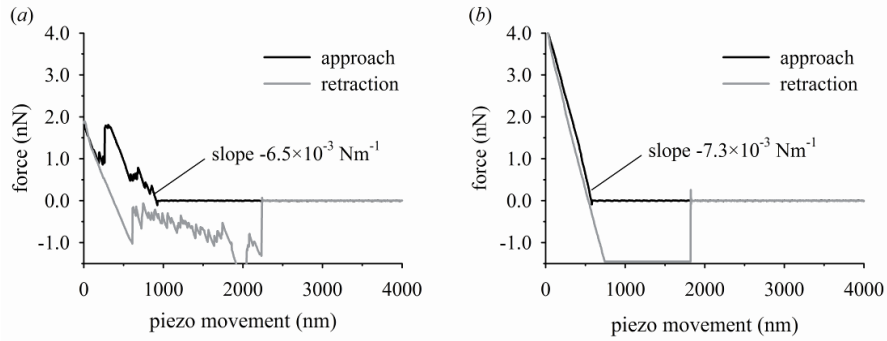


Figure 5.5. Hair shaving (a) A force-distance curve obtained before the hair was shaved. (b) A force-distance curve obtained after removal of the microtrichs. The velocity of the piezo movement was $5.58 \mu\text{m s}^{-1}$. Notice the significant improvement in data quality compared to that in (a). The approach curves in (a) and (b) should be read from right to left, and the retraction curves from left to right.

For the experimental conditions of most of the SFS measurements on shaved hairs we recorded very steady hair deflection, completely controlled by linear displacement of the piezoelectric crystal with random deviations smaller than 0.2 nm. No detectable thermal vibrations were recorded in the range of forces and distances examined, indicating significant viscous damping of the thermal vibrations and any other random deflections associated with environmental noise present in the lab. Moreover, no indications of large-scale displacements, associated with macroscopic movements, were recorded, indicating firm immobilization of the leg of the live spider.

5.2.5 Testing Methodology: Location of the axis of rotation

In order to measure the torque to deflect the trichobothrium, the distance, L , from its pivoting axis, O , to the region where the AFM cantilever tip contacted the hair shaft was required (figure 5.3). Precise values were obtained by making force-distance measurements at varying points along the hair shaft. From the zero position, the hair was deflected until its shaft contacted the socket at the limiting angle θ , and finally was bent

slightly (figures 5.3, 5.6a). The angle between the hair in its zero position and when touching the socket was used to identify the axis of rotation O . When the cantilever tip was moved towards or away from the hair suspension, the triangle described by the motion of the pivoting lever arm of length L changed area, but not angles. By changing the distance of the measurement location from the pivoting axis, the two lines representing the surface of the hair shaft at rest and at fully deflected states, respectively, were mapped out (figure 5.6b). The intersection of the two lines represents the location of the pivoting axis. The error regarding the distance from the AFM cantilever tip to the hair pivoting axis was estimated by taking the error of optical microscopy to be less than $\pm 1 \mu\text{m}$ for most SFS measurements conducted here.

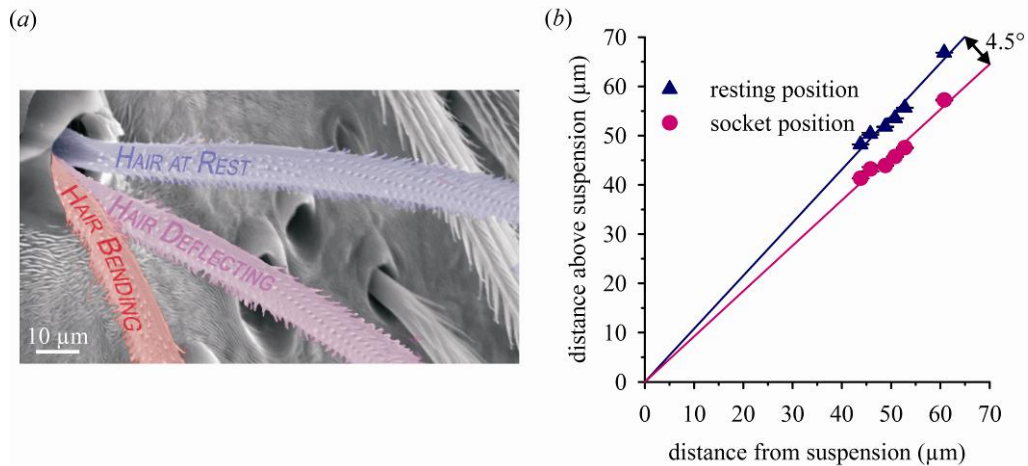


Figure 5.6: Locating the Pivot Position (a) SEM micrograph depicting the three regimes which characterize the large scale load curves shown in figure 5.7a. (b) Positions of the trichobothrium in its zero position (blue triangles) and positions of first contact of the hair shaft with the socket rim (red circles) with lines fit to the data. The origin of the curve represents the position of the hair-suspension ($N=1$, $n=30$) (N number of trichobothria, n number of measurements).

Once the location of the pivoting axis was obtained, calculating the torque, T , resisting hair deflection became unambiguous. The length of the hair shaft between the

outer edge of the socket and the pivoting axis located at the suspension membrane was $12 \pm 1 \mu\text{m}$. This data is in good agreement with previous results, where the length of the hair shaft inside the socket was determined morphologically to be $10 - 15 \mu\text{m}$ for large trichobothria.¹⁵⁷

5.2.6 Testing methodology: Deflection of a rigid hair

The force necessary to deflect the hair by a unit amount was measured by positioning the AFM cantilever tip at varying points along the length of the hair shaft and acquiring force-distance curves as discussed above. The results of the hair deflection measurements at small forces ($< 500 \text{ nN}$) were based on two key assumptions; (i) the hair shaft does not bend in this regime; and (ii) the AFM cantilever tip does not penetrate into the cuticle of the hair shaft.

Both assumptions were verified prior to the SFS measurements. The absence of hair bending under the nano-Newton forces used for high resolution studies was confirmed by measurements of hair deflection under identical forces at various distances along the hair. The increase of hair deflection was linear at all the different distances from the pivotal axis for the same range of forces applied, which confirmed that the hair was deflected but not bent. The absence of local hair indentation was validated by performing independent SFS measurements on a hair that had been plucked and immobilized on a rigid substrate (silicon), considered to be infinitely hard. Under the modest normal loads used here, the indentation depth, if any, was close to the experimental uncertainty. It did not exceed 1 nm at the largest load and therefore only slightly penetrated into the topmost layer of the epicuticle leading to the adhesion seen in

the retraction curves of the force-distance measurements (figure 5.5b). The thickness of the epicuticle on the leg of *Cupiennius* is 200 nm, with a thickness of the lipid layers of 10 to 40 nm.^{167,179} By its smallness the penetration into the epicuticle did not contribute to the deflection measurements. The hair was deflected like a rigid rod with its large stiffness relying mainly on the stiffness of the exocuticle, which has an elastic modulus of about 18 GPa in *Cupiennius salei*.^{129,180}

5.3 Results

5.3.1 Measuring the torques resisting hair motion

The micromechanical behaviour of a hair under maximum forces normal to the long axis of the hair shaft and reaching 500 nN is presented in figure 5.7a. The complex and nonlinear loading curve reflects the contribution of several different mechanical regimes. First, the deflection of the hair just before making contact with the AFM cantilever tip is zero (figure 5.7b). Then, immediately after the engagement of the AFM cantilever tip at the contact point, the hair starts its nanoscale deflection, which is noisy but essentially linear up to loads close to 100 nN. The irregular deflections observed are caused by the interaction of the AFM cantilever tip with the microstructure of the hair shaft surface (see section 5.2, figure 5.2a).

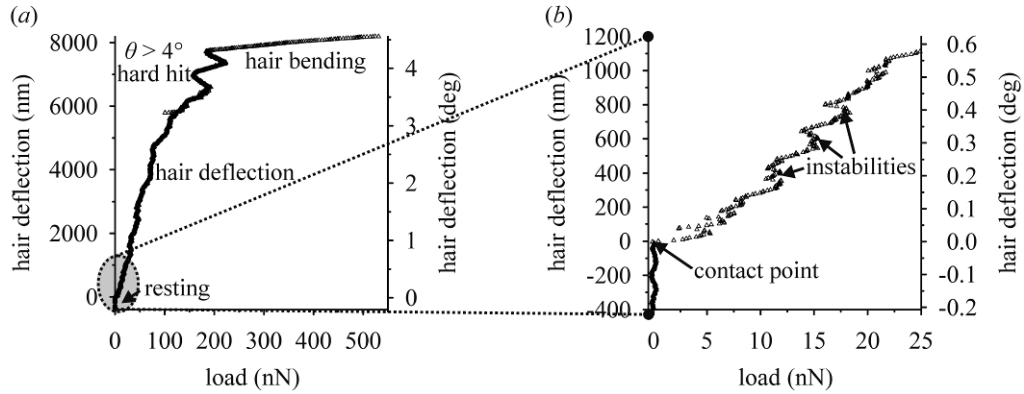


Figure 5.7: Hair Shaft Bending. (a) A load – hair deflection curve, utilizing relatively large forces. After significant deflection the hair made contact with the socket and then the hair shaft was bent as seen from the small slope of the curve. (b) The same load curve as in (a), with the initial part of the curve enlarged to show the region where the AFM cantilever tip contacts the hair shaft.

At larger normal loads hair deflection becomes erratic, especially between 7000 nm and 8000 nm, and finally alters dramatically (figure 5.7a). The erratic behaviour around 7000 nm deflection is likely due to several different surface patches of the hair contacting the inner parts of the socket. For deflections larger than 7500 nm, the force required to deflect the hair further increases steeply indicating a change in the hair's mechanical behaviour. Figure 5.7a and b reflect the overall hair behaviour observed in our large deflection experiments: steady, close to linear deflection as a rigid body for deflections of less than about 7500 nm, followed by a steep increase in mechanical resistance when the hair contacts the socket rim and starts bending. The bending stiffness of the hair shaft of the 950 μm long trichobothrium, selected as a representative example, was measured to be $0.18 (\pm 0.03) \text{ N m}^{-1}$ ($n=15$), the AFM cantilever tip being 43.8 μm from the hair suspension membrane. The overall quadratic relation for the bending

stiffness k of the hair shaft, as a function of distance from the pivoting point, L in μm , was $k = 3.38 \times 10^{-4} L^2 - 4.35 \times 10^{-2} L + 1.44$ (N m^{-1}).

Considering the significant instabilities observed in the micromechanical behaviour measured under large deflection conditions, we conducted high resolution experiments with more flexible cantilevers after nanoshaving the microtrichs to obtain the deflection characteristics in the range of very small forces (less than 2 nN). Under these conditions, the hair deflected fairly linearly with the force changing from 12.5 pN to 1.5 nN (figure 5.8a,b). Note that the first point in figure 5.7b is beyond the 0.5 nm uncertainty of the SFS measurement technique and therefore well measurable. The loading curve is directly related to the torque resisting hair deflections by multiplying the force with the length of the lever arm. The trichobothrium could be reproducibly deflected by 0.001 deg (17.5 μrad). This is an extremely small value, well below the sensory threshold deflection angle down to 0.01 deg.¹⁸¹ Hair deflection at small forces changed linearly by 0.85 nm increments per each 12.5 pN increase in load (figure 5.8b). The mechanical response of the hairs was linear at the specific angular velocities, even well below the sensory threshold deflection. Moreover, even under very small piconewton forces the hair response was smooth, with a mean deviation from linearity on the order of ± 0.2 nm (figure 5.8b).

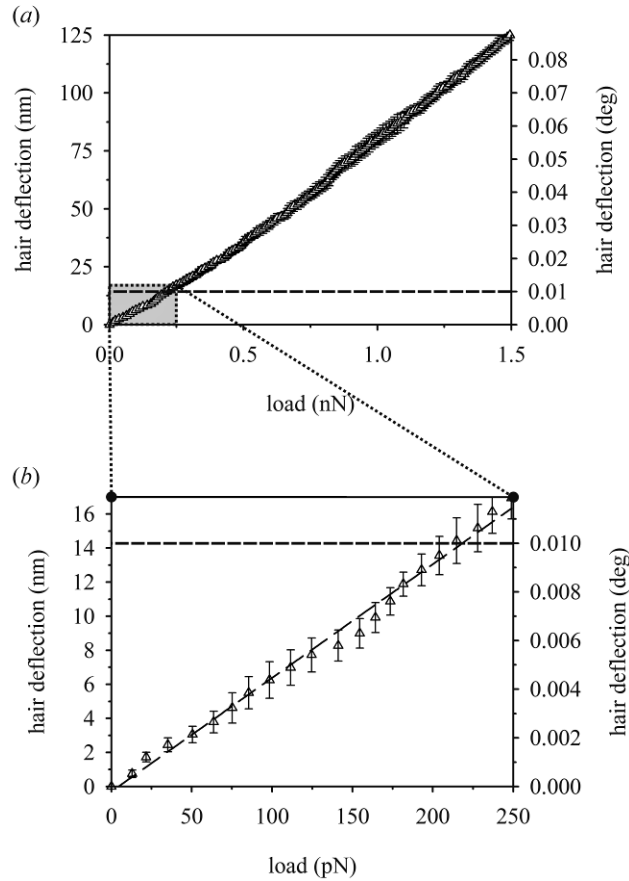


Figure 5.8: High Resolution Hair Shaft Deflection Measurements. for a hair shortened to 114.5 μm (a) High resolution load – deflection curve; example of the load curves used to determine the two- and three-parameter model constants. Average of 5 measurements (\pm SD) obtained at an angular velocity of $0.029 \pm 0.004 \text{ rads}^{-1}$. The dashed horizontal line represents the minimum angle of deflection necessary to elicit a nervous response as measured electrophysiologically.¹⁸¹ (b) Enlarged initial region of the load – deflection curve displayed in (a).

5.3.2 Viscoelastic model parameters

Preliminary values of the torsional restoring constant S , in which the contribution of the torque associated with damping was neglected, were obtained by relating the slope of the loading curves to a unit hair deflection of 1 rad. Previous data^{159,160} and current findings suggest that values of the torsional restoring constant S obtained this way are close to the true values, although slightly overestimated. In investigations of hairs 910

μm long and $923 \mu\text{m}$ long, the preliminary torsional restoring constants were measured to be $7.3 \times 10^{-12} (\pm 0.6 \times 10^{-12}) \text{ Nm rad}^{-1}$ and $4.3 \times 10^{-12} (\pm 0.1 \times 10^{-12}) \text{ Nm rad}^{-1}$, respectively.

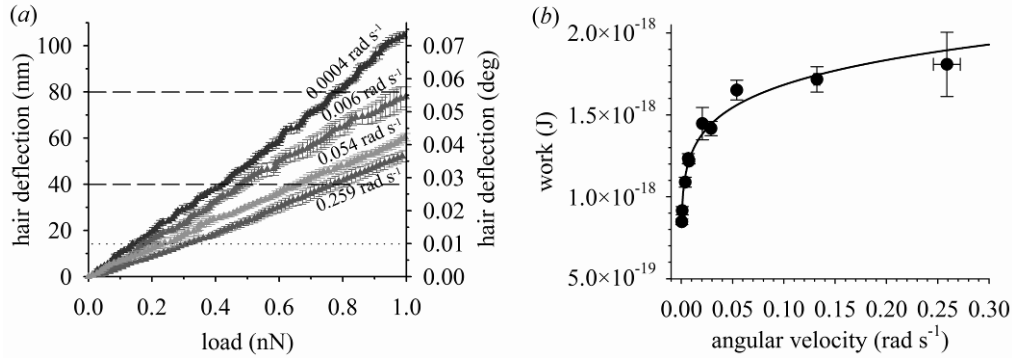


Figure 5.9: Dependency of Load-Deflection and Work on Angular Velocity. (a) High resolution load – deflection curves. At lower angular velocity the hair pivots much more with force. The curves shown are average curves \pm SD ($N=1$, $n=12$). (b) Work to reach the physiological threshold deflection of 0.01 deg ,¹⁸¹ see dotted line in (a). The line fitted to the data points (circles) follows the power law function of work $W = 2.24 \times 10^{-18} \times \dot{\theta}^{0.124}$ with an average overall uncertainty of 2.6%.

Given the potential importance of a trichobothrium’s mechanical properties for its physiological response, we studied its torsional behaviour at angular velocities between 0.0004 and 0.26 rad s^{-1} by collecting force-distance data in the high resolution mode (figure 5.9a). Surprisingly, the mechanical resistance of a hair to deflection forces, and consequently the work to deflect it to the physiological threshold angle, dropped sharply for angular velocities smaller than 0.05 rad s^{-1} (figures 5.9b & figure 5.10a). To the authors’ knowledge no previous work has reported such a trend in arthropod air flow-sensing hair receptors.

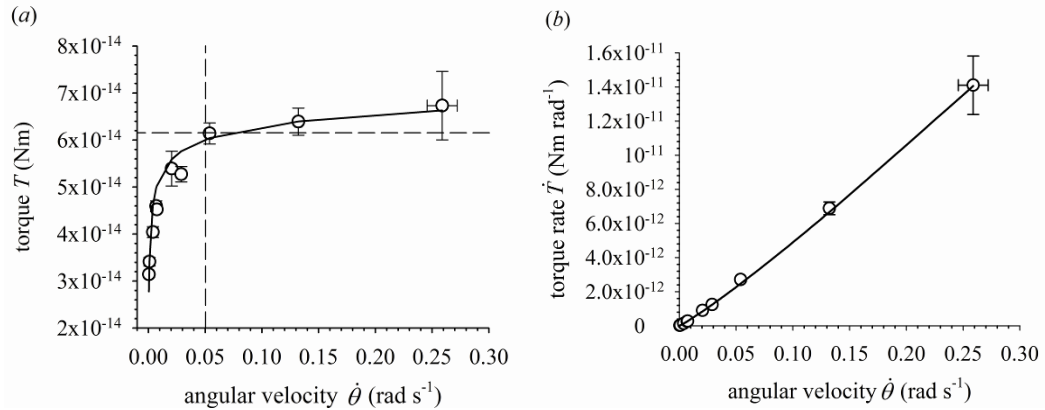


Figure 5.10: Comparison of Measurements and Empirical Fits. (a) the torque and (b) its time rate of change as a function of the hair's angular velocity. Measurements (circles; mean \pm SD) and empirical fits (lines; equations are given in the text).

Table 5.2 provides mean and *r.m.s.* (root mean square) values of the experimental angular velocity, the torque, and the time rate of change of torque from which the viscoelastic model parameters were determined. The torque values at a fixed hair deflection angle of 1.23×10^{-3} rad (0.07 deg) (which was the maximum angle that could be achieved at all deflection velocities with the same trigger deflection of the AFM's cantilever) are empirically related to the angular velocity by the expression $T = 8.50 \times 10^{-14} - 1.48 \times 10^{-14} \dot{\theta}^{-0.174}$ (Nm) (figure 5.10a). The empirical fit predicts the torque with an absolute percent difference smaller than 6 % over the entire range of angular velocities explored. The time rate of change of torque is empirically given by $\dot{T} = 6.30 \times 10^{-11} \dot{\theta}^{1.11}$ (Nm s $^{-1}$) (figure 5.10b), with an absolute percent difference smaller than 4 %. We note that the torque, T , tends towards an asymptotic value of 8.50×10^{-14} Nm for very large angular velocities. This is to be expected since the viscoelastic dashpot element resists deformation induced by motions at high angular velocities and, as a consequence, deformation can only occur due to the spring elements. The latter, however, deform in

proportion to the torque irrespective of the rate of change and are responsible for the asymptotic behaviour observed.

Table 5.2. Angular velocity $\dot{\theta}$, torque T , and torque rate of change \dot{T} (mean \pm *r.m.s.* values) for a shortened trichobothrium originally 950 μm long at a deflection angle fixed to $\theta_{tot} = 1.226 \times 10^{-3}$ rad (N=1, n=81)¹

data point	angular velocity	torque	torque rate
	mean (rad s ⁻¹)	mean (Nm)	mean (Nm s ⁻¹)
1	4.20 \pm .0225 $\times 10^{-4}$	3.14 \pm .0609 $\times 10^{-14}$	1.08 \pm .0306 $\times 10^{-14}$
2	8.17 \pm .0743 $\times 10^{-4}$	3.41 \pm .0922 $\times 10^{-14}$	2.27 \pm .0791 $\times 10^{-14}$
3	3.84 \pm .0404 $\times 10^{-3}$	4.04 \pm .115 $\times 10^{-14}$	1.27 \pm .0461 $\times 10^{-13}$
4	6.81 \pm .0665 $\times 10^{-3}$	4.59 \pm .112 $\times 10^{-14}$	2.55 \pm .0841 $\times 10^{-13}$
5	7.37 \pm .0378 $\times 10^{-3}$	4.52 \pm .0578 $\times 10^{-14}$	2.72 \pm .0660 $\times 10^{-13}$
6	2.05 \pm .0607 $\times 10^{-2}$	5.39 \pm .370 $\times 10^{-14}$	8.97 \pm .694 $\times 10^{-13}$
7	2.89 \pm .0399 $\times 10^{-2}$	5.27 \pm .164 $\times 10^{-14}$	1.24 \pm .0490 $\times 10^{-12}$
8	5.39 \pm .0940 $\times 10^{-2}$	6.14 \pm .225 $\times 10^{-14}$	2.70 \pm .122 $\times 10^{-12}$
9	1.32 \pm .0284 $\times 10^{-1}$	6.39 \pm .290 $\times 10^{-14}$	6.88 \pm .372 $\times 10^{-12}$
10	2.59 \pm .132 $\times 10^{-1}$	6.73 \pm .730 $\times 10^{-14}$	1.41 \pm .171 $\times 10^{-11}$

¹ The rate of change of the torque is determined as explained in the text and its *r.m.s.*

from the expression $\sigma_{\dot{T}_{SFS}} = \dot{T}_{SFS} \left(\frac{\sigma_{T_{SFS}}^2}{T_{SFS}^2} + \frac{\sigma_{\dot{\theta}}^2}{\dot{\theta}^2} + \frac{\sigma_{\theta_{tot}}^2}{\theta_{tot}^2} \right)^{\frac{1}{2}}$ where σ denotes *r.m.s.* value. In

this formula, the *r.m.s.* values for T_{SFS} and $\dot{\theta}$ are taken from the table entries, and that for θ_{tot} is estimated to be 2.45×10^{-5} rad from the experimental uncertainties of lever arm length and instrumental inaccuracies of the AFM.

Using the physical-mathematical procedure described in section 5.2.3.1 for the two-parameter Kelvin model applied to all measured data points, the model parameters were found to be $S_{2p} = 3.57 \times 10^{-11}$ ($\pm 8.08 \times 10^{-12}$) Nm rad⁻¹ and $R_{2p} = 1.15 \times 10^{-13}$ ($\pm 1.05 \times 10^{-13}$) Nm s rad⁻¹. To check the goodness of this model, the torque T_{SFS} was

calculated using equation 5.2 for the values of $\dot{\theta}$ in table 2 and the values obtained for S_{2p} and R_{2p} . The absolute percent difference between the measurements and the calculations averaged over the entire range of angular velocities is 14 %, reaching values as high as 39 % at the smallest angular velocity. Because of the poor agreement, especially at low angular velocities, a second regression was performed using only the data corresponding to $\dot{\theta} > 0.05 \text{ rad s}^{-1}$. From this it was found that $S_{2p} = 4.89 \times 10^{-11} (\pm 2.88 \times 10^{-13}) \text{ Nm rad}^{-1}$ and $R_{2p} = 2.83 \times 10^{-14} (\pm 2.07 \times 10^{-15}) \text{ Nm s rad}^{-1}$, which yielded calculated values of T_{SFS} differing from those measured by less than 0.5 % (figure 5.11).

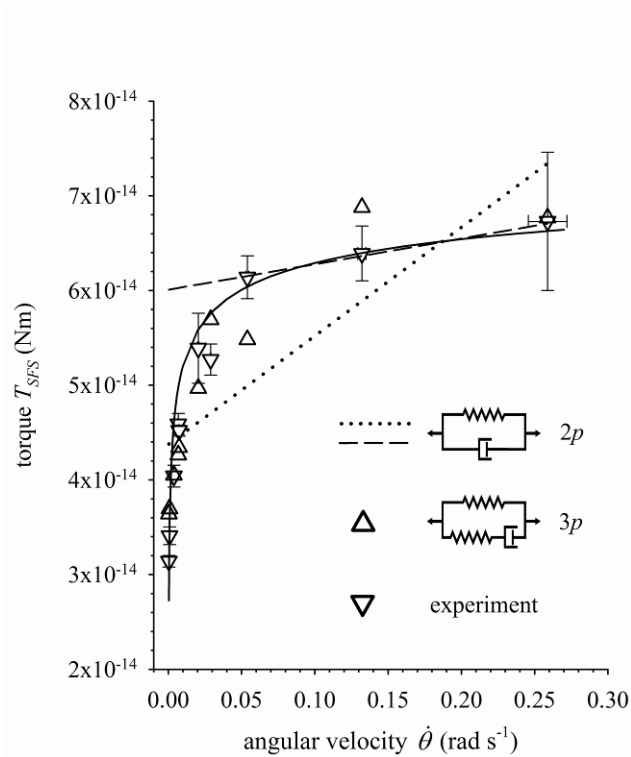


Figure 5.11: Comparison between Measurements and Models. Calculations of the torque acting on a spider trichobothrium using the two-parameter ($2p$) and the three-parameter ($3p$) models described in the text. Measured data (triangles pointing downward, with error bars); empirical fit (black solid line); values calculated using the two-parameter model fitted to all measured data points (dotted line); values calculated using the two-parameter model fitted to the three points at angular velocities larger than 0.05 rad s^{-1} (dashed line); values calculated using the three-parameter model fitted to all measured data points (triangles pointing upward)

For the three-parameter solid model described in §2.3.2 the multiple linear regression of the measured data in table 2 using equation 5.4 yielded $S_{3p} = 2.91 \times 10^{-11}$ ($\pm 6.55 \times 10^{-12}$) Nm rad⁻¹, $S'_{3p} = 2.77 \times 10^{-11}$ ($\pm 9.84 \times 10^{-12}$) and $R_{3p} = 1.46 \times 10^{-12}$ ($\pm 9.26 \times 10^{-13}$) Nm s rad⁻¹. The results of the three-parameter model using the experimentally determined data of angular velocity $\dot{\theta}$ and torque rate \dot{T} are plotted in figure 5.11. The three parameter model correctly captures the physical behaviour of the hair over the entire range of angular velocities including the drop of torque T for the small velocities, with an average absolute percent difference of 7 %, the largest difference being 16 % at the smallest angular velocity.

5.4 Discussion

5.4.1 Comparison with fluid mechanic modeling studies

The preliminary statically determined values of S as well as the two-parameter model values of S_{2p} and R_{2p} for the biologically most relevant angular velocities $\dot{\theta}$ larger than 0.05 rad s⁻¹ found in the present study, agree within one order of magnitude with the values obtained in earlier studies using a physical-mathematical flow modelling approach.^{156,159,160} Similarly, the three-parameter model values of the two spring elements S_{3p} and S'_{3p} are quite comparable to previously determined values but, in contrast, the value of the damping element R_{3p} is approximately 100 times larger than R_{2p} . Because the three-parameter model correctly captures the qualitative variation of hair motion over the range of angular velocities and torque rates explored, it is deemed to be

the more fundamental of the two hair suspension viscoelastic models. Notwithstanding, for angular velocities larger than 0.05 rad s^{-1} typical of many biologically relevant investigations, the two-parameter model yields very good predictions of hair behaviour.^{156,159,160,182,183}

A previous publication reported that by applying the two-parameter model a constant value for S (corresponding to S_{2p}) and R (corresponding to R_{2p}) was obtained for a $750 \mu\text{m}$ long trichobothrium on the metatarsus (MeD1) of *Cupiennius salei* and found these to be $5.77 \times 10^{-12} \text{ Nm rad}^{-1}$ and $2.20 \times 10^{-15} \text{ Nm s rad}^{-1}$, respectively, in the case of a sinusoidally oscillating flow with a velocity amplitude of 50 mms^{-1} driving the hair.¹⁵⁷ The experimental fits for *Cupiennius* hairs provided in a previous publication yield the constant values $S = 1.32 \times 10^{-11} \text{ Nm rad}^{-1}$ and $R = 3.34 \times 10^{-15} \text{ Nm s rad}^{-1}$ for a $950 \mu\text{m}$ long hair on the tibia (TiDA1).¹⁶² Our present results are also in good agreement with the constant S values of ca. $10^{-11} \text{ Nm rad}^{-1}$ reported in a previous publication for 1 mm long cricket filiform hairs for the case of quasistatic loading experiments.¹⁸⁴ The filiform hairs on the cerci of crickets are similar to the spider trichobothria in regard to diameter and length, and they are sensitive to similar air flow velocities.^{182,185,186} It should be noted that the flow conditions corresponding to the deflection of the above mentioned MeD1 and TiDA1 spider trichobothria are associated with maximum angular velocities significantly larger than 1 rad s^{-1} . In this regard, the results of Humphrey & Barth show that the angular velocities of MeD1 hairs $250 - 1000 \mu\text{m}$ long greatly exceed 1 rad s^{-1} in oscillating air flows with frequencies larger than 10 Hz and constant velocity amplitude of 10 mm s^{-1} .¹⁵⁶ The same is true for MeD1 hairs $500 \mu\text{m}$ long in oscillating air flows with frequencies larger than 50 Hz and constant velocity amplitude of 2 mm s^{-1} .¹⁵⁶

Angular deflection velocities of trichobothria exposed to natural air flows eliciting prey capture behaviour of the spider like in the wake of a buzzing fly are frequently larger than 1 rad s^{-1} (figure 5.12).¹²⁹

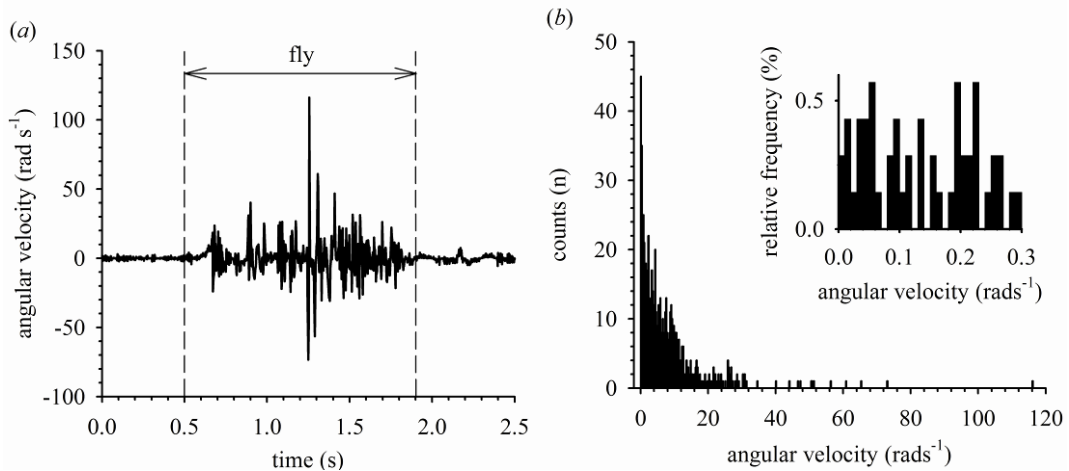


Figure 5.12: Hair Response to Natural Stimuli. Angular velocity of a trichobothrium hit by the wake cone of a fly buzzing stationarily at a distance of 4 cm from the trichobothrium and at an angle of 45 degree to the long axis of the spider leg. (a) Time course of the angular velocity measured from high-speed video recordings (sampling rate 500 frames per second). (b) Distribution of the angular velocity values from (a) between 0.5 and 1.9 s, bin size 0.25 rad s^{-1} , $n=700$. Negative velocity values from (a) were accounted for as positive. Inset: Relative frequencies of angular velocity values in the range from 0 to 0.3 rad s^{-1} ; bin size 0.01 rad s^{-1} .

5.4.2 Modeling of the viscoelastic hair suspension

All models for linear viscoelastic materials are composed of linear springs and linear viscous dashpots to describe the stress-strain-time relations of such materials.^{177,178,187} The form of equation 5.1, describing filiform hairs as forced damped harmonic oscillators, tacitly assumes that the viscoelastic behaviour of the hair suspension material can be approximated as a Kelvin solid; that is, according to a linear viscoelastic model consisting of a spring element (S_{2p}) and a dashpot element (R_{2p}) in

parallel. Thus, in equation 5.1 the torque, T_m , characterizing the material's inherent resistance to motion is given by:

$$T_m = R_{2p} \dot{\theta} + S_{2p} \theta \quad (\text{Equation 5.5})$$

where R_{2p} and S_{2p} are constants.^{177,178,187} The response of this model to a suddenly imposed external torque is for the torque to be initially carried entirely by the viscous element, R_{2p} thus preventing any immediate deflection of the hair. However, as the viscous element elongates it transfers an increasing portion of the applied torque to the elastic element S_{2p} , so that, finally, the entire torque is carried by the elastic element S_{2p} . Such behaviour is referred to as delayed elasticity.¹⁸⁷

By resorting to a three-parameter viscoelastic solid as described by equation 5.3, deformation can occur for any rate of applied torque. Whereas the two-parameter model would resist a deformation for a suddenly applied torque, the three-parameter model results in an initial deformation of the hair suspension by the two spring elements, S_{3p} and S'_{3p} , acting in parallel. Therefore, to achieve a particular angular deformation as the rate of deformation increases, the torque required to reach that angular deformation should asymptotically approach a constant value as observed in the experimental data. The two-parameter model achieves a similar effect by incorporating a numerical value for the dashpot that is three orders of magnitude smaller than the numerical value for the spring. The similar magnitudes of the three-parameter model constants allow the model to capture the deformation at low angular velocities.

These findings suggest that the viscoelastic nature of the hair suspension material and structure is complex at low angular velocities, with reversible elastic deformation and irreversible dissipation of mechanical energy strongly depending on both the deformation

and the rate of deformation of the material. The mechanical behaviour of the hair can be associated with the time-dependent shearing properties of materials consisting of physical networks of molecules like the protein matrix in arthropod cuticle.^{Error! Bookmark not defined.,188}

Not surprisingly, the work required to deflect the hairs to their physiological threshold angle of 0.01 deg at constant velocities essentially follows the changes of the torque T (figures 5.9b, 5.10a).¹⁸¹ The asymptotic, large angular velocity value for this work is about 2×10^{-18} J, close to the value of the area under the hair deflection versus load curve in figure 5.8b for 0.259 rads^{-1} . When allowance is made for the fact that this load curve corresponds to the first half of a saw tooth wave, it is possible to compare with the work generated by a sinusoidally oscillating hair of similar characteristics.¹⁶² For such a wave, the absolute value of work generated during each quarter of the sinusoidal oscillation is a number ranging between 4×10^{-18} and 1×10^{-17} J, approximately. The correspondence between these values and the asymptotic one of the present study is acceptable, especially when allowance is made for the fact that neither the angular velocity nor the acceleration are constant for sinusoidally oscillating hairs. Note that if instead of integrating a quarter of a sinusoidal cycle the integration is carried out for a full cycle, the net work obtained is smaller (10^{-20} to 10^{-19} J), because of the energy returned by the oscillating hair.¹⁶²

5.4.3 Sources of hair suspension viscoelasticity

The structures responsible for the viscoelastic behaviour of the hair suspension are the following (figure 5.3).¹⁵⁶

(i) The membrane, which connects the hair shaft and the exoskeleton, is suggested to represent the main spring element consisting of a highly elastic material. Its increase in stiffness may result from viscoelastic effects such as already shown for a soft cuticular pad of *Cupiennius* which functions as a high-pass filter in the spider substrate vibration receptor.¹⁶⁷ It seems likely that the hair suspension membrane contains resilin, which is known to elastically store energy with high efficiency in the joints of insects. According to dynamic mechanical testing between 10 and 200 Hz, the elastic modulus of resilin increases with increasing frequency as does the torque T resisting the hair deflection in the present study.¹⁸⁹

(ii) Regarding the dashpot element, we suggest two possible sources for the damping properties of the hair suspension. (a) The lever arm of the hair shaft below the suspension membrane, and the structure coupling the outer dendritic segments of the sensory cells to it, are surrounded by receptor lymph.^{129,190} The displacement of receptor lymph in such a confined space can be expected to be highly viscous and the associated energy dissipation will work to dampen the hair deflection. (b) The region of the coupling structure contacting the dendrites may add to this initial low velocity damping, but no experimental data are available yet.

5.4.4 Biological relevance

The velocities of background flows during the activity period of the spider in its natural habitat are typically smaller than 0.1 m s^{-1} , whereas the flow velocities generated by a buzzing fly can reach values of up to 1 m s^{-1} .¹⁹¹ The even more important difference between flow signals generated by prey insects or predators and the background wind is

the flow velocity time history. The signals generated by prey or predators are of a fluctuating nature, characterized by relatively large ranges in the spatial and temporal scales of motion. In contrast, the background wind, in particular during the night time activity of *Cupiennius*, is characterized by a much more steady flow.^{191,192} Angular deflection velocities of trichobothria caused by natural stimuli such as the background wind or the highly turbulent wake of a fly span a broad range of values with peak velocities of up to 150 rad s^{-1} (figure 5.12a). Interestingly, only 1.7 % of the angular velocity values are less than 0.05 rad s^{-1} (figure 5.12b), falling in the range of the deviation from the Kelvin solid-like behaviour of the suspension material.

At high angular velocities the viscous dashpot element characterized by R_{3p} in the three-parameter model resists deformation, and as a consequence, the two spring elements S_{3p} and S'_{3p} dictate hair motion (figure 5.4b). This results in torque being directly proportional to the hair's angular deflection. In contrast, at low angular velocities the dashpot element can deform, thus relaxing the material and resulting in a lower torque to attain the same angular deflection. This viscoelastic material behaviour at low angular velocities facilitates the start of hair motion from rest, thereby contributing to the highly phasic properties of the nervous response of the trichobothria.^{129,181} Note that under biologically relevant stimulus conditions a trichobothrium generally moves at high angular velocities for which the spring elements dominate hair motion. Highly fluctuating signals such as those produced by potential prey animals result in frequent and sudden changes of the hair's angular velocity. Indeed, directly at the start of a motion with large constant velocity the action potential discharge rate of the hair sensory cells is larger than during ongoing deflection.¹⁸¹ The mechanical properties of the hair suspension seem to

specifically support the oscillating nature of the deflections of a trichobothrium caused by biologically relevant stimulus patterns.

In addition to the hair suspension structures, the viscoelastic properties of the dendrites themselves may help to explain the phasic response pattern of the sensory cells of the trichobothria, which readily respond to movement, but not to static deflection.¹⁸¹

It is quite possible that only during movement of the coupling structure, not however during static deflection, the strain exerted on the sensory cell membrane is large enough to open a supra-threshold number of ion channels leading to the generation of the nervous response.

5.4.5 Relevance to Bio-inspired Materials Approaches to Sensing

Although the origin of the frequency dependant energy absorption remains for the trichobothria, the implications are still important and there are still important lessons offered to functional material scientists. As discussed in the last chapter, viscoelastic materials are used for high-pass filtering roles in biological mechanical signal transduction. This study highlights the fact that viscoelastic materials can be used in several different functional roles regarding signal absorption and filtering.

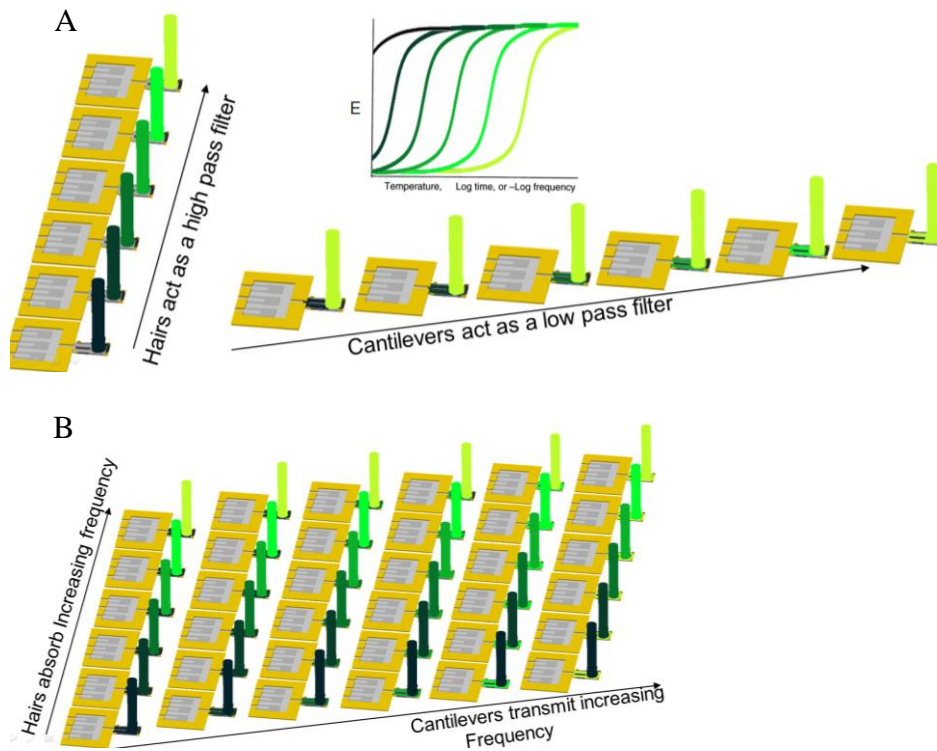


Figure 5.13: Relevance to Sensor Engineering A) A schematic showing the difference in filtering depending on the location of a material that has a T_g near room temperature. B) An array of sensors with varying band-pass frequencies

If a viscoelastic material is used to transmit mechanical information, then it can be used to as a high-pass filter. This is analogous to using the time dependant material as the hair shown in figure 5.13. These time-dependant polymers can also be used as low pass filters by using the material at the site of mechanical transduction. A softening of this material would result in a softer strain-based, which would deform more in response to stress. This is analogous to using the time dependant material as the cantilever shown in figure 5.13. This could also be accomplished by using the material as a support structure, which would divert mechanical energy from the transmission line (not shown), such as the hair supporting membrane. Furthermore, these components can be combined to create sensor that are specifically sensitive to very particular stimuli.

5.5 Conclusion

In conclusion, this work involved examining the stiffness of wind-based receptors to probe the validity of fluid dynamics models and to probe the origin of high-pass response of previous nervous response measurements. The stiffness measurements did show time-dependant properties. The mechanical data was fit to an appropriate 3-parameter model. Due to the complex structure of the hair receptors the exact origin of the time-dependant properties could not be conclusively determined. Although, it is likely that the nerve data is correlated to the mechanical behaviour, nonetheless the unexpected fruit really came from trying to interpret the biological data. Specifically, from this data it became apparent that passive polymers with T_g 's near room temperature can be used to sort mechanical data in a fairly complex way.

CHAPTER 6

BIO-INSPIRED MATERIAL FOR FLOW SENSING

6.1 Introduction

Organisms interpret their surroundings from information obtained with a variety of sensory systems. Mechanical-based receptors is an important class of receptors, such as shaft-like deflection of stiff hairs for vibration detection in spiders,¹⁹³ flexible membrane-like structures for night vision in snakes,¹⁹⁴ long whiskers for wake tracking in seals,¹⁹⁵ and superficial neuromasts (hairs) for navigation in fish.¹⁹⁶ In contrast, active sonar systems are widely used for a variety of civil and military applications in underwater environment. However, passive sensor systems similar to the fish lateral line provide a huge advantage in “silent” observation of the environment, which does not reveal the source and does not interfere with moving vehicles and various life forms.¹⁹⁷

In this work, a bio-inspired material-based approach is used to enhance microfabricated flow sensors, which were originally inspired by superficial neuromasts, much like that of a blind cave fish *Astyanax fasciatus mexicanus*. Blind cave fish have adapted to have superior abilities to navigate blindly in a hydrodynamically complex underwater environment (figure 1a- c).^{198,199} The glycoprotein cupulae couples the arrays of hair receptors to the surrounding fluidic environment (figure 1b-c). Therefore, this work proposes a new strategy towards enhancing microfabricated flow sensors, namely the hydrogel encapsulation

of the sensor.²⁰⁰ This design strategy comes from o observation that the cupula appears to be a specialized structure for fish flow transduction. In order to properly implement this strategic design we will study the mechanical properties of the fish cupula, acting on the assumption that biology has tailored the intrinsic properties of the cupula hydrogel for enhanced drag and flow signal absorption.

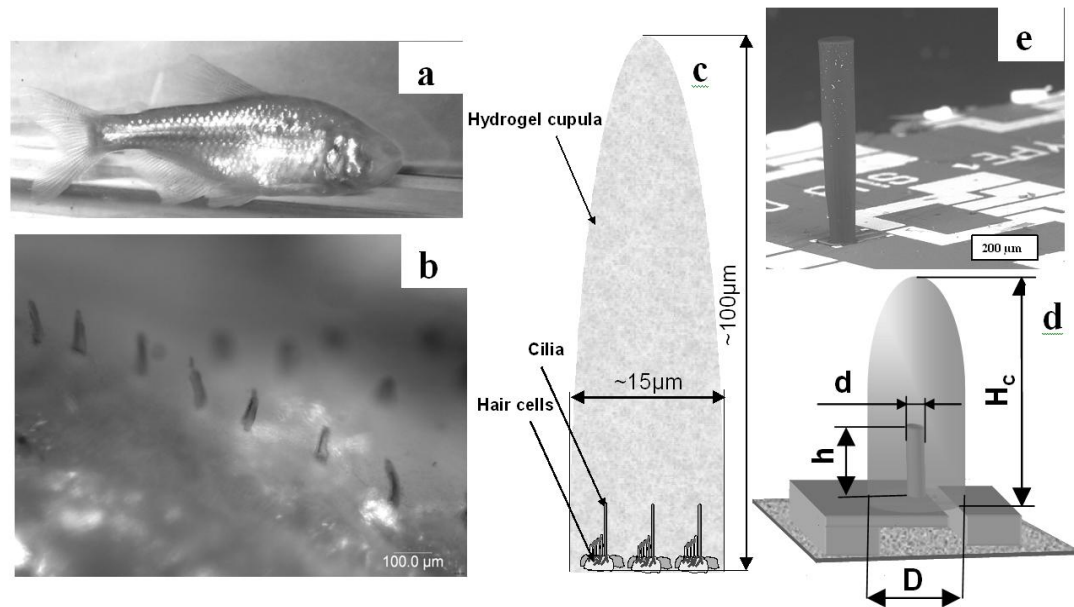


Figure 6.1 The Fish Lateral-line, Neuromasts, and Bio-inspired Sensors. **a)** Photograph of adult Blind Cave fish. **b)** Micrograph of the several cupula (blue cylinders) of the superficial neuromast row arrays (stained with Methylene Blue). **c)** General schematics of structure of superficial neuromast of the fish. **d)** General schematics and geometrical dimensions of the MEMS flow sensor capped with hydrogel cupula. **e)** SEM of photograph of a flow sensor with naked hair²⁰¹

The combination of the sensor with a hydrogel cupula grown by wet-chemistry micropatterned photo-polymerization presented here creates an integrated hair-cupula sensor with superior flow detection (figure 1d). We suggest that this symbiotic technology may enable the self-navigating ability of autonomous underwater vehicles, as well as possibly providing insight to biologists regarding the effects of the cupula.

6.2 Materials and Methods

6.2.1 Fish Preparation and Care

Blind cave fish (*Astyanax fasciatus mexicanus*) were cared for and kept at Iowa State University using procedures accepted under the Animal Care protocol (#9-05-5972-I)198 that was approved by Committee on Animal Care (COAC, Iowa State University). Experiments were performed on fish that were immobilized by ice water or buffered 0.005 % MS222 solution and placed into a holder with aquarium water. Optical microscopy studies were performed with stained superficial cupulae were studied in bright field and a bright field using a Leica DM4000 microscope.

For force-spectroscopy studies, a hole was made in upper part of disposable plastic Petri dish to fit AFM head equipped with fluid cell. Bottom part was equipped with four spring clamps to hold fish during mechanical measurements. Quick staining by one drop of 0.1% aqueous Methylene Blue or Janus Green allowed facile locating of cupulae. Excess of the dye was washed away after exposure of several second. After euthanizing the fish with MS222 and staining by Janus Green small piece of fish cheek was cut and placed in holder with water under AFM. The choice of the cheek was predominated due to high concentration of the superficial neuromast cupula and hard material of cheek itself that served as a solid substrate for measurements. Several cupula that were laying down were chosen for the mechanical testing. Force-volume measurements were performed at varying points along the length of the cupula to ensure nonexistence of the cupula shaft bending.

6.2.2 Force-Spectroscopy

AFM (Dimension 3000, Veeco Metrology) was used for imaging and mechanical measurements in water according to the procedures presented in Chapter 3. AFM tips were purchased from NovaScan Technologies, V-shaped, contact tips with nominal spring constant about 0.01 N/m. Spring constants of cantilevers were determined from the resonant frequencies and the spring-on-spring method. We used very soft contact tips equipped with borosilicate glass sphere (10 μ m in diameter) in the fluid measurements in order to get suitable data of the soft surfaces at room temperature.

6.2.3 Artificial Cupula Preparation

Poly(ethylene glycol) tetraacrylate (PEG-TA, Mw=18 000, Polyscience, Inc) was dissolved in methanol (wt 20%). Photoinitiator 2,2-dimethoxy-2-phenylacetophenone (DMPA, Aldrich) was dissolved in 1-vinyl-2-pyrrolidone (600 mg in 1 ml). 10 μ L of initiator solution was added to 1 ml of polymer solution. The hydrogel layer was developed by placing a sensor device in DI water for 2-3 hours. Artificial cupula were grown on the sensors by dropping 3-5 drops of UV cross-linkable PEG solution in methanol onto the silicon chip containing the sensor. Each drop was allowed to dry before the next was added. The sensors were then placed in a holder fabricated out of glass slides to suspend the photomask (opening 150 μ m and 500 μ m in diameter) just slightly above the SU-8 hair. The mask was then aligned under a stereomicroscope; followed UV irradiation of the entire system by UV light (365nm). The sensor was irradiated 6 min at intensity about 20 mW/cm². After irradiation, the sensors were placed in a Petri dish of Nanopure water for 2 hours completely undisturbed.

6.3 Results and Discussion

6.3.1 Fish Cupula Material Study

The purpose of this study was to guide development of a novel approach to improve the performance of microfabricated flow hair sensors introduced by Liu group (figure 6.1e). Therefore, we set out to create specialized structures, cupulae, to efficiently transmit flow energy to the sensors. In order to guide the development of an artificial cupula, the mechanical properties of superficial cupula in blind cave fish were characterized.

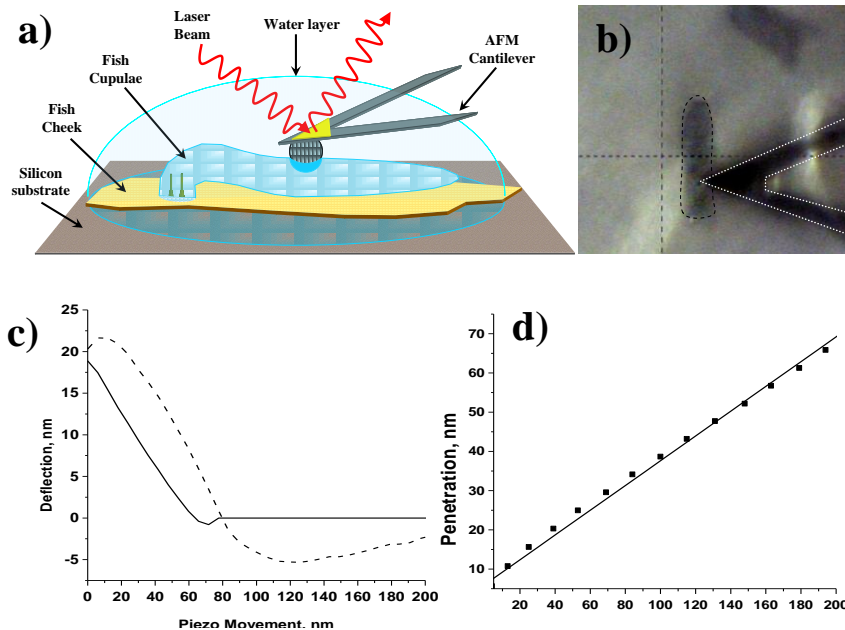


Figure 6.2: Fish Cupula Material Testing. A) Schematic of setup for cupula material properties measurements B) A screen shot of the cantilever pressing on a stained cupula C) A typical force distance curve from fish cupula D) An example load-penetration curve.²⁰¹

To this end, the mechanical properties of blind cave fish cupula were directly measured using fluid-based surface force spectroscopy with a colloidal probe. The

elastic modulus of the fish cupula was measured in water using an atomic force microscope (AFM) operated in force-volume mode in accordance with usual approach developed in our group (figure 6.2a).^{202,203,204} Figure 6.2D shows an example load-penetration curve indicating the magnitude of forces applied. The loading plot in coordinated penetration^{3/2} versus the applied load (Hertzian coordinate plot) was observed to be highly non-linear (figure 6.4). For purely elastic solids it is expected to be linear. The non-linear response is generally caused by viscoelasticity of the materials associated with time-dependent, viscous response.^{205,206}

It should be mentioned that the maximum applied load is extremely low, on the order to 250 pN, which is significantly less than the force to break a single C-C bond (on the order of several nN) and therefore, any non-linearity of the Hertzian coordinate plot is not due to plastic deformation. The Voigt viscoelastic model was combined with the Hertzian contact model to fit the non-linear loading data for the cupula. The bio-hydrogel was measured to have an elastic modulus of 9 kPa and a relaxation time of 0.42 seconds, characteristics of compliant and viscous materials.²⁰¹

6.3.2 Fish Inspired Artificial Cupula

6.3.2.1 Development of Artificial Cupula Material

The synthetic cupulae with comparable mechanical properties were fabricated by photo-crosslinking tetra-acrylate functionalized poly-ethylene oxide glycols (PEG) (figure 6.3, top). Photomasks were used to localize the crosslinking. UV-photopolymerization was applied through a proper photomask to initiate localized crosslinking reaction in a dry state and form a three-dimensional network (figure 6.3, bottom). Different molecular compositions

were tested with the final selection of PEG segments with the average molecular weight between functional crosslinking groups being about 9,000.²⁰⁷

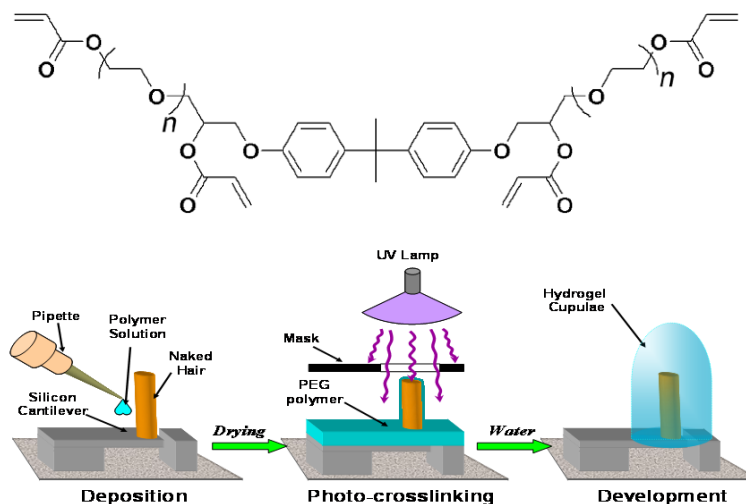


Figure 6.3: Artificial Cupula Fabrication. Top: A schematic of the photo-crosslinkable acrylate-functionalized PEO molecule used to fabricate the artificial cupula. Bottom: A schematic diagram of the fabrication process leading to dome-like cupulae.²⁰¹

Rinsing the photopatterned layer with water removed the residual uncross-linked monomer and initiates swelling the cross-linked PEG layer around the hair. Swollen PEG completely covered the polymeric hair adapting a dome-like shape (figure 6.5A). Independent estimation revealed the swelling ratio of about 1000% indicating a water content of about 90%.²⁰⁷ Varying the degree of crosslinking and initial monomer deposition conditions allowed us to tune the dimensions of the dome-shaped hydrogel cupula. As a result of crosslinking, the hydrogel cupula is anchored to the parylene coating that covers the polymer hair and silicon cantilever. This attachment is strong enough to sustain high flow pressure at maximum flow rates tested here (350 mm/sec). The cupula, which was placed directly on the hair into the sensory device (figure 6.5A), sustained its dome-like shape in the wet state at ambient conditions facilitating the transfer of the whole sensory system into the

water tank for further underwater testing. Under certain conditions, the hydrogel cupula can be mechanically pulled off from the hair.

6.3.2.2 Artificial Cupula Material Study

Having developed a controllable hydrogel material with patterning capabilities and likely enhanced anti-biofouling properties, we then measured the material properties to compare with the biological analogue. The mechanical properties of the hydrogel were tested with force-spectroscopy using the stand procedure.

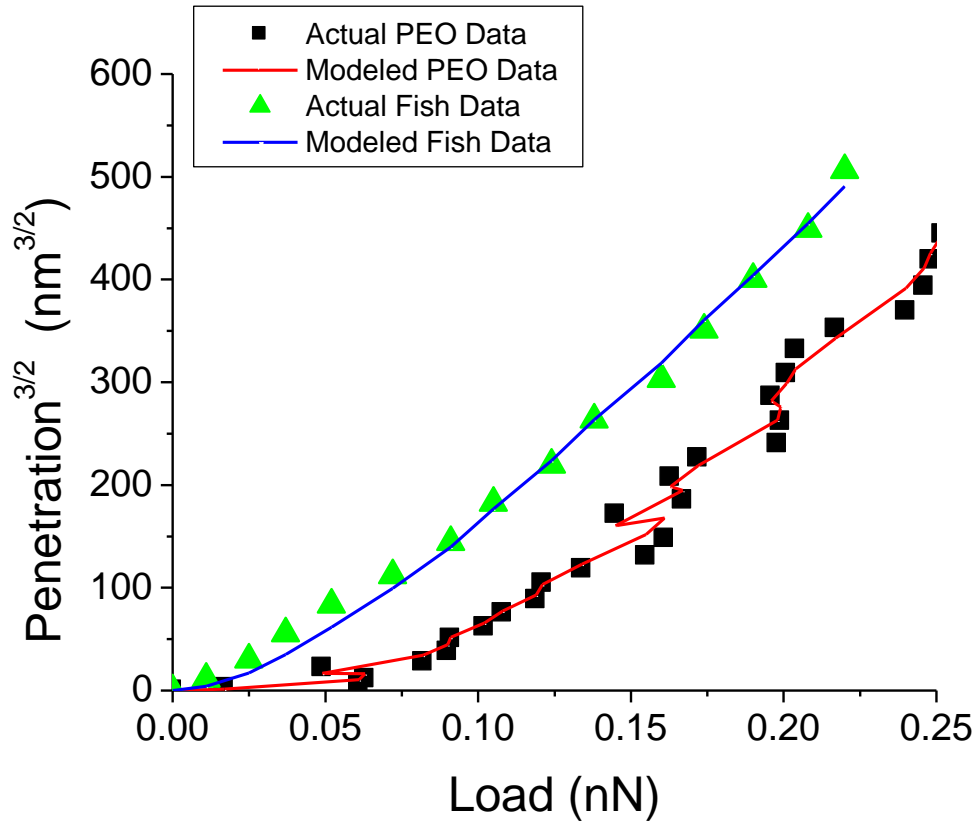


Figure 6.4: Comparison of Load-Penetration^{3/2} of Fish Cupula and Artificial Cupula. A Hertzian coordinates plot, load-penetration^{3/2} curve comparing the mechanical response of the fish cupula to the PEO-based cupula. Non-viscoelastic material would be linear²⁰¹

The Voight viscoelastic model combined with the Hertzian contact model was used to fit the non-linear experimental loading data obtained with colloidal probe spectroscopy on top of

synthetic cupula. This approach applied to synthetic cupula with intermediate molecular weight between cross-links resulted in an elastic modulus of 9.5 kPa and a relaxation time of 0.50 seconds, fairly close to that obtained for biological cupulae.²⁰¹ Therefore, this artificial material matched the material properties of the fish cupula quite well (Figure 6.4). After a promising material with similar properties to the biological analogue was fabricated, then testing moved to gauging the effectiveness of this bio-inspired approach.

6.3.2.3 Sensing Performance of Artificial Cupula

After trying different designs, for underwater testing we selected the dimensions of 0.5-1 mm in height and 1-2 mm in diameter for the hydrogel cupula in the wet state and the dimensions of 600-700 μm in height and 80 μm in diameter for the polymer hair (figure 6.5A). The bio-inspired approach was quantified by testing the hair sensors before and after the hydrogel had been applied to the hair sensors. The flow sensor testing was carried out under water by shaking dipole placed at set distances from the sensor surface (figure 6.5B). The dipole amplitude and frequency was controlled and monitored, while simultaneously monitoring the Fourier transform of the sensor piezoresistive output. This standard dipole test allows for prediction of the water velocity ($v \sim 1/r^3$) at the sensor surface based on the frequency of the dipole, the amplitude of the dipole, and the dipole-sensor distance. The dipole amplitude was varied to obtain the sensitivity and minimum threshold stimuli were measured by lowering the dipole amplitude until the sensor output became erratic. A second test involved constant (DC) laminar flow over the sensors in a flow chamber. In this test the flow velocity was varied controllably and the sensor piezoresistive output was simultaneously monitored.

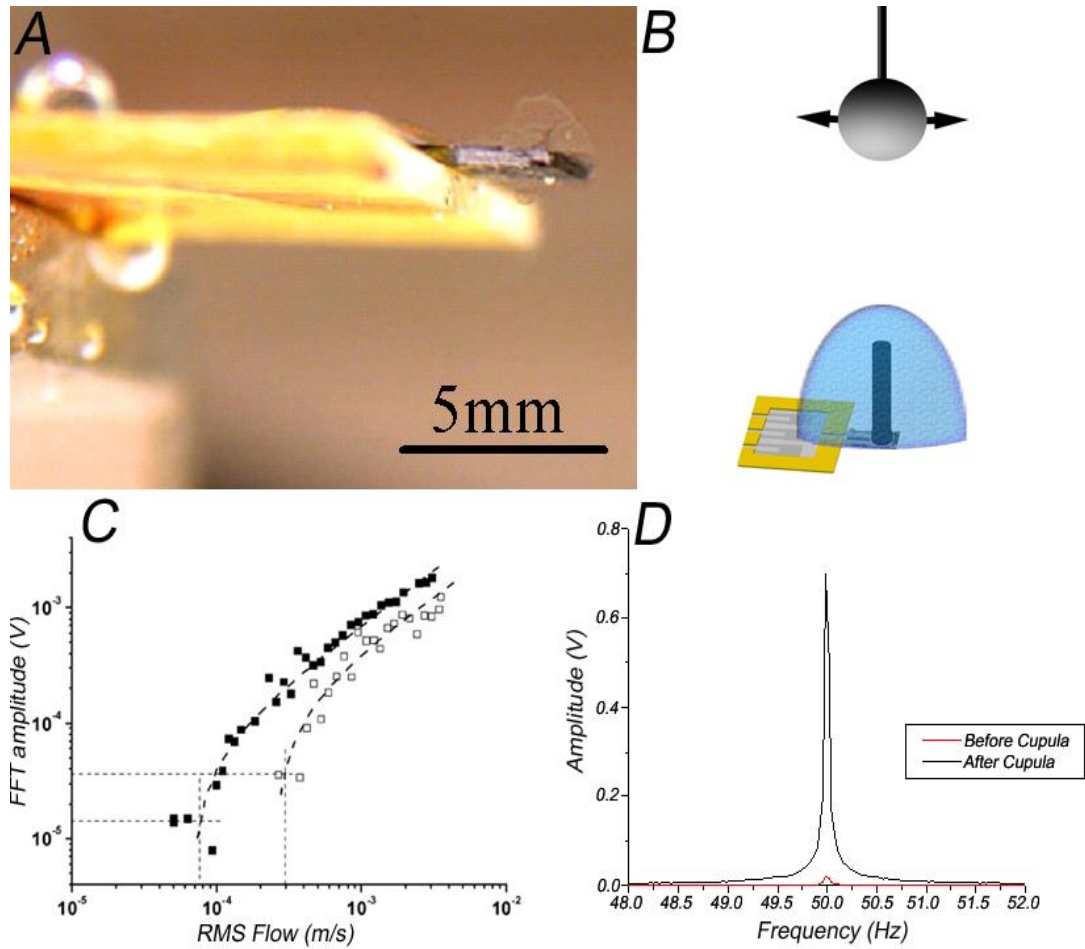


Figure 6.5: The Performance of The Dome-shape Cupula. A) Optical image of a sensor encapsulated in a dome-shaped cupula B) Schematic of AC test setup C) Response vs. Frequency at 50 Hz excitation frequency before sensor modification and after sensor modification D) Signal Response vs. velocity at 50 Hz (open before cupula, solid after cupula modification).²⁰¹

After the measurements were performed on the initial sensor with a bare hair, then the sensor was encapsulated in a dome-shaped cupula and tested under identical flow conditions. The unaltered sensors tested here had minimum water velocity detection thresholds of around 0.2 mm/s, and after the synthetic cupula was applied to the sensors the threshold velocities improved by over 2.5 times to roughly 0.075 mm/s (Figure 6.5C). In the linear regime of the sensor output the sensitivity increased by 60%, going from 4.3 mV/(mm/s) to 6.8 mV/(mm/s). Surprisingly, the application of the cupula resulted in

sensors with a lower noise floor from about 35 μV to about 10 μV and dynamic range increased by half an order of magnitude. This result indicates that the inertia-based dome-shaped cupula might also have a signal filtering role with random noise to be suppressed by viscously-coupled cupula. The sensitivity improvement led to very significant sensor output enhancement at relatively higher RMS flow rates (Figure 6.8C & D). The DC measurements resulted in a four times improvement in both the sensitivity and minimum threshold stimulus as discussed in chapter 5.²⁰¹

The impressive improvement of the flow velocity detection after the encapsulation of the hair sensor into the hydrogel cupula observed here is likely due to increased drag forces due to the larger effective cross-sectional area of the capped hair sensor, but simple estimates may imply that this is not enough to completely account for this improvement. The drag force, F , for a prolate-shaped body at low Reynolds number is given by

$$F = C * \mu * L * U \quad (\text{Equation 6.1})$$

where C is a constant, μ is the fluid dynamic viscosity, L is a characteristic length scale, and U is the approaching flow velocity.²⁰⁸ The ratio of the drag force acting on the impermeable cupula to the drag force that would act on the naked hair can be derived from simple scaling considerations using prolate shape approximation:

$$\frac{F_{cup}}{F_{hair}} \approx \left(\frac{H_c}{h_h} \right)^{4/3} \left(\frac{D_c}{d_h} \right)^{2/3} \quad (\text{Equation 6.2})$$

with the geometrical length scales as defined in Fig. 1d, where H_c is the cupula height, D_c is the cupula diameter, h_h is the original hair height, and d_h is the original hair diameter. This simple relationship shows that for typical cupula dimensions ($H_c/h_h \sim 1.5-3$ and $D_c/d_h \sim 20-30$), the expected increase in the drag force can be $F_{cup}/F_{hair} \sim 10-30$. These values are fairly

close, but lower than the values observed in this study ($F_{\text{cup}}/F_{\text{hair}} \sim 30-70$), especially at lower flow velocities, indicating the presence of additional factors that can be related to the semi-permeable nature of the hydrogel materials with low crosslinking density. A logical contribution is a coupling interaction between fluidic flow and fluid trapped inside the loose semi-permeable polymer network.²⁰⁹ Nonetheless, it should be stated that this prolate analysis involves large simplifications of the actual conditions of the experimental tests and thus should not be considered as strong evidence for particular sources of enhanced drag.

On the other hand, it is reasonable to expect that the viscous behavior of a cupula, which is composed of 90% water confined within a loose PEG network, should modify the pressure transfer from the water environment to the hair due to the contribution of a friction component of the fluid entrapped in the flexible polymer network.²¹⁰ For a hydrogel with average segment $M_n = 9000$, the average spacing between cross-links is close to 8 nm in the bulk state and will increase to about 18 nm in the wet state, as can be estimated assuming random-coil conformation of polymer segments.²⁰⁹ Thus, the effective width of the channels for water flow should be close to 15 nm. Considering that 3 to 8 molecular layers of water in contact with polymer chains should be virtually immobilized,²¹¹ a significant fraction (up to 30%) of water molecules should be confined by the polymer network, thus dramatically increasing drag forces. Moreover, the very slow hydrogel relaxation (the relaxation time is about 500 ms as estimated from dynamic colloidal probe microscopy measurements), should damp some of the low frequency noise.²¹² We expect that such a material would work to decrease the lowest detection threshold and increase the maximum limits of flow detection. The latter has likely occurred, as evident from viscous damping of the irregular, noisy background observed in our experiments (Fig. 3d).

6.4 Conclusion

In conclusion, we have demonstrated that the bioinspired concept of encapsulating MEMS haircell flow sensors with semi-permeable, hydrogel cupulae, as employed by fish for underwater orientation, works very efficiently. The significant improvement of all of the characteristics of the hair flow sensor has been achieved after encapsulation with a hydrogel cupula. Applying the cupula-hair design, we have demonstrated significant decrease in the lower threshold limit of flow detection and the expansion of the dynamic range due to an efficient suppression of background noise within the viscous-damped cupula with the damping ability increasing for the low frequency noise due to the viscous shear strength characteristics of hydrogel networks.²¹³ Moreover, the enhanced protection afforded by the hydrogel encapsulated hair flow sensors should enhance their ability to withstand high elastic deformation due to impact as well as provide anticorrosive and anti-biofouling properties to better withstand the marine environment.^{214,215}

CHAPTER 7

BIO-INSPIRED STRUCTURE FOR FLOW SENSING

7.1 Introduction

The hair cells of vertebrates are particularly interesting from a bio-inspired design standpoint due to their amazing sensitivity (displacement sensitivity in the nm range) and their functional versatility. For example, hair cells in the lateral line system of fish are capable of detecting water flows past the body surface with velocity of few micron per second.^{216,217} This functional versatility is made possible by the variety of specialized auxiliary structures that mechanically link sound, body motions or surrounding flows to the ciliary bundles of the hair cells. Such structures include membranes, bones, otolithic masses (calcareous stones), fluid-filled canals, and gelatinous structures known as cupulae. Fish have been shown to use the flow sensing hair cells of their lateral line for a variety of important functions, including prey localization, predator avoidance, schooling and many other functions.²¹⁸ As such, the lateral line system serves as a bio-inspiration for the engineered development of flow-sensing abilities in autonomous underwater vehicles, including the ability to detect hydrodynamic disturbances created by moving bodies and stationary bodies in a flow field, to maneuver effectively in complex turbulent flow conditions and minimize drag and increase locomotion efficiency.²¹⁹

In this regard, the blind cave fish, *Astyanax fasciatus* provides an ideal model system for inspiring engineered flow sensors, because these fish have evolved under dark

conditions that favored the development and reliance on flow sensing receptors (figure 7.1a-c). Because their eyes have degenerated, these fish form hydrodynamic rather than visual images of their surrounding environment. As they glide past stationary objects, they can detect the obstacle-created distortions in their own self-generated flow field. The hydrodynamic imaging abilities of blind cavefish allow them to avoid collisions with nearby obstacles²²⁰ and to make fine spatial discriminations on the order of 1 – 2 mm.²²¹

As discussed in detail in the first chapter of this dissertation, the lateral line system of blind cavefish, as well as other species, consists of many, spatially-distributed flow sensors, called neuromasts (figure 7.1b). Neuromasts can be divided into two basic categories – those directly on the skin surface (superficial neuromasts) and those in fluid-filled canals just under the skin surface. Blind cavefish have several anatomical specializations of the lateral line system, which include superficial neuromasts with greater cross-sectional areas and taller cupulae. Although superficial neuromasts tend to be smaller (<100 μm in diameter) and have fewer hair cells (<50) than canal neuromasts, the two classes of receptors are similar in their basic anatomy, spatial distribution on the head and body and basic flow sensing function. Nevertheless, the work presented here is focused lower frequency sensitivity (<100Hz), which is the sensing range of superficial neuromasts which are specialized to respond in proportion to flow velocity in frequencies between DC-100Hz. The cupula of superficial neuromasts tend to have high aspect ratio, such that the distal end of the cupula is outside the boundary layer, exposed to the free stream region of the flow field, and bent (figure 7.1d).²²²

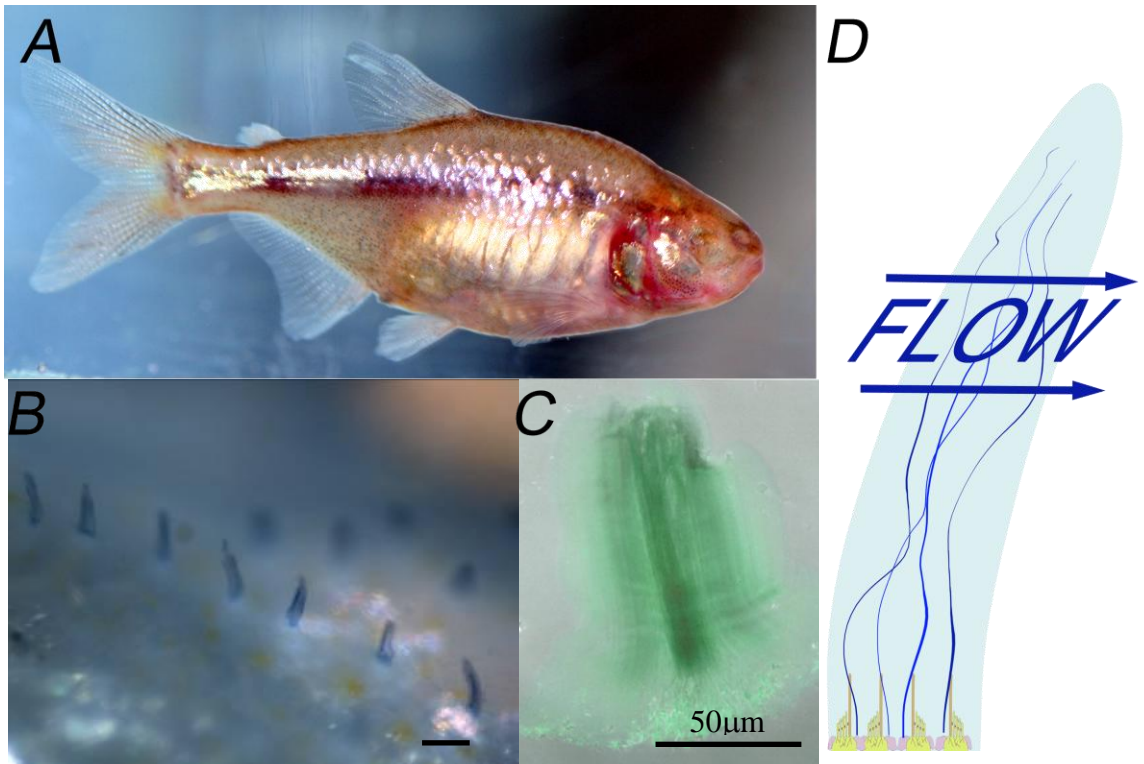


Figure 7.1: The High Aspect Ratio Superficial Cupula. (A) The blind cave fish evolved in darkness and relies on flow receptors for “imaging”, instead of eyesight. (B) An optical micrograph showing several stained cupulae (C) A confocal image of a cupula (scale bar) (D) Schematic of the neuromast structure that shows how the cupula couples the underlying hair receptors to the surrounding flow.

Here we report huge improvements to engineered flow hair sensors introduced recently coming from morphological lessons of superficial neuromasts.²²³ In order to maximize the coupling of water motions to the engineered flow sensor, the sensors have been covered with a tall hydrogel structure. Unlike our previous study,¹⁶⁸ in which a synthetic dome-shaped hydrogel with 10 kPa elastic modulus was developed to improve sensitivity, in this study we focus on mimicking of tall cupula-like structures with very low compliance (elastic modulus below 100 Pa) and high aspect ratio. Indeed, by creating higher-aspect ratio compliant structures capable of sensing beyond the boundary layer, we were able to impart sensing abilities to the flow sensors much higher than earlier rivaling that of fish.

Through the use of conventional drop-casting of the PEO solution presented in the last chapter, the resulted fabricated artificial cupula has dome-like shape. Having successfully mimicked the cupula hydrogel material,²²³ we set out to mimic the high aspect ratio cupula in superficial receptors to further improve the sensors' capabilities. A controlled drop-casting method was developed in order to fabricate artificial cupula with a shape like that of fish. The height and width of blind cave fish superficial cupula were studied with conventional optical microscopy and confocal fluorescence microscope to guide the high-aspect ratio synthetic cupula study.

7.2 Materials and Methods

7.2.1 Fish Cupula Aspect Ratio

Only superficial cupula with circular footprints were analyzed and studies were focused on the superficial neuromasts along the opercle. Confocal fluorescence microscopy was used for an initial detailed study of the morphology and dimensions of the cupula, whereas the optical microscopy was used to analyze the dimensions of many cupula and generate representative statistics. For imaging cupulae of blind cavefish superficial neuromasts, fish were first anesthetized in a 0.01% solution of MS222 and then dipped into a filtered 0.1% Janus green or methylene blue solution for 5 minutes to render cupulae visible under optical microscopy. The cupula involved in fluorescent confocal microscopy studies were further treated by removing them from the fish by suction with a small micropipette under the stereomicroscope. Cupulae were then placed in a 1 µg/ml solution of 5-DTAF, made from a 0.1% stock solution of 5-DTAF

dissolved in DMSO for epifluorescent visualization under a confocal microscope. Because cupulae are pH-sensitive, all solutions were made from filtered aquarium water buffered to the same pH (~7.5). as the original aquarium water after the anesthetic or stains were added. From these studies, we concluded that the superficial cupula had a height of $104 \pm 13 \mu\text{m}$, a width of $26 \pm 3 \mu\text{m}$, and an aspect ratio of 4.0 ± 0.8 ($n=13$, $N=1$) (see figure 7.1b,c).

7.2.2 Controlled Drop Casting for Hydrogel Shape Control

Synthetic high aspect ratio cupula were fabricated directly on hair flow sensors by dispensing a specific volume of hydrogel solution precisely onto the hair without wetting the sensor platform (for sensor description see Chapter 1). The poly (ethylene glycol) tetraacrylate (PEG-TA, $M_w = 18,000$, Polyscience, Inc) macromonomer solution was prepared according to conditions described Chapter 8. A syringe with solution attached to a 3-axis micro-positioning system equipped with a camera of the side view was aligned in the horizontal plane over the hair (figure 7.2a). Then while the syringe was several hundred μm over the hair, a droplet of less than $1 \mu\text{l}$ was dispensed from the syringe tip. While the droplet was still hanging from the syringe tip, the syringe was slowly lowered onto and through the hair using the z-axis micrometer. The syringe diameter is significantly larger than the hair diameter, so with careful alignment, the syringe did not interfere with the hair. After the droplet made contact with the hair, the droplet was furthered lowered over the length of the hair. The methanol in the droplet was allowed to partially evaporate for several seconds, until the droplet became slightly viscous and opaque, then the syringe was raised, leaving the droplet on the hair.

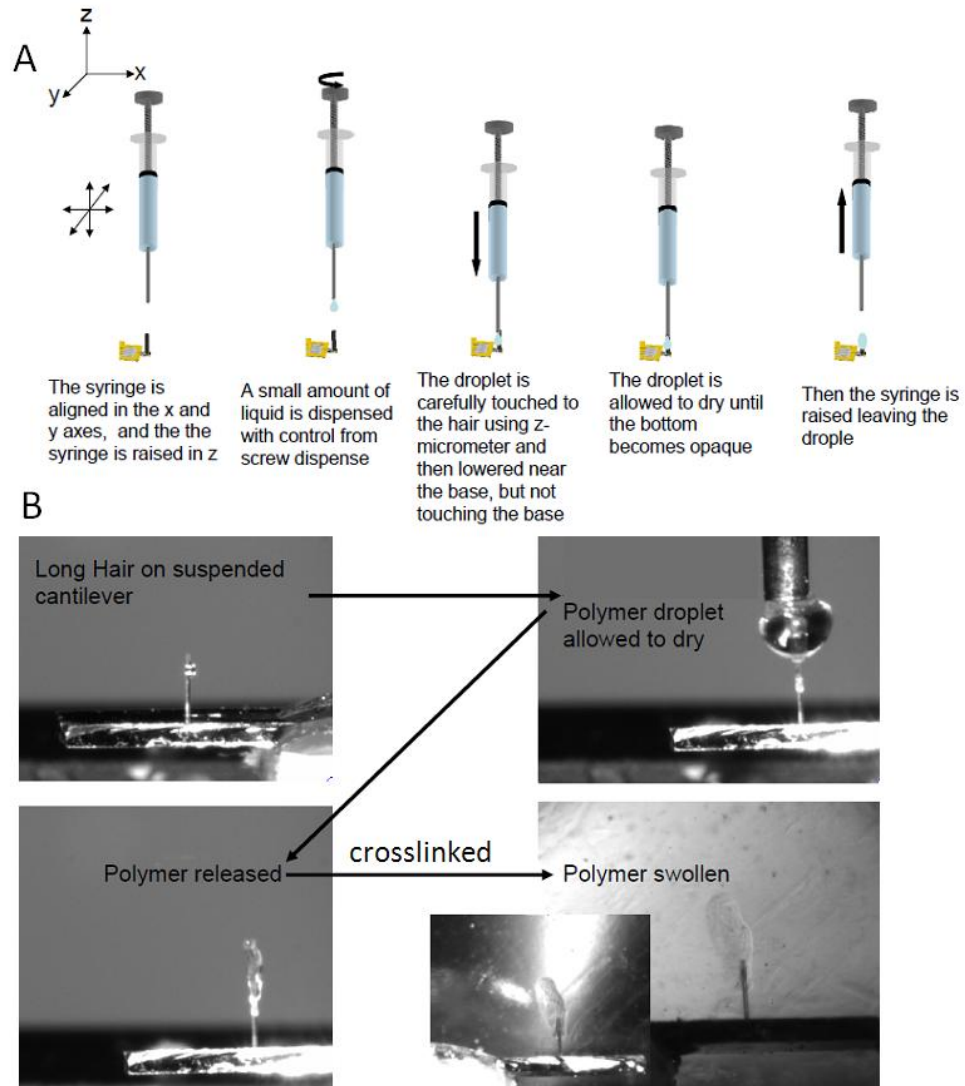


Figure 7.2: Precise Drop Casting. A) A schematic of the precise drop casting process B) Optical picture of a few various steps of the process

Occasionally the precipitation of polymer would nucleate on the syringe, which would cause the droplet to stick to the syringe instead of the flow sensor. In this case the syringe was wiped off and the deposition resumed. If the droplet was allowed to dry too long, then the syringe could become bound to the hair and then damage to the sensor would occur upon the removal of the syringe. Therefore, the syringe was periodically raised several μm , essentially sliding the droplet back and forth along the hair until the

droplet stayed in place and then it was left on the hair. Once the droplet dried, then another droplet was lowered until it made contact with the last drop and it was deposited in the same manner to built tool hydrogel structure.

This method allowed the cupula to be applied to the hair and built up, without wetting the base of the sensor, thereby leading to a high-aspect ratio structures (figure 7.2b). Furthermore, this method provides the ability to control the width and height of the cupula by controlling the dispensed volume of each droplet and by controlling the number of droplets, respectively. The distance from the bottom of the cupula to the base of the hair, can be also controlled. When the synthetic cupula was placed closest to the sensor platform, without actually wetting the platform, the durability and lifetime of the cupula structure was enhanced.

Through experience we found that depositing a cupula which started half-way up the hair and extended past the hair by about 50 % was a good balance between robustness, height and preventing wetting of the platform. In the case of the tested sensors, the microfabricated hairs were 550 μm long and the base of the dried cupula started at about 275 μm above the base of the hair and ended about 275 μm above the hair, giving the total hair-dry cupula structure a height of roughly 825 μm (figure 7.3b). At this distance, wetting the platform was minimized and still the cupula remained intact for months under a noisy environment. Furthermore, when the hydrogel cupula was allowed to swell, the base of the cupula nearly reached the sensor platform. The full process involved dropping about 10 droplets of solutions to form the desired height and width (see examples of two structures in Fig. 7.3b,d).

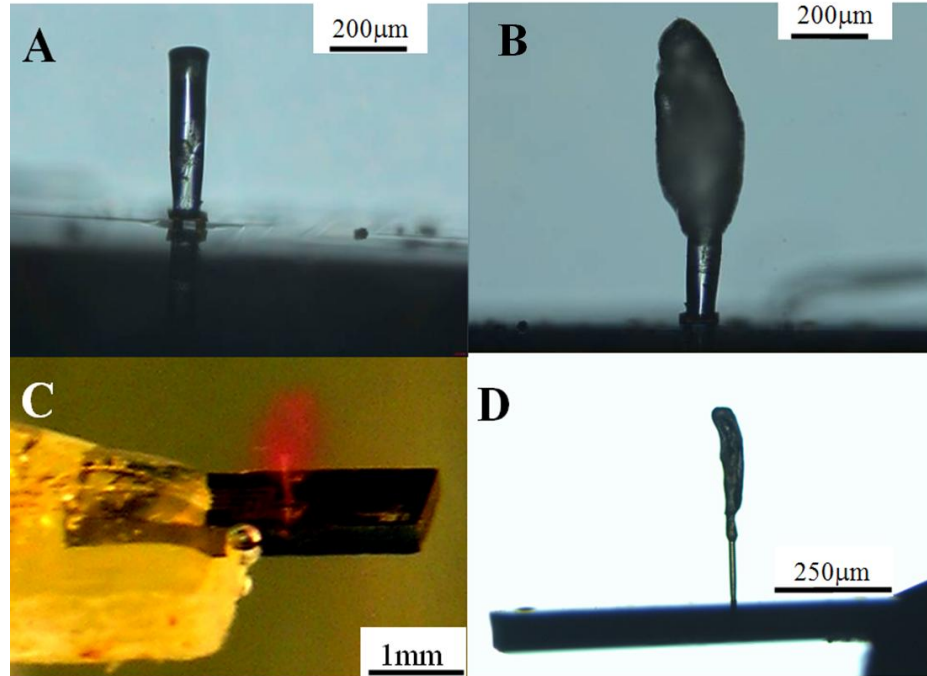


Figure 7.3: High Aspect Ratio Artificial Cupula. The front-view of flow sensor A) before and B) after being coated with the PEG-based hydrogel material. C) A swollen cupula on a working sensor, which has been dyed using rhodamine. D) The side-view of a sensor with a relatively long SU-8 hair, with a very long and high aspect ratio dry cupula.

Once the dried synthetic cupula structure had formed, we cross-linked the functionalized PEG macromonomer by irradiating the sample with UV light (365 nm) for 6 minutes at an intensity of $1000 \mu\text{W}/\text{cm}^2$. Under these conditions, hydrogel structures showed the elastic modulus in the range 5-50 Pa. After the samples were irradiated they were allowed to swell for 45 minutes in the testing water tank before measurements were performed.

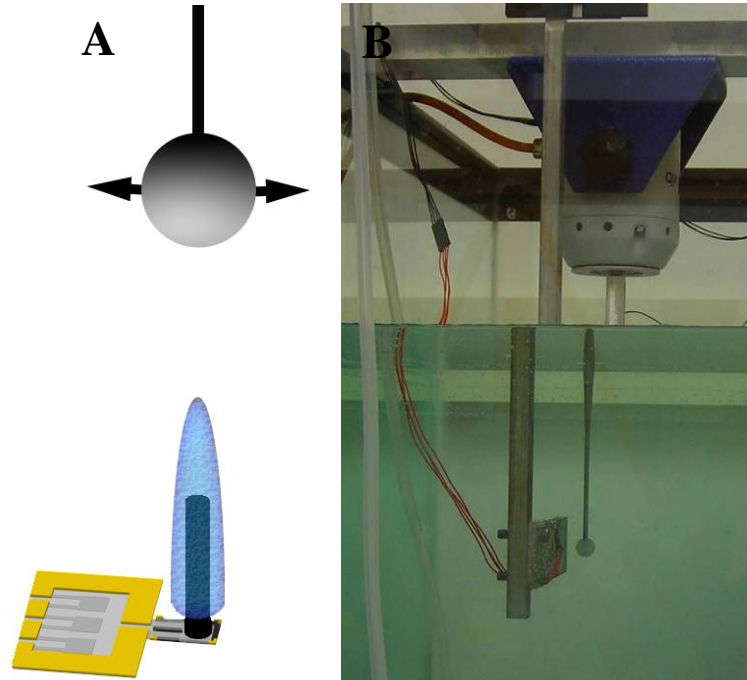


Figure 7.4: Testing of the High Aspect Ratio Artificial Cupula A & B) A permanent magnet shaker was positioned above the sensor and a sinusoidal frequency was applied while the displacement was measured with a sensor embedded inside the dipole.

7.3 Results and Discussion

The completely assembled hair sensors with hydrogel cupula (figure 7.32c) were tested using a permanent magnet shaker that sinusoidally actuated a dipole with an embedded velocity sensor to measure the amplitude and frequency of the dipole movement. The sensors were mounted on a metal platform connected to a micrometer, which accurately controlled the distance of the sensor platform to the dipole, all element placed in a water tank mounted on an air table (figure 7.4a, b). The sensors were mounted such that the dipole moved perpendicular to the long axis of the hair. The “bare” sensors were tested at a distance of 15 mm away at a constant frequency of 50 Hz. At 15 mm, the dipole shaker is capable of producing a minimum flow velocity of 85

$\mu\text{m/s}$, which was below the sensing threshold for the “bare” sensor. After the addition of the cupula, the sensing threshold was much lower and therefore required moving the dipole to 45 mm to fully capture the sensing threshold.

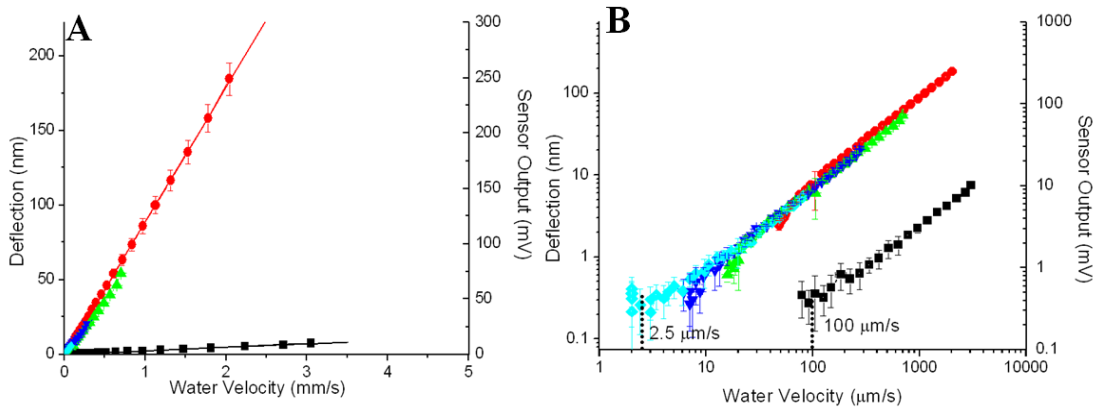


Figure 7.5: The Performance of the High Aspect Ratio Cupula. A) The results of the minimum threshold deflection measurements plotted on a linear scale, clearly showing an improvement in the sensitivity of 40 times. B) The results of the threshold deflection measurements plotted on a log-log graph, clearly showing an improvement in the threshold deflection of 40 times. A-B) \blacksquare “bare” sensor response at 15mm from the dipole, \bullet , \blacktriangle , \blacktriangledown , \blacklozenge sensor response with cupula, 15 mm, 22 mm, 30 mm, 45 mm from the dipole, respectively.

The results of the test showed a dramatic improvement with the addition of the high aspect hydrogel cupula onto hair sensor (fig 7.5a). The signal output which is proportional to the hair deflection increases linearly with flow velocity but overall slope is much higher for modified sensor. Initially, the bare sensor had a velocity sensitivity of $1.2 \text{ nm}/(\text{mm/s})$ (nm hair deflection per a mm/s flow velocity) and $3.2 \text{ mV}/(\text{mm/s})$ (sensor output per mm/s flow velocity) with maximum deflection reaching only 10 nm. After the addition of the hydrogel cupula the sensitivity improves to $45 \text{ nm}/(\text{mm/s})$ and $122 \text{ mV}/(\text{mm/s})$, an overall improvement of 38 times (fig 7.5a). The “bare” sensor had a

minimum velocity threshold of 100 $\mu\text{m/s}$ (defined by signal output equal to background noise), but after the sensor was coated with the high aspect ratio cupula the threshold was 2.5 $\mu\text{m/s}$, an improvement of 40 times (figure 7.5b). This improvement was very repeatable for different distances and sensors (figure 7.5b). After coating a second sensor with a very similar cupula the velocity sensitivity improvement was 36 times and the minimum threshold velocity was improved from 200 $\mu\text{m/s}$ to 6 $\mu\text{m/s}$ an overall improvement of 33 times.

7.4 Conclusion

In conclusion, by using a soft hydrogel material that was patterned into a higher aspect structure we were able to improve upon our previous design, resulting in a drastically improved sensor. The improved sensor has minimum threshold flow velocities as low as 2.5 $\mu\text{m/s}$, which is extremely low as compared to current available sensors and even the biological analogue. Estimates of velocity sensitivity threshold for fish flow receptors varies significantly, with those derived from AC signals being as low as 18 - 38 $\mu\text{m/s}$ for frequency range 10 – 20 Hz²¹⁶ and those from unidirectional, DC flows to even above 1 cm/s.²²⁴ Therefore, with the addition of high-aspect ratio hydrogel cupula to the hair sensors, we were able to impart sensing abilities that are truly rivaling the performance of fish flow receptors.

CHAPTER 8

CUPULA ARRAYS AND FIBRILS FOR FLOW SENSING

8.1 Introduction

As mentioned in the introductory chapter, the fish lateral line is made of many receptors covering the fish (figure 8.1). The spatial distribution of the cupula provides spatial information to the fish that is key to interpreting the flowing environment. It was also mentioned in Chapter 1, that blind cave fish neuromasts have fibrils embedded in their cupula (figure 8.1B). These fibrils appear to help support tall cupula and to couple the hair cells to the cupula. These fibrils function as scaffolding structures to support the viscous hydrogel that stands several times higher than the hair cell itself in the completed system. By supporting the hydrogel, the aspect ratio of the hair cell is greatly increased, which is predicted will enhance the sensitivity of the sensor. We also wish to demonstrate anisotropic cupula shapes, which fish use to enhance directional sensitivity (figure 8.1C).

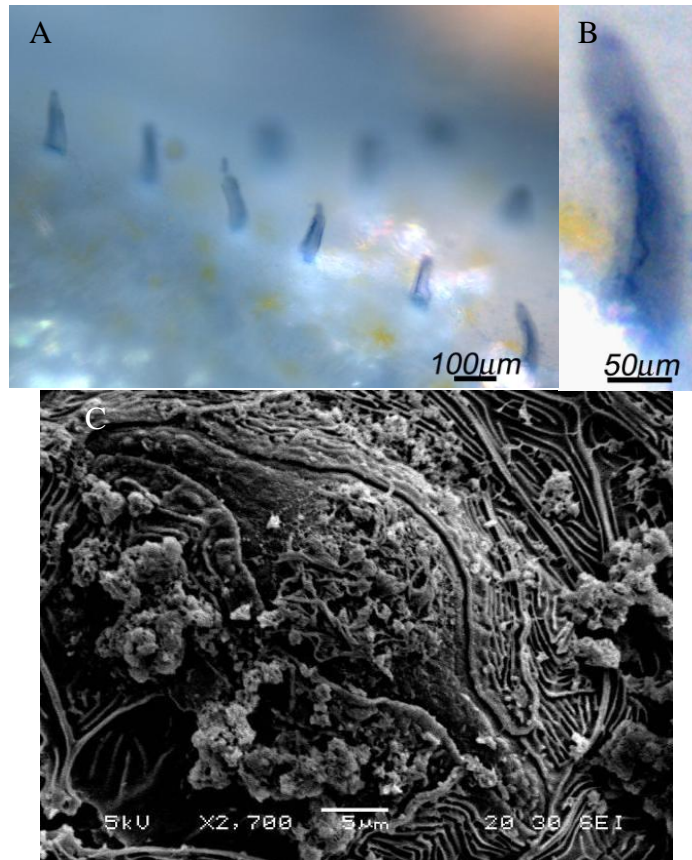


Figure 8.1: An Array of Fish Cupula, Cupular Fibrils and Anisotropic Cupula. A) A row of neuromasts and associated cupula B) A single cupula showing the fibrils C) An SEM of an anisotropically shaped blind cave fish neuromast footprint, of which develops into a anisotropic cupula.

Therefore, another goal of this work is to demonstrate shape control and to the ability to create cupula arrays. Shape control is essential to the fabrication of artificial cupulae, along with the ability to pattern arrays of many cupulae at one time to recreate hair arrays. Shape control of the hydrogel should meet several criteria. First, the shape must reproduce the original photomask pattern showing a final shape that has consistent x-y dimensional ratios, thus retaining the same footprint as the intended shape. Second, the swelling in the z direction must be controlled to tune the aspect ratio of the hydrogel. By patterning the shaped hydrogel, we can rapidly create artificial cupula on sensor arrays that have high aspect ratios and directional sensitivity. Incorporating a similar

shape control design for sensors arranged in different orientations along the surface of an underwater vehicle can be used for directional sensitivity of hydrodynamic flow fields.

Here, we focus on the fabrication of simple arrays of hydrogel microstructures with pre-determined shapes (dome-like, elliptical, and crescent) by applying patterned photopolymerization to control the lateral dimensions. This approach is combined with utilization of electrospun vertical microfibers to enhance vertical dimensions and create hydrogel structures with high aspect (height to diameter) ratios. We demonstrate the components necessary for construction of the arrayed hydrogel microstructures with well-controlled shapes and mechanical properties, which are necessary for fabricating a viable bio-inspired flow sensor system.

8.2 Materials and Methods

8.2.1 Hair Substrates

All sensor hairs from SU-8 photo-resist utilized for testing were manufactured and provided by the Liu group. The hairs used were made from SU-8 deposited on the surface of a silicon cantilever with an average height of 500 μm and a diameter of 80 μm .

8.2.2 Shape Control and Patterning

For shape control and arraying, PEG was dissolved in methanol (20% by wt.), and the photo-initiator listed above was dissolved in to the polymer solution (~5% by wt). Several drops of a PEG monomer-UV initiator solution were deposited on a

functionalized silicon surface and allowed to briefly dry. Shape control was performed during UV photopolymerization, where a photomask (silver pattern on glass) placed between the UV source and the sample was used to pattern cupulae of various shapes, as well as arrays of controlled dimensions and a number of structures. The polymer solution was exposed through an aperture to ultraviolet light at 365 nm light at $1000 \mu\text{W}/\text{cm}^2$ for six minutes with the UV photomask suspended between the polymer and the light source. The silicon substrate and crosslinked polymer were submerged in Nanopure water and allowed to swell overnight. Upon immersion in water, only the photo-crosslinked polymer in the exposed area swelled as a hydrogel, while the rest of the uncrosslinked polymer dissolved in solution. This technique was applied to generate both single and patterned arrays of shaped hydrogels. These samples were then stained with methylene blue dye for better optical clarity for imaging and evaluation of the final shape and dimensions.

8.2.3 Electrospinning

Electrospinning was used to generate polymer nanofibers by electrostatically ejecting a polymer solution from a capillary tube under an applied electric field to create long thin fibers around the haircell along with smaller fibers with diameters as low as 100 nm^{225, 226}. However, electrospun fibers tend to splay as they reach their target making it difficult to cover the hair sensor with an exact and uniformly repeatable deposition. To achieve deposition control, focusing rings were used to help narrow the region where the fibers would be deposited²²⁷. Electrospun nanofibers were formed by inserting an electrode to a solution of Polycaprolactone (PCL) in acetone (17.5% wt.), which was held

in a Pasteur pipette.²²⁸ This apparatus uses two positive high voltage sources and a target connected to ground, as is shown in figure 8.2. A CircuitSpecialist CSI 300 3X5 DC Regulated Power Supply was used in conjunction with a Gamma High Voltage Research HV Power Supply (UC5-10R) as the high voltage source to create an electric field to eject a thin polymer fiber from the capillary to the collection plate²²⁵. Slight pressure was applied to the pipette to begin flow of the polymer and the applied electric field continued to propel the solution toward the target. As is conventional, the solvent in the solution evaporated as the polymer traveled to the target, leaving only a continuous polymer fiber collected around the hair. The PCL was passed through a single 5 cm diameter copper focusing ring used to control excessive splaying of the polymer by creating a uniform electric field for the polymer to move through. The ring was positioned to direct the trajectory of the polymer fiber to a point on the target haircell. The copper ring was attached to a second voltage source and biased slightly less (10 kV, as opposed to the Pasteur pipette at 10-12kV) than the polymer solution. The bias of the copper ring was sustained below the polymer solution to maintain an effective bias toward the collection plate. This required fairly precise position between the ring and the pipette tip, where they were nearly level in the vertical and the pipette tip was centered in the ring's lateral dimensions. A 3-axis micrometer was used to move the Pasteur pipette with respect to the tip.

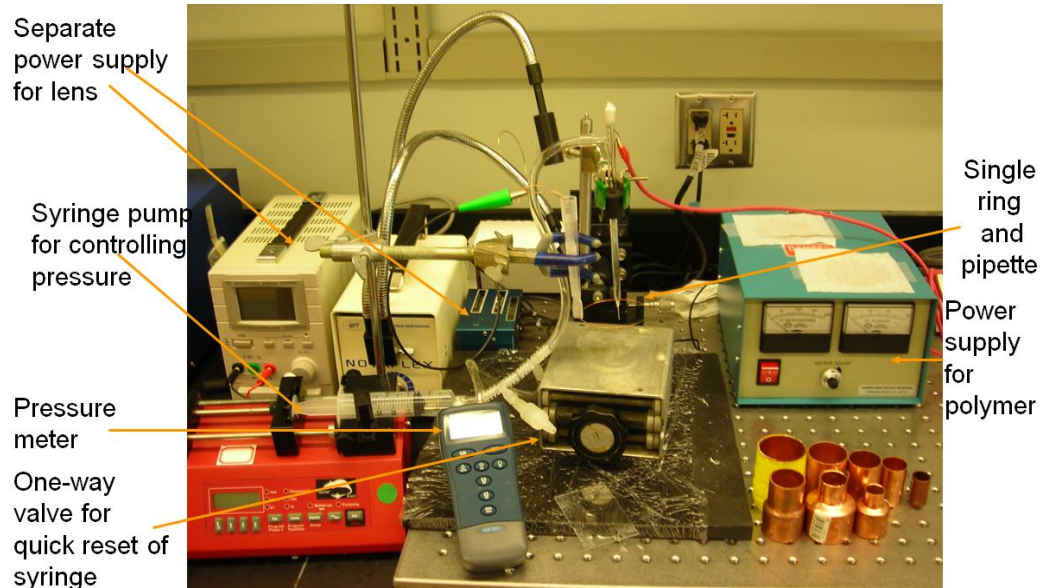


Figure 8.2: The Electrospinning Setup

The target hair structure was sputtered with gold so that the specimen would be conductive, and the specimen was positioned at the collection plate 35 mm from the pipette such that fibers would collect on the hair. After the fiber was spun on the hair to the desired height, PEG solution was drop-cast over both the electrospun fibers and hair structure. The hair cell with the polymer was then exposed to the UV light to activate the crosslinking of the polymer. The entire hair assembly was then immersed in Nanopure water overnight for swelling. Parameters such as the applied voltage to the PCL solution and the focusing ring, target separation distance, polymer viscosity, were varied to produce optimal characteristics of electrospun fibers for high-aspect ratio cupulae. It should be said that with too much biased voltage, the fiber stream would be completely blocked by the field. It should also be stated that even with the sputtered gold film, this technique essentially was a line of sight technique. Therefore, poor lateral alignment with the hair would still result in a tall fiber structure, but grown from the substrate instead of the hair. This occurred even when the surface was blocked from being

sputtered. In order to get the shorter lengths we desired for cupular support, the voltage was essentially pulsed. Although, the system repeatedly formed tall structures, the alignment of the hair underneath this stream was difficult. In many ways the alignment issues of this setup are similar to the precision drop-casting process. Although on the other hand they are much more stringent because dropcasting process involves bringing a pipette to a close proximity of the hair, instead of aligning from several cm away. Furthermore, the dropcasting involves aligning a relatively large droplet, as is evident from figure 8.8C. Nonetheless, a few simple improvements would have likely led to better uniformity, such as a fiber optic laser shined through the pipette for alignment or a fiber optic camera.

8.3 Results and Discussion

8.3.1 Cupula Shape Control

Shape control of the hydrogel was achieved by using UV polymerization of photo-crosslinkable PEG monomer placed under a photomask printed with the desired shapes as shown in figure 8.3, 8.4, 8.5. Through this fabrication technique, we were able to achieve excellent microscopic shapes of the hydrogels using the photomask exposure system.

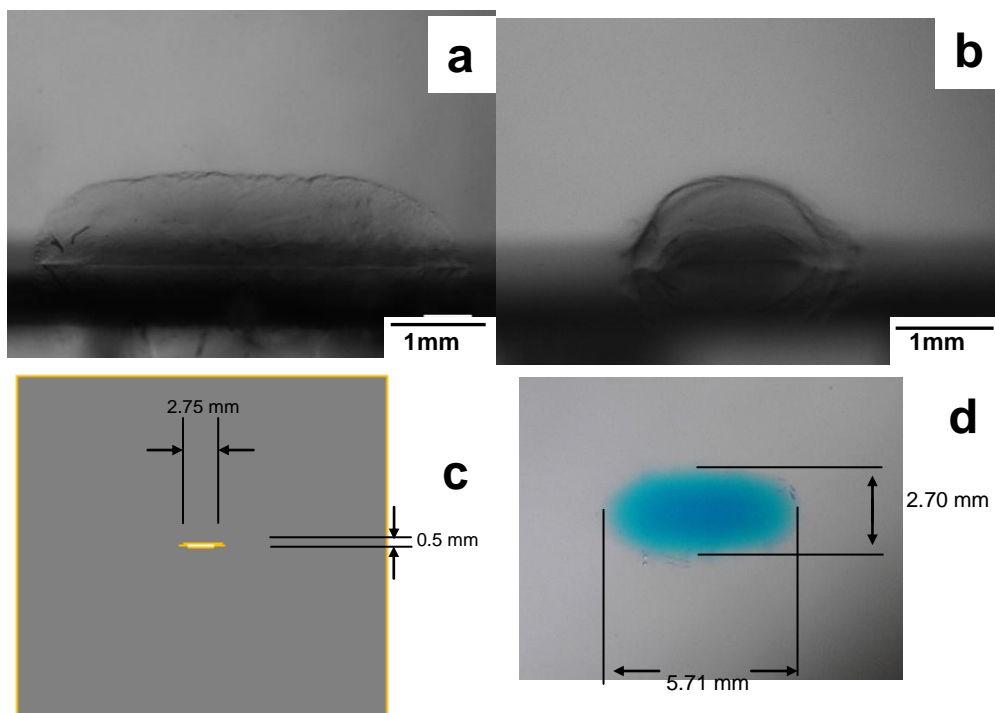


Figure 8.3: An Elliptical Shaped Cupula. Images of (a) Side view of elliptical shaped hydrogel, (b) End view of elliptical shaped hydrogel, (c) Photomask used for exposure of elliptical shaped hydrogel, (d) Top view of elliptical shaped hydrogel with methylene blue dye added for optical clarity.

The polymerized PEG swelled as a hydrogel with dimensional ratios virtually identical to that of the photomask aperture used during photopolymerization as seen in figure 8.3. The long oval shape was retained from the photomask pattern to the hydrogel but expanded outward more than it extended lengthwise. This type of swelling was seen in all samples where they are more likely to swell along the direction with less restriction, which is usually outward. This shows that the PEG hydrogel will swell as desired when the shape is symmetrical and also when the shape is asymmetrical indicating that it is possible for other complex shapes to be created using this technique.

The swelling ratio is measured as the final dimension of the swollen shape over the dimension of the photomask pattern. For the crescent moon sample seen in figure

8.4, the swelling ratio for x-y dimensions is consistently between two and three. However, the ellipse in figure 8.4 shows a slightly more distorted ratio with the x (long) direction ratio being around the expected value of two but the y (short) direction swell was greater with a ratio of about five. This greater swelling ratio in the y direction is most likely due to unrestricted expansion along the lateral dimension of the hydrogel, whereby the system could swell unhindered by its own expansion as happens in the swelling in the x direction. There is a larger surface edge area that can expand outward allowing the hydrogel to become much wider. This pattern indicates that as the hydrogel is swollen in water, it will expand more in any direction where there are no constraints placed on its expanding edge.

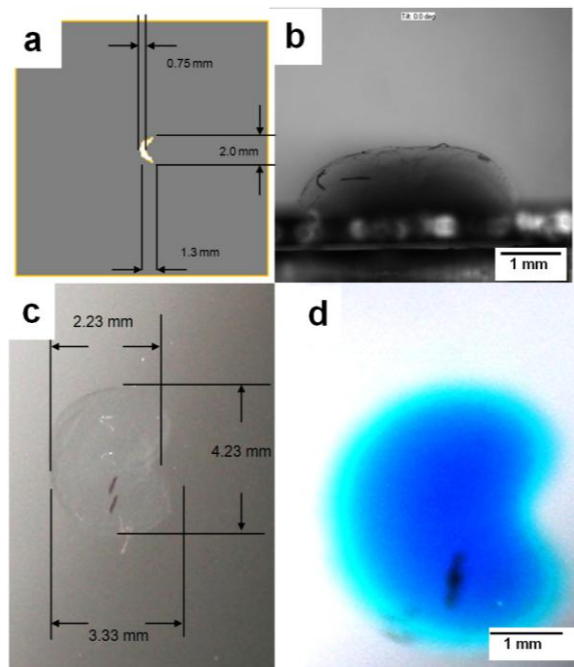


Figure 8.4: A Crescent Shaped Cupula. Images of (a) Crescent moon photomask used to pattern PEG during UV-light exposure, (b) Side view of swollen hydrogel, (c) Dimensions of swollen hydrogel sample, (d) Image of dyed hydrogel sample for optical clarity of final shape.

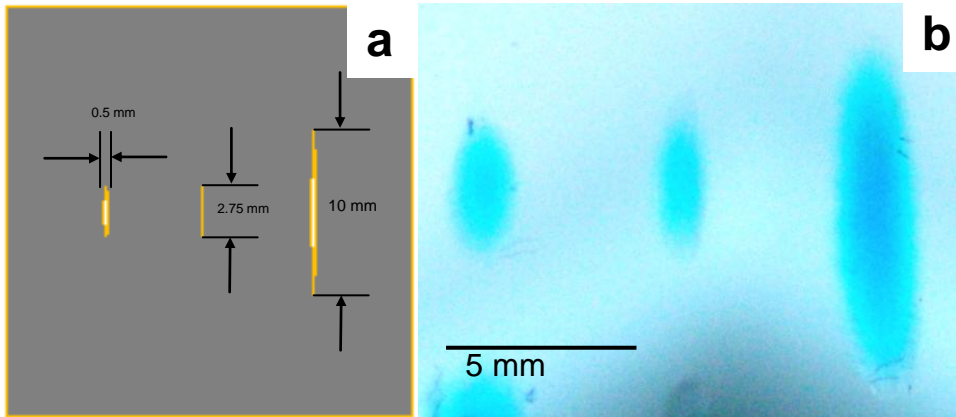


Figure 8.5: Parallel Fabrication of Multiple Cupula. Image of (a) Patterned photomask for creation of multiple cupula at once, (b) Exposed and swollen hydrogels for multi component patterning.

After swelling, the hydrogel was stained with methylene blue (figures 8.3, 8.4, & 8.5) for optical clarity and to emphasize the shape retention of the swollen polymer in comparison to the photomask. During the photo-exposure of the hydrogel, the UV light exposed a slightly larger area of the hydrogel than intended by the photomask due to scattering effects in the photomask. Additionally, since there was a slight separation between the mask and the sample, the exposed area was seen to be slightly larger than the printed shape from this as well. These systemic artifacts can be corrected for by creating photomask patterns that are slightly smaller than the desired final size so that the correct area will be exposed.

In addition to the single shape control shown, we demonstrated patterned shape control using a single photomask to crosslink and shape several areas of hydrogel in an array during a single UV exposure. Arrays of various shaped cupula were generated, and the long and thin geometries are especially applicable for directional sensing, as shown in figure 8.5. Demonstrated arrayed hydrogel structures would allow for rapid

manufacturing of these sensors with precise control of the shape for directional flow sensing.

Overall, dimensional ratios of the aperture geometry proved stable and were reliably maintained in the swollen hydrogel cupulae, which is essential to the repeatable construction of the sensors. The shapes of the hydrogels have remained simple thus far as circular or elliptical shapes with the most complex being the crescent moon shape. Generally, more complex shapes can be created as long as the expected swelling ratios are accounted for when designing the pattern. This should allow many other shapes to be created as needed, but the shapes will typically be limited to rounded, coarse geometries for the time being as sharp features are difficult to control due to the nature of hydrogel swelling. The UV-photolithography process used for shape control demonstrates a quick and reliable method for creating many different shapes and sizes of hydrogels quickly that can be adapted to any process that shape controlled hydrogels are needed. We focused on the ellipse and crescent moon shapes because they hold promise for directionally sensitive sensor systems.

8.3.2 Electrospun Fibrils and Cupula Aspect Ratio

As was mentioned above, the superficial cupula of blind cave fish is a composite structure composed of a very compliant bio-hydrogel supported by a relatively dense network of long fibrils. In order to further leverage our bio-inspired cupula, we adapted an electrospinning technique to fabricate tall micro/nano-fibrillar structures on top of the hair sensor. An in-depth review of electrospinning is beyond the scope of this dissertation, but one may refer to relevant papers.^{225, 229,230,231}

The electrospinning process was used to create the additional vertical fibrillar structures to support the hydrogel cupula as a means of increasing vertical stability of the hydrogel to achieve the desired high aspect-ratio cupula geometries (up to 5-10). Conventional electrospinning on the sensors resulted in the spun fibers laying flat parallel with the substrate, with some fibers crossing over the hair forming a teepee net like structure, as shown in figure 8.6.



Figure 8.6: Conventionally Electrospun Fibers onto a SU-8 Hair

In order to obtain tall electrospun fibers, an electrically biased focusing ring was used to repel the fiber to prevent it from deviating from a straight path. For our system, only one copper ring was necessary to create a sufficient electric field for adequate stabilization of the ejected polymer through a 35 mm trajectory. This approach of using focusing rings to better control the trajectory of the ejected polymer was proposed by Deitzel et al. to eliminate the precession of the PCL as it traveled to the target when no additional electric field is present.²²⁷ The typical precession is the causes the spun fiber to coil around a given target, instead of landing straight to build up a tall structure as needed. The focusing ring, when aligned properly, prevented the polymer from coiling as

it was deposited on the target and instead the fiber piled up on top of itself, thereby allowing the tall, thin structures to be built that were necessary for support of the high aspect ratio cupula.

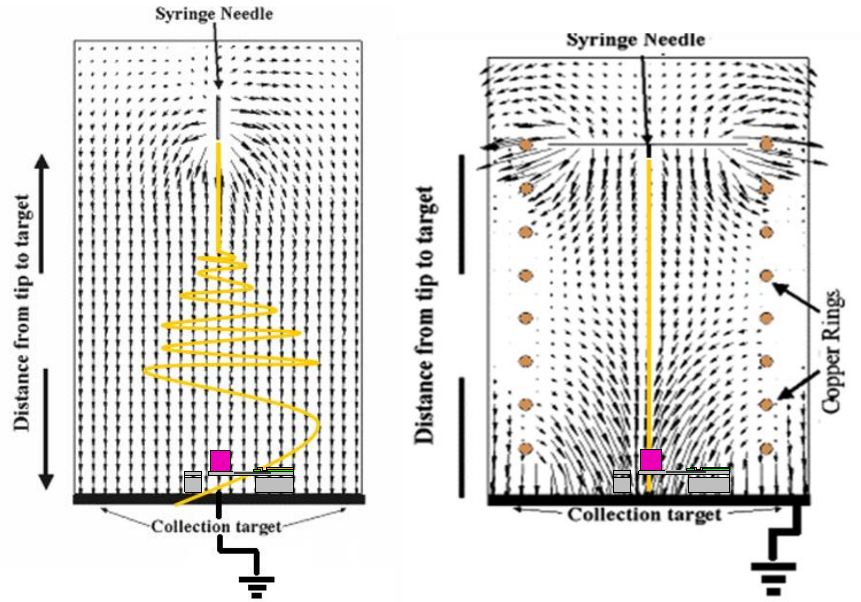


Figure 8.7: Schematic Showing Effect of Biased Coils on the Electric Field (Image provided by D. Lu).

By controlling the trajectory of the polymer with an additional electric field, the fibers showed a much more uniform and linear shape as opposed to when PCL was deposited without the use of a focusing ring. Essentially the focusing ring acted to extend the stability region, so that the fiber dries and is deposited before the bending instability forms. By avoiding this bending instability, the fiber velocity is much slower and the fiber is thicker because it has not been stretched. To take full advantage of the focusing ring, alignment of the electrospinning deposition on the hair sensor was critical to facilitating the generation of the fibrous support structures directly on the hair sensor. By precisely setting the alignment, the PCL would be deposited on the previous layer building up the tall fibers used as support structures. Occasionally the creation of vertical

fibrous structures taller than 30 mm was possible under these conditions and structures as tall as 10 mm could be generated that would support the deposition of PEG monomer solution (Figure 8.8). However, fibers of shorter lengths of 0.5 to 2 mm were typically used in the final sensor structures since they proved more robust under PEG deposition and UV exposure than the taller fibers. Nonetheless, the focusing ring successfully eliminated the problems of coiled and dispersed fibers and helped to create much more uniform fibers as seen in the final product. Therefore, this focused electrospinning approach allowed us to fabricate bio-inspired cupular fibrils, which allowed us to build up artificial cupula quite tall.

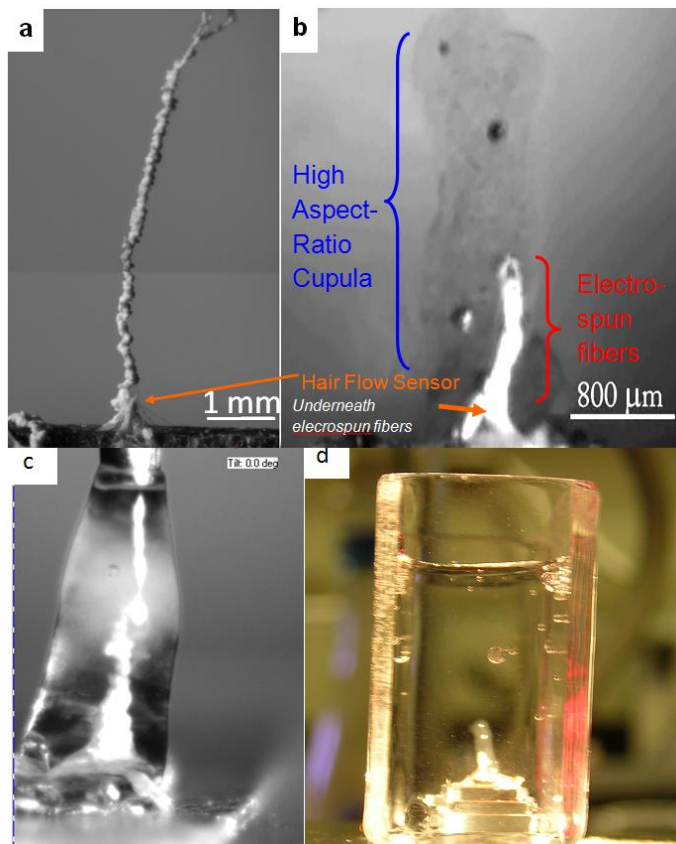


Figure 8.8: The Cupular Fibrils and Cupula Supported by Fibrils. Optical images of (a) Hair sensor with large cupula support structure from spun fibers (b, c) Hair sensor with middle electrospun fiber cupula support and hydrogel cupula attached (d) overall view on toll hydrogel structure.

8.4 Conclusions

It is important to optimize the sensing abilities to in order to fully leverage microfabricated flow sensors for flow based imaging. Furthermore, it is critical to use an array of sensors, essentially creating the pixels for “flow based imaging”. To leverage the microfabricated sensors and the bio-inspired signal absorbing cupula, tall cupular fibrils were fabricated and arrays of cupula were patterned in various shapes. We expect further sensitivity gains through the cupular fibrils by expanding the signal absorbing structure farther from the boundary layer and by enhancing the cupula-hair coupling. By extending the functional length of the sensor with the electrospun fiber, the hydrogel cupula was able to be extended to about 3 times the height of what an unsupported hydrogel cupula would be able to swell to. This allowed for a greatly enhanced aspect ratio hydrogel cupula reaching 5:1, which is a necessity in creating more sensitive sensors similar to superficial biological cupulae. By using the spun fiber as support to increase the height of the hair cell and the overall aspect ratio of the hydrogel cupula system, we can expect to see even further leveraging of our bio-inspired approach to obtain further sensitivity gains. Much like fish, we were able to create anisotropic cupula in arrays, which should help to enhance the directional sensing capabilities and the overall ability to image the environment via flow fields.

CHAPTER 9

FIRE-BEETLE INSPIRED PHOTO-THERMAL SENSING

9.1 Introduction

Infrared imaging by biological species is another intriguing example which could be served well by examining biology for material-based approaches to sensing. Modern infrared (IR) imaging with artificial detectors can generally be broken into two different categories: photon-based and thermal-based.^{232,233} Until relatively recently, most of the IR imaging development focused on photon sensors. Thermal based detection, which involves transducing temperature, changes from the infrared absorption, was considered slow and insensitive. After decades of development, thermal-based detectors are being re-examined as an alternative to expensive photon detectors. After more recent developments, thermal-based IR detection is being revisited as an option for cheap and relatively sensitive detectors with TV-rate scanning speeds. Thermal-based detection includes a myriad of transduction techniques including bolometers and Golay cells, with sensitivities still usually below record values set by the nature.²³³ To develop novel material-based strategy towards photothermal sensing, here we consider one interesting example of thermal biological receptors.

Melanophila acuminata, or commonly called “fire beetles”, are attracted to forest fires from great distances, at least 0.5-3 miles and maybe even up to 50-100 miles away Figure 9.1.^{234,235,236,237,238} As discussed in introductory chapter, they mate and lay their eggs in newly burnt trees, which are ideal for their larvae. The beetles find these distant forest fires through the use of their IR receptors. These pit organs are made of almost

100 spherical cap shaped receptors located on their thorax near their middle legs.^{239,240} Each organ is made up of a cuticular sphere covered by a protoplasmic layer, which is roughly 300 nm thick. The sphere appears to freely hang in a cavity within the cuticle stalk. Although, it is quite clear that these receptors exploit a photo-mechanical transduction mechanism, the exact details of the mechanism are somewhat ambiguous.^{241,242} There are two conceivable hypotheses of the transduction mechanism, a thermal-pneumatic mechanism and a solid thermal expansion mechanism.

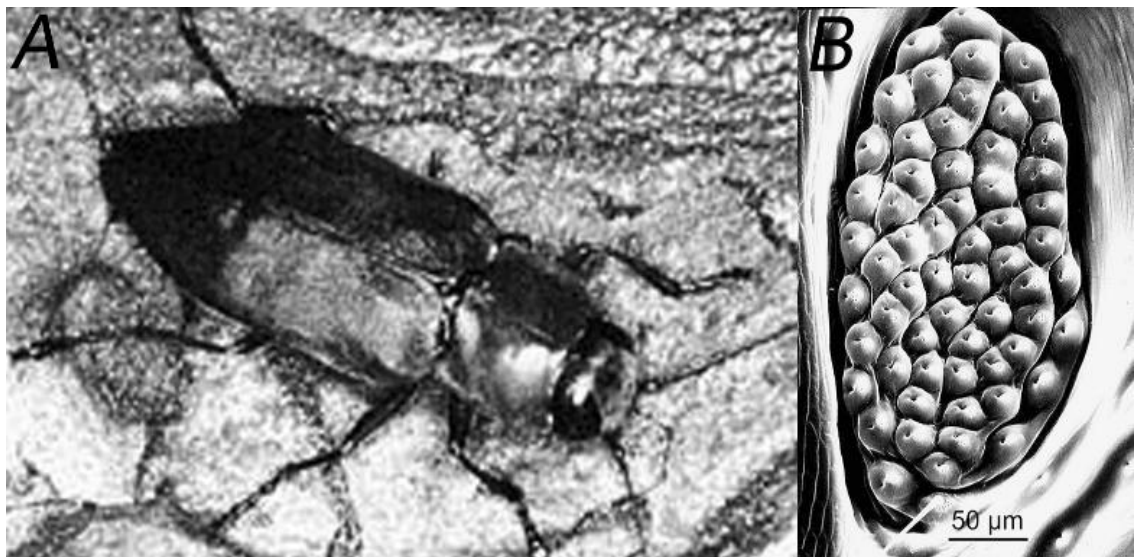


Figure 9.1: The Fire Beetle Photo-thermal Receptor. A) The Fire Beetle, arrows indicate location of IR sensing pit organ receptors B) An infrared pit organ composed of an array of micro-scale IR receptors. (From Reference 81)

Initially, the fire-beetle offered much motivation for our work, in that we knew thermal-mechanical transduction was promising and deserved further investigation. We started by developing ultra-thin, flexible, freely-suspended membranes, much like the fire beetle employs. Initially, our work focused on thermal-pneumatic transduction because thermal expansion transduction from a non-bimorph ultra-thin film seemed unfeasible. It

should be mentioned, that previous work had demonstrated such a non-bimorph thermal expansion based IR sensor, which was also inspired by the fire-beetle.²⁴³ The sensor was made from a Teflon disc (cm-diameter) wedged against piezoelectric crystal; upon absorbing IR radiation the disc would expand and deform the piezo-electric crystal, thereby producing a voltage signal. Despite the impressive capabilities of this bio-inspired sensor, it seemed impractical to scale this design to a micro-scale multi-pixel imager.

As will be discussed, after the thermal-pneumatic transduction work, we developed a new bio-inspired non-bimorph thermal expansion transduction that can be scaled down to very small sizes. Furthermore, by exploring both possible mechanisms employed by the fire-beetle, we were able to develop sensors with impressive properties and this engineering work may prove useful in further biological investigations of this creature.

9.2 Materials and Methods

9.2.1 Layer-by-Layer Deposition

Layer-by-layer (LbL) deposition was used as fabrication method to create freely suspended ultra-thin films capable of acting as photo-thermal transducing structures, much like the bulbs in the IR-sensing receptor pits of fire-beetles. Traditionally, LbL films are fabricated using dip coating. Freely-suspended films used in this dissertation are prepared using spin-assisted layer-by-layer (SA-LbL) deposition.^{244,245,246} The membranes are made of a series of oppositely charged polyelectrolyte bilayers with a

gold nanoparticle layer in the center. The work presented here concentrates on bilayers of poly(allylamine hydrochloride) (PAH) and poly(sodium 4-styrenesulphonate) (PSS), figure 9.2.

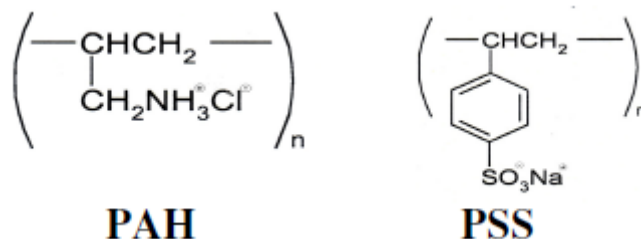


Figure 9.2: The chemical structure of Polyions used to make LbL films

SA-LbL deposition method will be used to fabricate the supportive membranes for sensing applications. Fabricating these robust, uniform membranes is fairly easy using the general method shown below in figure 9.3.

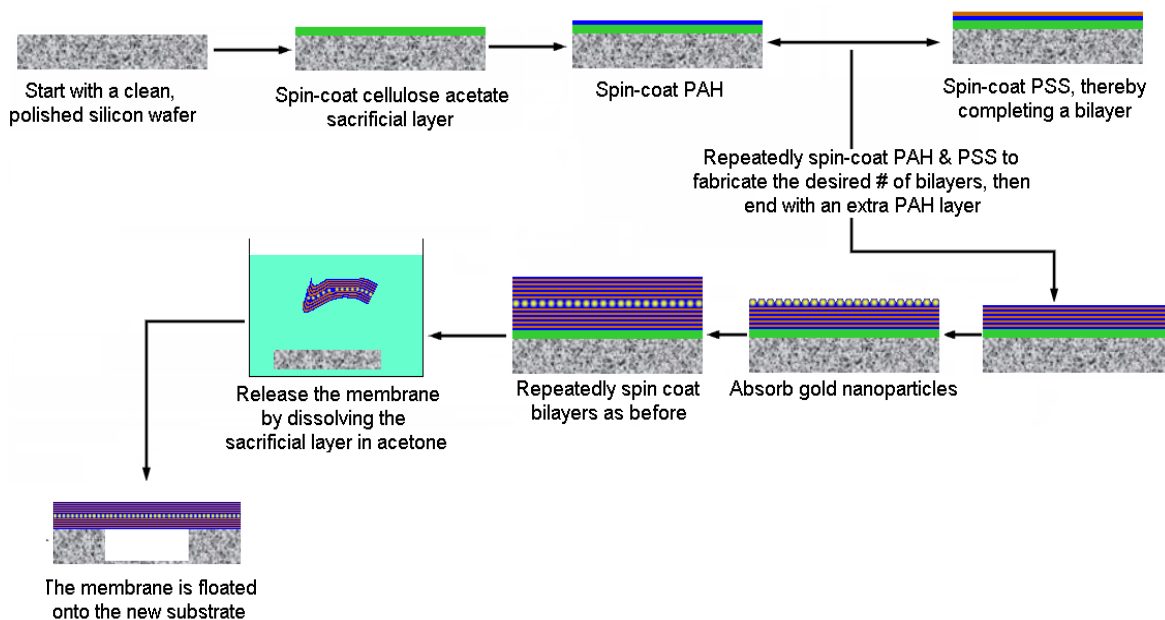


Figure 9.3: Membrane Fabrication Process.

The fabrication process is as follows: first, a polished, clean silicon wafer with a (100) orientation is spin coated with a layer of cellulose acetate (CA) solution. The

cellulose acetate acts as a sacrificial layer, which is later used to free the membrane from the substrate. The use of other sacrificial layers has also been explored. After deposition of the sacrificial layer, then the surface is spin coated with two different polyelectrolytes. The polyelectrolyte being spin coated is alternated (the alternate ionic charges make the layer strongly cohesive); with deionized water spin coated twice in between the polyelectrolyte layers. The water spin coatings wash the excess polyelectrolytes and ions. This is done until the desired number of bi-layers is fabricated. At any point in the bi-layer deposition process nanoparticles can be embedded in the film. These nanoparticles are useful to reinforce the membrane and give the films functionality, such as piezo-resistance. Furthermore, these nanoparticles can act as a dye, which facilitates the handling involved in the release and floating of the film. After the desired number of bi-layers and filler has been deposited, the multi-layered SA-LbL film (still on silicon wafer and the sacrificial CA layer) can be stored for long periods of time, if so desired.

Before releasing the film, it is usually perforated to make many smaller membranes. To release the film, we put the wafer with the LbL film into acetone to dissolve the sacrificial layer. The membrane is floated onto a substrate with a cavity or an array of cavities. The last step in fabricating and mounting a stable, robust freely-suspended membrane is allowing the membrane to dry. This drying pulls the membrane taut and made for a wrinkle free sample.

9.2.2 Interferometry-based Transduction

The interferometer based transduction system was first developed in Prof. Tsukruk's lab in order to measure the elastic modulus and residual stress of freely

suspended films. It is essentially an optical interferometer, which uses interference contrast to quantify distances. A schematic of the test setup is displayed in figure 9.4A. Using this setup, we can acquire an interference pattern of the membrane, which can be directly related to the membrane deflection with ~300 nm resolution. An example of an interference pattern can be seen in figure 9.4B. Figure 9.4C shows a calculated membrane deflection profile using fringe fitting software, QuickFringe.

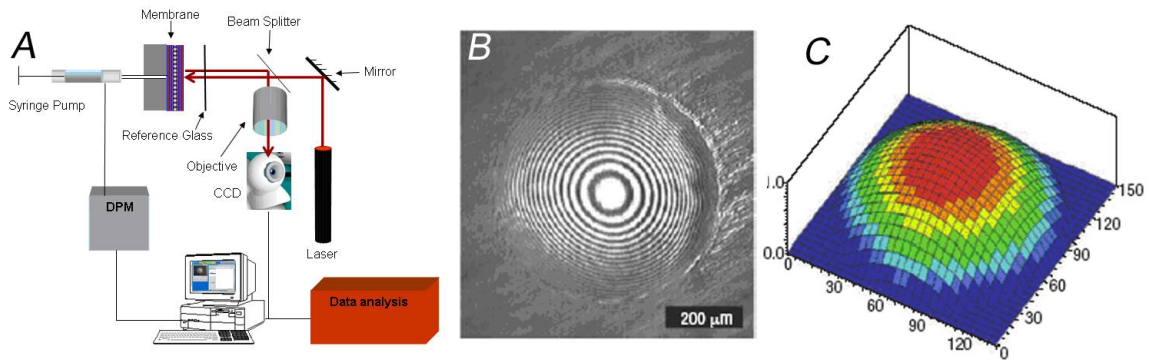


Figure 9.4: Membrane Interferometer Testing A) Bulge Test Interferometer Setup, B) Interference Pattern C) Deflection Profile of Bulged Membrane (Adapted from Reference 253)

Such thermal-pneumatic sensors operate by transducing the deflection caused by increased pressure associated with the raised temperature from infrared absorption. The pressure can be related fairly well to the temperature by the ideal gas law. The deflection profile vs. the pressure can be plotted and related to the elastic modulus of the film using the following equation:^{247,248,249,250, 251}

$$P = P_0 + \left[C_0 \frac{Et^4}{(1-\nu^2)a^4} + C_1 \frac{\sigma_0 t^2}{a^2} \right] \left(\frac{d}{t} \right) + C_2 \frac{Eh^4}{(1-\nu^2)a^4} \left(\frac{d}{t} \right)^3 \quad (\text{Equation 9.1})$$

where P is the applied pressure, P₀ is the initial pressure, E is the elastic modulus, d is the deflection of the center of the membrane, ν is the Poisson's ratio, σ₀ is the residual stress, t is the film thickness, C is constants related to the film geometry (tabulated in the

literature²⁵¹) and a is the length associated with the lateral dimensions (such as the radius for circular membrane). At relatively small deflections, on the order of the film thickness, where the sensitivity, s , is highest, it depends on the radius and thickness with the following relation: $s \propto \frac{t^4}{r^4}$. Therefore, in order to ensure high sensitivity, the sensors must be quite large. Often, they are on the millimeter-scale or larger. This constraint makes the feasibility of realizing multi-pixel imagers from thermal-pneumatics somewhat questionable. On the other hand, as previously discussed, there is good evidence that biology efficiently uses the thermal-pneumatic principle in a very small package. It should be evident that if the deflection is significantly more than the film thickness that the first and second terms become negligible and the third term becomes the principle descriptor of the behavior. Furthermore, we generally test films with thicknesses between 10-100 nm, therefore generally a cubic relation of the deflection vs. applied pressure is expected.

The systems shown in figure 9.4a can be used to characterize the mechanical properties of the film. This is most often done by applying pressure to the membrane instead of heating a sealed cavity.

9.3 Results and Discussion

9.3.1 Thermal-Pneumatic IR-Imagers

As mentioned, these fire beetles, with their highly sensitive miniature receptors, provided motivation to take a second look at miniaturized pneumatic IR transduction.

The thermal-pneumatic transduction mechanism was implemented by covering a cavity with an ultrathin film.²⁵² As this covered cavity is exposed to IR radiation the enclosed gas heats and expands, thereby deflecting the membrane capping the cavity (figure 9.5).

In order to fabricate an array of sensitive Golay cells with a μm -scale footprint, we concentrated on minimizing the thickness of the covering membrane. Ultra-thin polymeric membranes were fabricated via layer-by-layer assembly, which allows excellent control over the thickness and the modulus of the film.²⁵³ A good balance between flexibility, robustness, and reflectivity was obtained with films about 50 nm thick, with a gold nanoparticle layer serving as reflective and reinforcing filler.

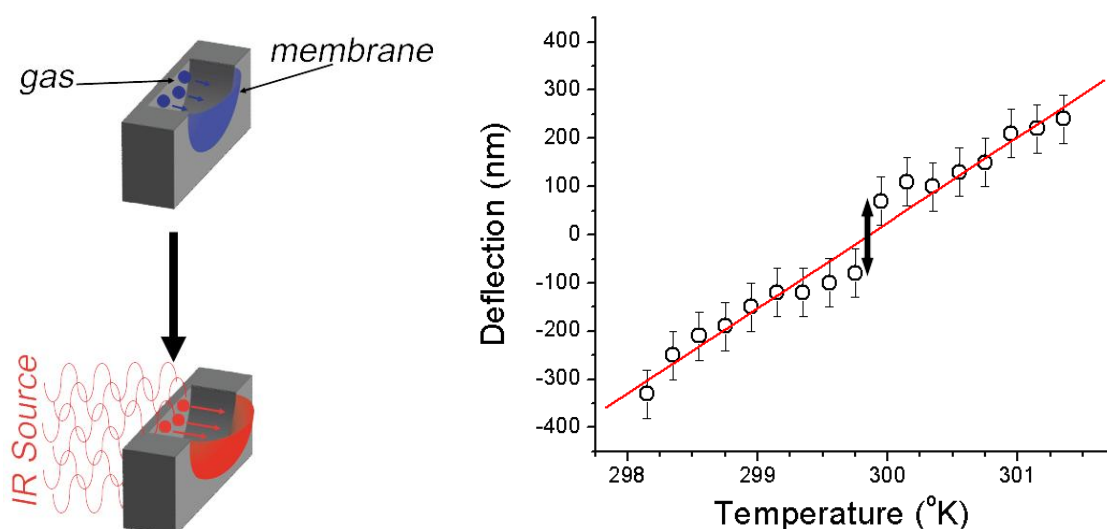


Figure 9.5: Thermal-pneumatic IR sensing. Left: Schematic explaining thermal-pneumatically driven membrane deflection. Right: Membrane deflection vs. temperature, notice the non-linearity at zero deflection.

It was already well demonstrated that these ultra-thin films have negligible gas permeability, thus serving as flexible sealing sensors.²⁵⁴ Furthermore, the composite films have an elastic modulus of several GPa and tensile residual stress on the order of 10

MPa, which occurs during the drying process. It is also important to note that, under large stresses, these films show viscoelastic behavior. The films will reversibly creep, with the strain recovery times exceeding seconds, which is not surprising considering they are composed of an ionic-bound network. To fabricate the thermal-pneumatic imagers these membranes were deposited over microfabricated arrays (64 x 64, 4096 pixels) of 80 micrometer diameter, 100 micrometer deep cavities with 15 micrometer open channels separating each cavity to prevent cross-talk.²⁵⁵

Measurements of membrane deflection with temperature were performed with interferometry in order to characterize the sensitivity of the individual sensors. The overall sensor response was found to be linear for several degrees above and below room temperature, but with a non-linearity occurring at room temperature (figure 9.5). This non-linearity occurred at room temperature over a 200mK temperature change with an overall membrane deflection of 200 nm and is expected from the first and second terms of equation 9.1, when the deflection is on the order of thickness (figure 9.5). The overall sensitivity of the sensor was measured to be 0.12nm/mK near room temperature, except at the transition region, where it reached 1nm/mK. This is vastly more sensitive than conventional microfabricated sensors based on inorganic membranes.²⁵⁶ Furthermore, the sensors demonstrated response times as fast as 60 ms, which is much faster than usual membrane or microcantilever sensors.²⁵⁷

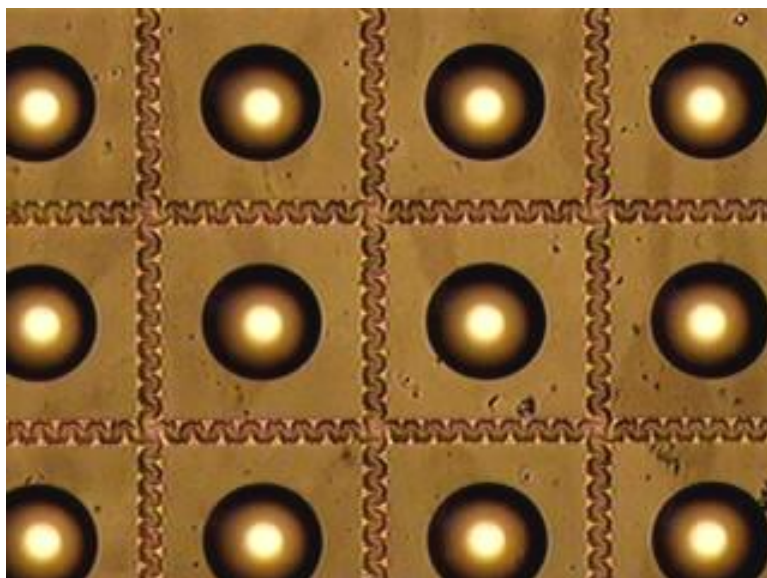


Figure 9.6: Cooling Induced Buckling. An optical image of a cooled sensor array. Notice the worm-like buckling in the trenches and the high contrast of the sealed thermal-pneumatic sensors, which is caused by out of plane buckling.

During the thermal-pneumatic work, it was observed that upon cooling the membranes below a critical temperature, worm-like buckling appeared in the open trenches (figure 9.6). These trenches do not undergo thermal-pneumatic deformation because of their open nature, and therefore were not expected to be affected by temperature changes. The buckling is the result of large thermally-induced changes in the residual stress of the membranes. These worm-like buckling instabilities may be attributed, at least partially, to entropic negative thermal expansion, which is seen in polymers with anisotropic strain, such as cross-linked polymers and aligned fibers.^{258,259,260} As mentioned, these membranes have significant extensional residual stress, on the order of 10 MPa, which could lead to stretching of the polymer material in the film, thereby leading to entropic negative thermal expansion.²⁵⁸

9.3.2 Polymeric Thermal-Buckling Based Sensor Arrays

Buckling behavior of elastic materials has attracted attention in recent years.^{261,262,263} Several papers have explored out-of-plane buckling as a prospective sensing mechanism.^{264,265,266,267,268} It should also be mentioned that theoretical studies have recognized buckling as a possible sensing mechanism that is incredibly sensitive, but has a very small sensing range due to the discrete nature of buckling.^{264,265} Sensitivity could be an order of magnitude higher than that of conventional linear transduction, such as microcantilevers, with μm deflections over incredibly small ranges.²⁶⁴ Much of the enhanced response can be attributed to stress that builds prior to the critical buckling point, which acts to amplify the response. In fact, it is suggested that such huge deflections could likely be transduced optically, thereby eliminating the need for expensive photodetector-based methods.²⁶⁴ But a major issue regarding this approach is to keep the residual strain levels in this critical sensitivity region.

Implementing this transduction mechanism for IR sensing, requires adjusting the residual stress to critical conditions by cooling the membrane below the critical buckling temperature. Then, when the membrane is exposed to incoming IR radiation, it will unbuckle. As mentioned, the open trenches, which are not thermal-pneumatic, had a buckling response after the IR imager chip was cooled below a certain critical temperature and a strong correlation was found between the large optical responses of the thermal-pneumatic detectors and the trench buckling. Upon further investigations, a unique feature was observed in interferometry data taken from the sealed membranes over a relatively large temperature range with the sensors displaying a non-symmetric behavior, which is not predicted by equation 9.1 (figure 9.7).

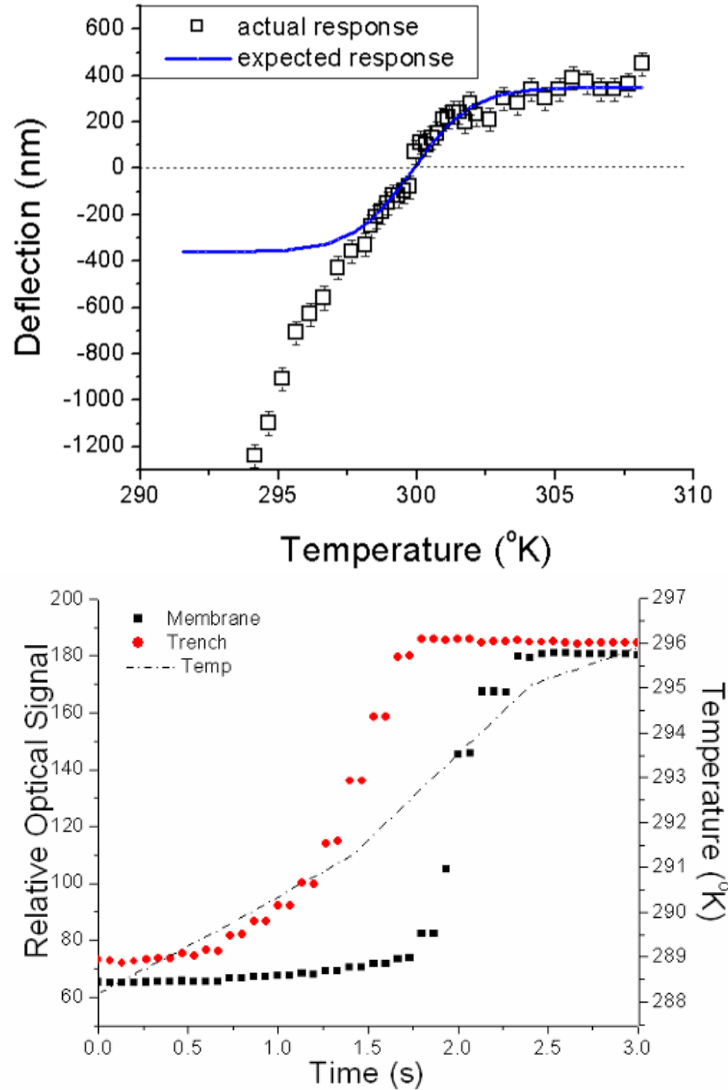


Figure 9.7: Pneumatically-guided Out-of-plane Buckling. Top: Relatively large scale interferometer results, black squares. Notice the non-symmetric behavior around the zero point. The blue line indicates the theoretical behavior of thermal-pneumatic sensors. This huge increase in the sensitivity below room temperature indicates the onset of out of plane buckling. Bottom: A plot, showing the similarity of the optical response of the pneumatic membrane and the worm-like buckling in channels.

This behavior led to huge sensitivities at modestly low temperatures. The sensitivity around 295 K would be expected to be roughly 28nm/K, but in actuality it was measured to be 356 nm/K. These large deformations can be explained as out of plane buckling, which occurs from thermally-induced changes in residual stress. The disparity

between the out of plane buckling of the sealed cavities and the in-plane buckling of the trenches can be explained as pneumatically-guided buckling. In other words, the worm-like buckling and the out-of-plane buckling of the sealed cells are caused by the same phenomena, but the behavior of the sealed cell is offset because of the pneumatic effect. This behavior is logical, considering that the pressure will provide some initial out of plane deformation, which will cause the out of plane buckling to become energetically favorable over in-plane buckling.

The viscoelastic creep of these films caused static measurements of the buckling transduction performance to be somewhat unstable, including diminished buckling with time and changes in critical buckling temperatures. To avoid the viscoelastic problems associated with the huge strains of buckling, the membranes should be operated in a dynamic mode. This was accomplished by cooling the membranes with a temperature-controlled thermo-electric cooler, while exposing them to chopped infrared laser light (figure 9.8).

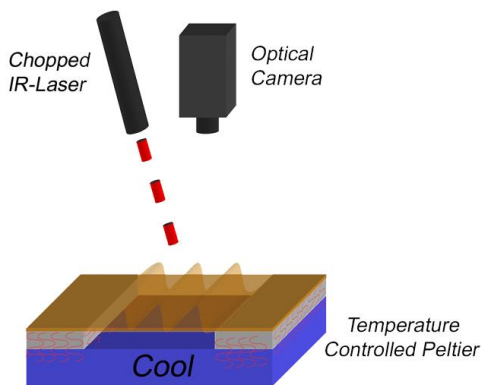


Figure 9.8: Thermal Buckling Transduction Experimental Schematic: A schematic showing the experimental apparatus used to obtain and characterize the dynamic buckling-based IR sensors. This approach allows the residual stress to be modulated, which ensures the sensor can be kept in the highly sensitive buckling regime. Furthermore, it prevents viscoelastic creep of the LbL membranes caused by the large deformations.

Under this dynamic regime, the buckling proved to be very stable. As mentioned, major issues in implementing buckling-based sensing are tailoring the residual stress to be near the critical buckling threshold and the small sensing ranges associated with the discrete behavior of buckling.²⁶⁴ We solve these problems by controlling the residual stress with our approach. Furthermore, the response times were extremely fast (figure 9.9). At 10.3 Hz, a little over 3 frames per a cycle, were recorded a clear sinusoidal signal that can be seen overlapping the primary sinusoidal signal, which occurs from temporal-aliasing caused by the sensor frequency being a non-integer multiple of the sampling frequency of the camera. Therefore, the fidelity of the intermediate stages of post-buckling deformation are captured in the data, thereby indicating the relatively high-quality of the optical transduction method. We were able to measure response times of 25 msec, by using the temporal aliasing signal.

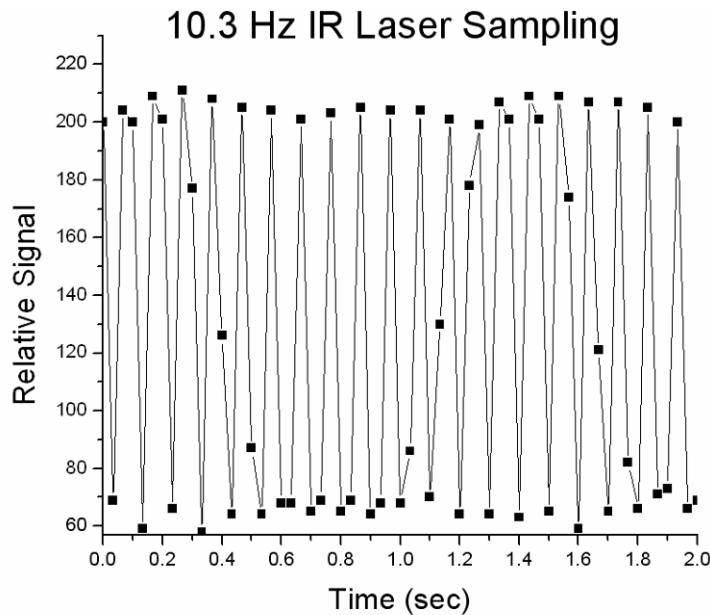


Figure 9.9: A plot of the relative optical amplitude vs. time operated under a laser frequency of 10Hz. Note the sinusoidal time aliasing caused by a difference between the optical camera sampling frequency and buckling frequency.

In order to investigate the performance of the IR sensors, they were exposed to IR light with a relatively slow frequency (0.56 Hz) and the thermo-electric cooler temperature was changed, thereby providing a measurable thermal signal. In this case the sensors were operated so that the laser power was relatively high and essentially saturated the un-buckling response and cooled enough to saturate the buckling deformation, thereby allowing the sensor to be sensitive in the region of the thermal cycle after the onset of buckling. Upon raising the temperature by 500 mK, from 17.00°C to 17.50°C, a significant damping in the optical signal was observed, specifically in the bottom part of the cyclic data corresponding to the buckling response (figure 9.10). Furthermore, the saturated un-buckling part of the thermal cycle was unaffected. The damping response is expected with heating and was shown to be quite repeatable. This damped response is induced because the Peltier temperature increase causes it to act as a less efficient heat sink, which offsets the minimum temperature of the thermal cycle. The unbuckling is unaffected because the relatively high laser power already unbuckles the membrane out of the sensitive region. The data was analyzed for phase shifts, which was inspired by the phasic sensing of the fire-beetle and their beating wings, but unfortunately the camera did not have enough temporal resolution to probe this, which samples at roughly 30 frames a second. Nonetheless, the amplitude response is still highly promising.

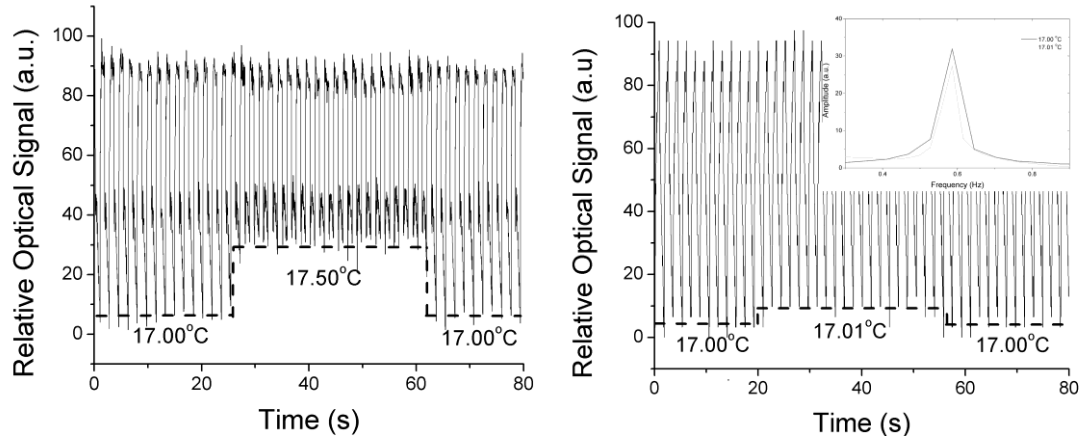


Figure 9.10: Left: A plot of relative optical signal vs. time. The temperature was raised by 500mK and then decreased. A dotted line at the bottom of the graph conveys the significant change in the amplitude due to the temperature change. Right: A plot of relative optical signal vs. time. The temperature was raised by 10mK and then returned. A dotted line at the bottom of the graph conveys the small, but noticeable change in amplitude due to the incredibly small temperature change. Inset: An FFT of the relative optical signal of the sensor before and after the 10mK temperature change, indicating a measurable damping of the amplitude of the buckling deflection caused by heating.

In order to better demonstrate the extremely sensitive nature of the thermal buckling sensors, the temperature difference was reduced to 10mK. Upon changing the temperature from 17.00°C to 17.01°C, a noticeable damping in the optical oscillation signal was observed again in the lower part of the thermal cycle (figure 9.10). The Fourier transform of the data also shows a noticeable difference in the amplitude at the probing frequency (figure 9.10, inset). The ability to resolve a 10mK difference is quite impressive considering that most commercial IR sensors have noise-equivalent temperature differences well exceeding 100mK. Even more impressive is that such sensitivity was obtained with sensors with such extremely small foot-prints of 15 μm ; which is about two orders of magnitude smaller than traditional membrane-based sensors.

9.4 Conclusion

Looking back to the fire beetles, the controversy regarding their signal transduction details is not surprising, especially considering that we started with thermal-pneumatic based sensing and found an overlapping thermal-expansion based mechanism. In fact, these results sparked the possibility that fire beetles in fact use both mechanisms simultaneously. Nonetheless, our exploration of these two different material-based transduction mechanisms, spurred by past biological research, serves as yet another example of the importance of both biologists and engineers in exploring biological ingenuity and implementing bio-inspired design. In doing so, we successfully demonstrated a new infrared sensing mechanism that proved to be highly sensitive, fast and capable of performing in a very small footprint.

CHAPTER 10

GENERAL CONCLUSIONS AND BROADER IMPACT

10.1 Summarized Specific Conclusions

In summary, spiders strongly rely on substrate vibrations for the guidance of prey capture, predator avoidance, and mating behaviour. These signals must be separated from the environmental noise. The most important vibration receptor organ in spiders is the metatarsal lyriform organ, which is relatively insensitive at frequencies below 30 Hz, but increasingly sensitive at higher frequencies. When deflected by vibrations the tarsus first transmits the stimulus to a soft material pad, which in turn passes it on to the metatarsal vibration sensor immediately behind it. The pad material was found to be highly viscoelastic with its highest compliance and high energy dissipation at frequencies below 30 Hz. At frequencies above 30 Hz the pad material quickly becomes stiffer, which allows better transmission of vibrations to the metatarsal lyriform organ. These properties of the pad material make it an ideal high-pass filter, which filters out environmental noise and makes the frequency range of vibrations relevant for the spider most effective. The signal processing abilities of the spider trichobothria, wind sensing receptors, were also investigated.

Work involved in examining the stiffness of wind-based receptors to probe the validity of fluid dynamics models and to probe the origin of high-pass response of previous nervous response measurements. The stiffness measurements did show time-dependant properties. The mechanical data was fit to an appropriate 3-parameter model.

Due to the complex structure of the hair receptors the exact origin of the time-dependant properties could not be conclusively determined. Although, it is likely that the nerve data is correlated to the mechanical behaviour, nonetheless the unexpected fruit really came from trying to interpret the biological data. Specifically, from this data it became apparent that passive polymers with T_g 's near room temperature can be used to sort mechanical data in a fairly complex way, including band-pass filtering. Signal absorption in biology was also investigated.

The investigation of material based signal absorbing structures in fish flow receptors was also a major focus of the work presented here. The bio-inspired concept of encapsulating MEMS haircell flow sensors in a semi-permeable, hydrogel cupulae, as employed by fish for underwater orientation, works very efficiently. The significant improvement of all of the characteristics of the hair flow sensor has been achieved after encapsulation with a hydrogel cupula. Applying the cupula-hair design demonstrated a significant decrease in the lower threshold limit of flow detection and the expansion of the dynamic range due to an efficient suppression of background noise within the viscous-damped cupula with the damping ability increasing for the low frequency noise due to the viscous shear strength characteristics of hydrogel networks. Moreover, the enhanced protection afforded by the hydrogel encapsulated hair flow sensors should enhance their ability to withstand high elastic deformation due to impact as well as provide anticorrosive and anti-biofouling properties to better withstand the marine environment.^{269,270}

After demonstrating the potential of the bio-inspired artificial cupula, the material was patterned into a bio-inspired higher aspect structure. We were able to improve upon our previous design, resulting in a drastically improved sensor. The improved sensor had

minimum threshold flow velocities as low as $2.5 \mu\text{m/s}$, which is extremely low as compared to current available sensors and even the biological analogue. The sensitivity was improved by almost 40 times with the addition of the high aspect ratio cupula. In fact, a velocity sensitivity threshold of $2.5 \mu\text{m/s}$ achieved here with the addition of high-aspect ratio hydrogel cupula to hair sensors are truly rivaling the performance of fish flow receptors.

To fully leverage the microfabricated flow sensors for flow based imaging, it is important to optimize the sensing abilities. Furthermore, it is critical to use an array of sensors, essentially creating the pixels for “flow based imaging”. This work demonstrated fabrication techniques to create structures aimed at accomplishing these two tasks. To enhance the microfabricated sensors abilities through the signal absorbing cupula, bio-inspired tall cupular fibrils were fabricated and arrays of cupula were patterned in various shapes. We expect further sensitivity gains from sensors encapsulated by tall cupula (3 times taller) supported by cupular fibrils. These taller cupula would enhance the signal absorption of the structure farther from the boundary layer and enhancing the cupula-hair coupling. Much like fish, we were able to create anisotropic cupula in arrays, which should help to enhance the directional sensing capabilities and will allow the bio-inspired cupula to be applied towards sensor arrays for imaging the environment via flow fields.

After studies involving signal absorption, transmission and signal processing, we focused efforts on signal transduction, specifically developing photo-thermal sensors from bio-inspired transduction strategies. Although, there is some debate as to the details of the thermal-pneumatic transduction mechanism, this work started by developing

implementing a thermal-pneumatic mechanism, by sealing cavities with an ultra-thin film. The film deflects in response to increased pressure (caused by heating of the gas in the cavity). While developing these sensors a unique buckling behavior was observed at temperature slightly below room temperature. Upon further investigations it was found that this buckling was induced due to the negative thermal expansion of the suspended film. Looking back to the fire beetles, the controversy regarding their signal transduction details is not surprising, especially considering that we started with thermal-pneumatic based sensing and found an overlapping thermal-expansion based mechanism. In fact, these results sparked the possibility that fire beetles in fact use both mechanisms simultaneously. Nonetheless, our exploration of these two different material-based transduction mechanisms, spurred by past biological research, serves as yet another example of the importance of both biologists and engineers in exploring biological ingenuity and implementing bio-inspired design. In doing so, we successfully demonstrated a new infrared sensing mechanism that proved to be highly sensitive, fast and capable of performing in a very small footprint.

10.2 General Conclusions

Sensing is the vital bridge that allows biology to interpret the surrounding ecology, which provides a large incentive to continually improve sensing capabilities. Biology has had extensive time to develop and apply functional materials to sensing applications, thereby providing a wealth of ingenuity for functional materials design waiting to be tapped. Bio-inspired design approach is gaining momentum because of

this limitless wealth of novel approaches, especially in regard to materials. The research presented in this dissertation serves as an example of the capabilities offered to material scientists and engineers who investigate and interpret biology's design. This dissertation presented research in the area of bio-inspired approaches to applying structured soft materials to sensing applications. Specifically, the work focused on fish-inspired micro-fabricated soft structures for enhancing underwater flow sensing, spider-inspired structures for enhancing air-flow monitoring, and insect-inspired photo-thermal transduction methods.

By studying fish and understanding that the hydrogel-like cupula was an important specialized structure that enhanced the neuromast's flow sensing ability, we were able to take a fruitful bio-inspired approach to develop an engineered cupula. Furthermore, by studying blind cave fish cupula we were able to replicate the material properties and shape of the fish bio-cupula, which led to dramatically enhanced flow sensing, endowing the engineered sensors with capabilities that rival that of fish.

Through studying spiders that were highly dependent on vibrations and air-flow, we were able to elucidate a material-based mechanical signal filtering mechanism. Furthermore, we worked with scientists at AFRL to develop a spider inspired two-tier hair sensor that has significantly enhanced the durability of the sensors and provides the ground-work for developing air-flow sensors capable of material-based signal filtering.

The sensing abilities of fire beetles provided motivation to improve thermal-pneumatic based sensors by using ultra-thin polymeric films. Work with the IR-sensing films naturally evolved into an exploration of thermal-stress induced buckling. The work

with the thermal-pneumatic and thermal-buckling transduction paralleled questions regarding the details of the fire-beetle's IR transduction.

From the work presented here, the synergistic relationship of understanding the novel approaches of biology and applying those approaches to engineered systems should be quite evident. Furthermore, this work demonstrated that dramatic improvements to engineered systems are accessible through understanding and utilizing relatively simple lessons offered by biology in the application of functional materials. The results presented in this dissertation clearly support the value that nature offers to material scientists looking for inspiration in the design of functional materials, especially for sensing applications.

10.3 Significance and Broader Impact

Inter-disciplinary work often acts to catalyze discovery and innovation by exposing different scientific communities to the methodologies, concepts, and knowledge of each other. This exposure is often mutually beneficial and constructive. The research presented in this dissertation is not an exception to this trend; in fact the work has been getting attention among these communities. While polymer scientists are very familiar with time-temperature superposition and viscoelasticity, biologists were quite surprised by this phenomenon. Fish sensory biologists, have cited our work in their recent studies and made considerable progress supporting the idea that the fish cupula not only functions in a signal absorbing role, but also in a signal filtering role. Nonetheless, it often requires significant effort to bridge these gaps. Furthermore, interpreting the functional role of biological systems and components can be quite a challenging task in

itself. The broad success of the research serves to build a strong foundation for interdisciplinary research in bio-inspired materials for functional roles sensing.

While it is well-known in the biological community that species often off-load signal processing via a variety of different strategies, the strategy presented in this dissertation regarding strain receptors in wandering spiders strongly supports the theory that passive materials can act in a functional role to depreciate signal processing loads, which can be crucial to species with simple nervous systems that heavily rely on their sensory information. The pad material acts as a high-pass filter by transmitting the mechanical stimuli through this time dependant material en-route to the receptor. In fact, it is quite possible that wandering spiders also use passive materials to filter mechanical stimuli to their wind-sensing trichobothria. In this case, the sensor structure is more complex and the location of the material is difficult to elucidate and therefore the role remains somewhat elusive without performing mechanical and nervous response measurements simultaneously.

Nonetheless, the process of deciphering the result's biological significance bore an unexpected fruit. Specifically, we realized that the use viscoelastic material was not limited to a high-pass filtering role, but in fact could be used as a low-pass filter, or even a band pass-filter, depending on the location of the material. Depending on whether the frequency stiffening component act to transmit mechanical energy or not determines whether the component will act in a high-pass or a low-pass role, respectively.

On the same note, if instead the time-responsive material were located at the site of strain reception, the material would also act as a low-pass filter. In other words, because the absorbed signal is stress (or force) and the signal transduction utilizes strain

(or deformation) the time-varying stiffness of the material has the ability to divert, absorb or focus mechanical information. This ubiquitous approach opens up many new applications for functional polymeric materials in MEMS. In fact a negative photo-resist with a very well-defined glass transition temperature (frequency) with exposure time would likely become a very important tool for the MEMS industry.

The investigations in photo-thermal-based sensing resulted in two different transduction principles from the same sensor system, thermal-pneumatic transduction and non-linear thermal buckling transduction. First, this work supports the importance of working directly with biology or at least well studied systems. The fire-beetle is not the most well studied specimen. Nonetheless, we explored two possible transduction principles that were fairly similar to the two common theories regarding the sensing mechanism of the fire beetle. In the engineered sensor the thermal-pneumatic mechanism was significantly less sensitive than the solid thermal expansion-based mechanism. Although, biological receptors are sensitive enough to measure the strains from the thermal expansion of a solid film, it still seems surprising because the thermal expansion of gases is much larger than solid films. Furthermore, the volumetric heat capacity of air is much less than polymers, which would support thermal-pneumatic as an efficient transduction principle. But, on the other hand, as our sensors demonstrated, materials are able to access non-linear deformation mechanisms, which can lead to very high sensitivities over smaller ranges. In order to properly use this unique transduction mechanism it is important to maintain the sensors in their sensitive range. In order to accomplish this we cooled the sensors and then dynamically heated them. These sensors had quite impressive threshold sensitivity within this sensitive range. In the future, non-

linear deformation mechanisms could likely lead to highly sensitive sensors. But much like the atomic force microscope, they will require a feedback loop to prevent them from drifting from their sensitive range.

The studies presented in this dissertation demonstrated the effectiveness of analyzing and understanding biology's use of functional materials. Through understanding functionality of biological materials, we were able to implement similar designs for engineered sensors, which truly demonstrated the capabilities of this approach. The work explored some of the boundaries of the subject and thereby provided a strong foundation for future scientific explorations of the subject.

10.4 Refereed Publications and Information Directly Related to this Dissertation

The underwater flow sensing research serves as a very strong example of the benefits that await scientists and engineers who stray from the comfort zone of their communities and immerse themselves in biological research in search of novel design principles. With over 20 highlights in over 20 journals, radio and TV including German NPR, Canadian Discovery Channel, ACS C&EN and Chemical Technology, this work has had the exposure to serve as strong support for bio-inspired functional materials. Furthermore, this research strongly supports the use of passive materials to enhance signal absorption.

1) **ME McConney**, KD Anderson, L Brott, RR Naik, VV Tsukruk, Bio-inspired Material Approaches to Sensing (2009) (Invited Feature Article Accepted to Advanced Functional Materials)

2) **ME McConney**, N Chen, D Lu, HA Hu, S Coombs, C Liu and VV Tsukruk. *Biologically inspired design of hydrogel-capped hair sensors for enhanced underwater flow detection* (2009) *Soft Matter* 5: 292 - 295

- 3) DR Denison, ME Knotts, **ME McConney**, VV Tsukruk. *Experimental Characterization of mm-wave detection by a micro-array of Golay cells* SPIE Defense Security + Sensing, Orlando, FL, April 13-17 2009 Paper 7309-18 of Conference 7309
- 4) **ME McConney**, CF Schaber MD Julian, WC Eberhardt, JAC Humphrey, Friedrich G. Barth, VV Tsukruk.. *Surface Force Spectroscopic Point Load Measurements and Viscoelastic Modelling of the Micromechanical Properties of Airflow Sensitive Hairs of a Spider (Cupiennius salei)* (2008) J. R. Soc. Interface (Available online: December 16, 2008)
- 5) KD Anderson, D Lu, **ME McConney**, T Han, D Reneker, VV Tsukruk. *Hydrogel microstructures combined with electrospun fibers and photopatterning for shape and modulus control* (2008) Polymer 49: 5284-5293
- 6) **ME McConney**, CF Schaber, MD Julian, FG Barth, and VV Tsukruk, *Viscoelastic nanoscale properties of cuticle contribute to the high-pass properties of spider vibration receptor (Cupiennius salei Keys)* (2007) J. R. Soc. Interface 4: 1135–1143 (Cover Story)
- 7) S Peleshanko, MD Julian, M Ornatska, **ME McConney**, MC LeMieux, N Chen, C Tucker, Y Yang, C Liu, JAC Humphrey, and VV Tsukruk. *Hydrogel-Encapsulated Microfabricated Haircells Mimicking Fish Cupula Neuromast* (2007) Adv. Mater. 19: 2903-2909
- 8) C Jiang, **ME McConney**, S Singamaneni, E Merrick, Y Chen, J Zhao, L Zhang, and VV Tsukruk. *Thermo-Optical Arrays of Flexible Nanoscale Nanomembranes Freely Suspended over Microfabricated Cavities as IR Microimagers* (2006) Chem. Mater. 18: 2632-2634

10.5 Other Relevant Publications

- 1) KD Anderson, JM Slocik, **ME McConney**, JO Enlow, R. Jakubiak, TJ Bunning, RR Naik, VV Tsukruk. *Facile Plasma Enhanced Deposition of Ultrathin Crosslinked Amino Acid Films for Conformal Biometallization* (2009) Small 5:741-749
- 2) JH He, S Singamaneni, CH Ho, Y. Lin, **ME McConney** and VV Tsukruk. *Thermal Sensor and Switch Based On Plasma Polymer/ZnO Suspended Nanobelt Bimorph Structure* (2009) Nanotechnology 20: 065502
- 3) S Singamaneni, **ME McConney**, MC LeMieux, H Jiang, JO Enlow, TJ Bunning, RR Naik, and VV Tsukruk. *Polymer–Silicon Flexible Structures for Fast Chemical Vapor Detection* (2007) Adv. Mater. 19: 4248-4255 (Inside Cover Story)
- 4) JH He, YH Lin, **ME McConney**, VV Tsukruk, and ZL Wang. *Enhancing UV photoconductivity of ZnO nanobelt by polyacrylonitrile functionalization* (2007) J. Appl. Phys. 102: 084303

- 5) Y Lin, **ME McConney**, M Lemieux, S Peleshanko, C Jiang, S Singamaneni, and V. Tsukruk. "Tri-layered Ceramic-Metal-Polymer Microcantilevers with Dramatically Enhanced Thermal Sensitivity, *Advanced Materials* (2006) *Adv. Mater.* 18: 1157-1161 ([Inside Cover Story](#))
- 6) M Lemieux, **ME McConney**, Y Lin, S Singamaneni, H Jiang, TJ Bunning, and VV Tsukruk. *Polymeric Nanolayers as Actuators for Ultrasensitive Thermal Bimorphs* (2006) *Nano Lett.* 6(4): 730-734 (DOI: 10.1021/nl0525305)
- 7) C Jiang, **ME McConney**, S Singamaneni, E Merrick, Y Chen, J Zhao, L Zhang, and VV Tsukruk. *Thermo-Optical Arrays of Flexible Nanoscale Nanomembranes Freely Suspended over Microfabricated Cavities as IR Microimagers* (2006) *Chem. Mater.* 18: 2632-2634

10.6 Oral Presentations Related to Dissertation

- 1) **ME McConney**, CF Schaber, MD Julian, J Humphrey, FG Barth, VV Tsukruk, , *Mechanical Signal Filtering by Viscoelastic Properties of Cuticle in a Wandering Spider*, American Physical Society, March Meeting, 2009
- 2) **M. E. McConney**, D. Lu, K. Anderson, S. Peleshanko, V. V. Tsukruk, *Sensing Structures Inspired by Blind Cave Fish*, American Physical Society, March Meeting, 2009
- 3) **ME McConney**, S Singamaneni, VV Tsukruk, *Thermally Sensitive Array of Nanoscale Polymeric Golay Cells*, 36th Annual North American Thermal Analysis Society Conference, 2008,
- 4) **ME McConney**, CF Schaber, MD Julian, FG Barth, VV Tsukruk. *Wandering Spiders use Viscoelastic Properties of Cuticle for Mechanical Signal Filtering*. Materials Research Society Meeting, Spring 2008
- 5) **ME McConney**, S Peleshanko, D Lu, K Anderson, VV Tsukruk. *Blind Cave Fish Inspired Novel Sensing Structures*. Materials Research Society Meeting, Spring 2008
- 6) **ME McConney**, CF Schaber, MD Julian, FG Barth, VV Tsukruk. *Characterization of Ultra-Sensitive Air Flow Receptors of live Wandering Spiders*. Materials Research Society Meeting, Fall 2006
- 7) **ME McConney**, M Ornatska, MC LeMieux, S. Coombs, VV Tsukruk. *Elastic Properties of Flow Sensing Structures in Blind Cave Fish*. Materials Research Society Meeting, Fall 2006

REFERENCES

- 1 Y. Bar-Cohen; in *Biomimetics: Biologically Inspired Technologies*, CRC Press, Boca Raton, FL 2006, pp.2-40.
- 2 S. Vogel; “Cat’s Paws and Catapults: Mechanical Worlds of Nature and People” W.W. Norton & Company Inc. New York, NY, 1998
- 3 T. Galante, J. Frank, J. Bernard, W. Chen, G. A. Lesieutre, G. H. Koopmann; “Design, Modeling, and Performance of a High Force Piezoelectric Inchworm Motor”. *J. Intel. Mat. Syst. Str.* 1999, 10, 962.
- 4 J. Hazel, M. Stone, M. S. Grace, and V. V. Tsukruk; “Nanoscale design of snake skin for reptation locomotions via friction anisotropy”. *J. Biomech.* 1999, 32, 477.
- 5 L. Mahadevan, S. Daniel, M. K. Chaudhury; “Biomimetic ratcheting motion of a soft, slender, sessile gel”. *P. Natl. Acad. Sci. USA*, 2004, 101, 23.
- 6 A. Woesz, J. C. Weaver, M. Kazanci, Y. Dauphin, D. E. Morse, J. Aizenberg, P. Fratzl; “Micromechanical properties of biological silica in skeletons of deep-sea sponges”. *J. Mater. Res.* 2006, 21, 2068
- 7 J. C. Weaver, J. Aizenberg, G. E. Fantner, D. Kisailus, A. Woesz, P. Allen, K. Fields, M. J. Porter, F. W. Zok, P. K. Hansma, P. Fratzl, D. E. Morse; “Hierarchical assembly of the siliceous skeletal lattice of the hexactinellid sponge *Euplectella aspergillum*”. *J. Struct. Biol.* 2007, 158, 93
- 8 J. Aizenberg; “Crystallization in Patterns: A Bio-Inspired Approach”. *Adv. Mater.* 2004, 16, 1295
- 9 K. Autumn, Y. A. Liang, S. T. Hsieth, W. Zesch, W. P. Chan, T. W. Kenny, R. Fearing, R. J. Full; “Adhesive force of a single gecko foot-hair”. *Nature* 2000, 405, 681
- 10 A. K. Geim, S. V., Dubonos, I. V. Griforievam K. S. Novoselov, A. A. Zhukov, and S. Y. Shapoval; “Microfabricated adhesive mimicking gecko foot-hair”. *Nat. Mater.* 2003, 2, 461
- 11 K. Autumn, M. Sitti, Y. A. Liang, A. M. Peattie, W. R. Hansen, S. Sponberg, T. W. Kenny, R. Fearing, J. N. Israelachvili, R. J. Full; “Evidence for van der Waals adhesion in gecko setae”. *P. Natl. Acad. Sci. USA* 2002, 99, 12252

-
- 12 S. Yang, J. Aizenberg; "Microlens arrays with integrated pores". *NanoToday* 2005, 12, 40.
 - 13 S. Yang, G. Chen, M. Megens, C. K. Ullal, Y.-J. Han, R. Rapaport, E. L. Thomas, J. Aizenberg; "Functional Biomimetic Microlens Arrays with Integrated Pores". *Adv. Mater.* 2005, 17, 435.
 - 14 H. Lee, Y. Lee, A. R. Statz, J. Rho, T. G. Park, and P. B. Messersmith; "Substrate Independent Layer-by-Layer Assembly by Using Mussel-Adhesive-Inspired Polymers". *Adv. Mater.* 2008, 20, 1619.
 - 15 H. Lee, S. M. Dellatore, W. M. Miller and P. B. Messersmith; "Mussel-Inspired Surface Chemistry for Multifunctional Coatings". *Science* 2007, 318, 426.
 - 16 Committee on Biomolecular Materials and Processes, National Research Council; "Inspired by Biology: From Molecules to Materials to Machines" The National Academies Press, Washington, D.C., 2008
 - 17 M. Frasca, P. Arena, L. Fortuna; "Bio-inspired Emergent Control of Locomotion Systems" World Scientific Publishing Company Pte. Ltd, Singapore, 2004
 - 18 L. Sheperd, T.G. Constandinou, C. Toumazou; "Towards Ultra-Low Power Bio-inspired Processing" In "Body Sensor Networks" ed.: G.-Z. Yang, Springer-Verlag, London, 2006, pp. 219-238
 - 19 D.R. Brooks; "Evolution as Entropy: Towards a Unified Theory of Biology" The University of Chicago Press, Chicago, 1988, pp. 1-30
 - 20 N.A. Cambell, J.B. Reece; "Biology 6th Ed." Pearson Education Inc., San Francisco, CA, 2002
 - 21 M. Hiagland, B. Dodson, J. Hauck; "Exploring the Way Life Works: The Science of Biology" Jones and Bartlett Press Inc., Sudbury, MA, 2001
 - 22 "Fundamentals of Modern Manufacturing: Materials, Processes and Systems" John Wiley & Sons Ltd., 2002
 - 23 W. Stebbins; "The Acoustic Sense of Animals" Harvard University Press, Cambridge MA, 1983.
 - 24 N.T. Nguyen; "Micromachined flow sensors-a review". *Flow Meas. Instrum* 1997, 8, 7.

-
- 25 R. Darby; "Chemical Engineering Fluid Dynamics". 2nd ed. Marcel Dekker. New York, 2001.
- 26 I.F. Akyildiz, D. Pompili, T. Melodia; "Underwater acoustic sensor networks: research challenges". *Ad Hoc Net.* 2005, 3, 257.
- 27 Y. Yang, J. Chen, J. Engel, S. Pandya, N. Chen, C. Tucker, S. Coombs, D.L. Jones, C. Liu; "Distant touch hydrodynamic imaging with an artificial lateral line". *PNAS* (2006) 103:18891-18895
- 28 B.R. Clayton, B.S Massey; "Flow visualization in water: a review of techniques". *J. Sci. Instrum.* 1967, 44, 2-10
- 29 P. Freymuth; "Flow visualization in fluid mechanics". *J. Sci. Instrum* (1993) 64: 1-18
- 30 S. Pandya, Y. Yang, D. Jones, J. Engel, C. Liu; *EURASIP Journal on Applied Signal Processing*, accepted.
- 31 N. Chen, J. Chen, J. Engel, S. Pandya, C. Tucker C. Liu; *The 12th Solid State Sensors, Actuator, and Microsystems Workshop* (Hilton Head 2006), Hilton Head Island, SC, June 4 - 8, 2006.
- 32 J. Chen, J. Engel, N. Chen, S. Pandya, S. Coombs, C. Liu; *MEMS 2006 Conference*, Istanbul, Turkey , January 22 - 26, 2006
- 33 Y. Yang, N. Chen, C. Tucker, J. Engel, S. Pandya, C. Liu; *MEMS 2007 20th IEEE International Conference on Micro Electro Mechanical Systems*, Kobe, Japan, January 21 -25, 2007
- 34 Jonathan Engel, Jack Chen, Chang Liu, and David Bullen, "Polyurethane Rubber All-Polymer Artificial Hair Cell Sensor", *IEEE/ASME Journal of MEMS*, 2006
- 35 N. Chen, C. Tucker, J.M. Engel, Y. Yang; S. Pandya, C. Liu; *J. MEMS*, 2007, 16, 999
- 36 Fan, Z., J. "Design and fabrication of artificial lateral line flow sensors" *Micromech. Microengin.*, 2002, 12, 655
- 37 S. Dijkgraaf. "The Functioning and Significance of the Lateral-line Organs". *Biol. Rev.* 1962, 38, 51.

-
- 38 E.S. Hassan in *The Mechanosensory Lateral Line: Neurobiology and Evolution*, eds. S. Coombs, P. Görner and H. Münz, Springer-Verlag, NY, 1989, pp.218-227
- 39 A.B.A. Kroese, J.M. Van der Zalm and J. Van der Berken, ““Frequency response of the lateral-line organ of *Xenopus laevis*”.” *Pflug. Arch. Eur. J. Phy.*, 1978, 375, 167
- 40 S. Coombs and J. Janssen, in *The Mechanosensory Lateral Line: Neurobiology and Evolution*, eds. S. Coombs, P. Görner and H. Münz, Springer-Verlag, NY, 1989, pp.299-319
- 41 G.G. Harris, W.A. van Bergeijk; “Frequency response of the lateral-line organ of *Xenopus laevis*”. *J. Acoust. Soc. Am.* 1962, 34, 1831
- 42 N. A. M. Schellart and R. J. Wubbels “The Auditory and Mechanosensory Lateral Line System” in *The Physiology of Fishes 2nd Edition*, ed. D. H. Evans, CRC Press LLC, NY, 1998, pp. 283-312
- 43 M.J. McHenry and S.M. van Netten; The flexural stiffness of superficial neuromasts in the zebrafish (*Danio rerio*) lateral line”. *J. Exp. Biol.*, 2007, 210, 4244-4253.
- 44 S. Coombs, S. M. van Netten; “The Hydrodynamics and Structural Mechanics of the Lateral Line System”. *Fish Physiol.* 2006, 23, 103.
- 45 Barth, F.G. and A. Schmid, eds. *Ecology of Sensing.* 2001, Springer: New York. 241.
- 46 A. Flock, A.J. Duvall; “The Ultrastructure of the Kinocilium of the sensory cells in the inner ear and lateral ear and lateral line organs”. *J. Cell Biol.* 1965, 25, 1
- 47 E. Perozo, A. Kloda, D.M. Cortes, B. Martinac; “Physical principles underlying the transduction of bilayer deformation forces during mechanosensitive channel gating”. *Nat. Struct. Biol.* 2002, 9, 696
- 48 A. Assad, D.P. Corey; “An active motor model for adaptation by vertebrate hair cells” *The Journal of Neuroscience* 1992, 12, 3291
- 49 J. Howard, W.M. Roberts, and A.J. Hudspeth; “Mechanoelectrical Transduction by Hair Cells”. *Ann. Rev. Biophys. Biophys. Chem.* 1988, 17, 99
- 50 R. Fettiplace, P. A. Fuchs; “Mechanisms of Hair Cell Tuning”. *Annu. Rev. Physiol.* 1999, 61, 809

-
- 51 L.G. Tilney, M.S. Tilney, D.J. DeRosier; "Actin Filaments, Stereocilia, and Hair Cells: How Cells Count and Measure". *Annu. Rev. Cell Biol.* 1992, 8, 257
- 52 R.A. Eatock; "Adaptation in Hair Cells". *Annu. Rev. Neurosci.* 2000, 23, 285
- 53 J.T. Corwin and M.E. Warchol; "Auditory Hair Cells: Structure, Function, Development, and Regeneration". *Annu. Rev. Neurosci.* 1991. 14, 301
- 54 V.S. Markin and A. J. Hudspeth; "Gating-Spring Models of Mechanoelectrical Transduction by Hair Cells of the Internal Ear". *Annu. Rev. Biophys. Biomol. Struct.* 1995, 24, 59
- 55 T. Teyke; "Morphological Differences in Neuromasts of the Blind Cave Fish *Astyanax hubbsi* and the Sighted River Fish *Astyanax mexicanus*". *Brain Behav. Evol.* 1990, 35, 23.
- 56 M. Denny; "The lateral-line system of the teleost, *Fundulus heteroclitus*". *J. Comp. Neurol.* 1937, 68, 39
- 57 J.P. Kelly, S.M. van Netten; "Topography and mechanics of the cupula in the fish lateral line. I. Variation of cupular structure and composition in three dimensions". *J. Morphol.* 1991, 207, 23.
- 58 F.G. Barth, *A Spider's World: Senses and Behavior.* 2002, New York: Springer-Verlag.
- 59 J.S. Rovner, F.G. Barth; "Vibratory Communication through Living Plants by a Tropical Wandering Spider". *Science* 1981, 214, 464
- 60 F.G. Barth; Neuroethology of the spider vibration sense, In: Barth, F.G. (ed) *Neurobiology of Arachnids* Springer, Berlin, 1985 pp. 203-229
- 61 F.G. Barth, Gethabali; "Spider vibration receptors: Threshold curves of individual slits in the metatarsal lyriform organ". *J. Comp. Physiol. A* 1982, 148, 175.
- 62 F.G. Barth, "How To Catch the Wind: Spider Hairs Specialized for Sensing the Movement of Air". *Naturwissenschaften*, 2000, 87, 51.
- 63 F.G. Barth, U. Wastl, J.A.C. Humphrey, R. Devarakonda; "Dynamics of Arthropod Filiform Hairs. II. Mechanical Properties of Spider Trichobothria (*Cupiennius salei* Keys.)". *Phil. Trans. Soc B.* 1993, 340, 445.

-
- 64 F.G. Barth; “Spider senses – technical perfection and biology”. *Zoology*, 2002. 105, 271.
- 65 F.G. Barth; “Spider mechanoreceptors”. *Curr. Opin. Neurobiol.*, 2004, 14, 415.
- 66 F.G. Barth, Sensors and Sensing: A Biologist's View, in *Sensors and Sensing in Biology and Engineering*, F.G. Barth, J.A.C. Humphrey, and T.W. Secomb, Editors. 2003, Springer Verlag: New York. p. 2-15
- 67 J.A.C. Humphrey, F.G. Barth, Medium Flow Sensing Hairs: Biomechanics and Models In: J. Casas, S.J. Simpson (Eds) *Advances in Insect Physiology Vol. 34 Insect Mechanics and Control*, Elsevier, Ltd. London, UK, 2008
- 68 A. Rogalski; *Infrared Detectors; Electrocomponent Science Monographs; Gordon and Breach Science Publishers: Amsterdam, Netherlands, 2000, Vol. 10*
- 69 *Handbook of Infrared Detection Technologies; Henini, M., Razeghi, M., Eds., Elsevier Science Ltd.: Oxford, UK 2002*
- 70 A. Rogalski; “Infrared detectors: status and trends”. *Prog. Quant. Electron.* 2003, 27, 59
- 71 E. Defay, C. Millon; “PZT thin films integration for the realisation of a high sensitivity pressure microsensor based on a vibrating membrane”. *Sensor Actuat. A.* 2002, 99, 64
- 72 Yamashita, K., A. Murata; “Miniaturized infrared sensor using silicon diaphragm based on Golay cell”. *Sensors Actuat. A* 1998, 66, 29.
- 73 J.-B. Chévrier, K. Baert, T. Slater; “An infrared pneumatic detector made by micromachining technology”. *J. Micromechanics and Microengineering* 1995, 5, 193.
- 74 W.G. Evans; “Infra-red Receptors in *Melanophila Acuminata* DeGeer” *Nature* 1964, 202, 211
- 75 W.G. Evans; “Perception of infrared from forest fires by *Melanophila Acuminata* DeGeer (Buprestidae, coleopteran)” *Ecology* 47, 1061
- 76 W. Gronenberg, H. Schmitz; “Afferent projections of infrared-sensitive sensilla in the beetle *Melanophila acuminata* (Coleoptera: Buprestidae)”. *Cell and Tissue Res.* 1999, 297, 311.

-
- 77 D.X. Hammer, D. Dave, T.E. Milner, B. Choi, H.G. Rylander, A.J. Welch; “Investigation of the transduction mechanism of infrared detection in *Melanophila acuminata*: photo-thermal–mechanical hypothesis”. *Comparative Biochemistry and Physiology A: Molecular and Integrative Physiology* 2002, 132, 381
- 78 H. Schmitz, H. Bleckmann; “The photomechanic infrared receptor for the detection of forest fires in the beetle *Melanophila acuminata* (Coleoptera: Buprestidae)” *Journal of Comparative Physiology A: Sensory Neural and Behavioral Physiology* 1998, 182, 647
- 79 Schmitz, H., Bleckmann, H.; “Fine structure and physiology of the infrared receptor of beetles of the genus *Melanophila* (Coleoptera: Buprestidae)”. *Int. J. Insect Morphol. & Embryol.* 1997, 26, 205
- 80 H. Schmitz, M. Murtz, H. Bleckmann; “Responses of the infrared sensilla of *Melanophila acuminata* (Coleoptera: Buprestidae) to monochromatic infrared stimulation”. *Journal J Comp Physiol A* 2000, 186, 543
- 81 H. Bleckmann, H. Schmitz, G. Von der Emde; “Nature as a model for technical sensors“. *J. Comp. Physiol. A* 2004, 190, 971
- 82 T. Vondran, K.-H. Apel, H. Schmitz; “The infrared receptor of *Melanophila acuminata* De Geer (Coleoptera: Buprestidae): ultrastructural study of a unique insect thermoreceptor and its possible descent from a hair mechanoreceptor”. *Tissue & Cell* 1995, 27, 645
- 83 A.L. Campbell, R.R. Naik, L. Sowards, M.O. Stone; “Biological infrared imaging and sensing” *Micron* 2002, 33, 211
- 84 W.G. Evans; “Infrared Radiation Sensors of *Melanophila acuminata* (Coleoptera: Buprestidae): A Thermopneumatic Model”. *Annals of the Entomological Society of America* 2005, 98, 738
- 85 D.X. Hammer H. Schmitz A. Schmitz, H. G. Rylander III, A.J. Welch; “Sensitivity threshold and response characteristics of infrared detection in the beetle *Melanophila acuminata* (Coleoptera: Buprestidae)”. *Comp. Biochem. Phys. A* 2001, 128, 805
- 86 R. Dudley, *The Biomechanics of Insect Flight: Form, Function, and Evolution.* Princeton University Press, 2000 Princeton, New Jersey
- 87 G. Binning, C.F. Quate, C.H. Gerber; “Atomic Force Microscope”. *Phys. Rev. Lett.* 1986, 56, 930

-
- 88 G. Binnig, H. Rohrer, C. H. Gerber, E. Weibel; "Tunneling through a controllable vacuum gap". *Appl. Phys. Lett.* 1982, 40, 178
- 89 G. Binnig, H. Rohrer, C.H. Gerber, E. Weibel; "Surface Studies by Scanning Tunneling Microscopy". *DF Phys. Rev. Lett.* 1982, 49, 57
- 90 G. Binnig, H. Rohrer; "Scanning tunneling microscopy—from birth to adolescence". *Rev. Mod. Phys.* 1987, 59, 615
- 91 Ch. Gerber, H. P. Lang; "How the doors to the nanoworld were opened". *Nat. Nanotechnol.* 2006, 1, 3
- 92 D.P.E. Smih; "Limits of force microscopy". *Rev. Sci. Instr.* 1995, 66, 3191
- 93 H.-J. Butt; B. Cappella, M. Kappl; "Force measurements with the atomic force microscope: Technique, interpretation and applications". *Surf. Sci. Rep.* 2005, 59, 1
- 94 B. Cappella, G. Dietler; "Force-distance curves by atomic force microscopy". *Surf. Sci. Rep.* 1999, 34, 1
- 95 J.P. Cleveland, S. Manne, D. Bocek, P.K. Hansma; "A nondestructive method for determining the spring constant of cantilevers for scanning force microscopy". *Rev. Sci. Instrum.* 1993, 64, 403.
- 96 J.E. Sader; "Parallel beam approximation for V-shaped atomic force microscope cantilevers". *Rev. Sci. Instrum.* 1995, 66, 4583.
- 97 J.L. Hazel, V.V. Tsukruk; "Spring constants of composite ceramic/gold cantilevers for scanning probe microscopy". *Thin Solid Films* 1999, 339, 249.
- 98 J. E. Sader, I. Larson, P. Mulvaney, L.R. White; "Method for the calibration of atomic force microscope cantilevers". *Rev. Sci. Instrum.* 1995, 66, 3789
- 99 C.T. Gibson, G.S. Watson, S. Myhra; "Determination of the spring constants of probes for force microscopy/spectroscopy". *Nanotechnology* 1996, 7, 259.
- 100 J.L. Hutter, J. Bechhoefer; "Calibration of atomic-force microscope tips". *Rev. Sci. Instrum.*, 1993, 64, 1868-1873.

-
- 102 G.A. Matei, E.J.Thoreson, J.R.Pratt, D.B. Newell, N.A. Burnham; "Precision and accuracy of thermal calibration of atomic force microscopy cantilevers". *Rev. Sci. Instrum.* 2006, 77, 083703-1-6
- 103 C.T. Gibson, D.A. Smith, C.J. Roberts, "Calibration of silicon atomic force microscope cantilevers". *Nanotechnology*, 2005, 16, 234
- 104 T. Machleidt, R. Kästner, K.-H. Franke; In *Nanoscale Calibration Standards and Methods: Dimensional and Related Measurements in Micro- and Nanometer Range*; Wilkening, G.; Koenders, L., Eds. Wiley-VCH: Weinheim, 2005; pp. 297-310
- 105 S. Czerkas, T. Dziomba, H. Bosse; In *Nanoscale Calibration Standards and Methods: Dimensional and Related Measurements in Micro- and Nanometer Range*; Wilkening, G.; Koenders, L., Eds. Wiley-VCH: Weinheim, 2005; pp. 311-320
- 106 C.M. Stafford, C. Harrison, K.L. Beers, A. Karim, E.J. Amis, M.R. Vanlandingham, H.-C.I. Kim, W. Volksen, R.D. Miller, E.E. Simony, "A buckling-based metrology for measuring the elastic moduli of polymeric thin films". *Nat. Mat.* 2004, 3, 545
- 107 S.A. Chizhik, Z. Huang, V.V. Gorbunov, N.K. Myshkin V.V. Tsukruk; "Micromechanical Properties of Elastic Polymeric Materials As Probed by Scanning Force Microscopy". *Langmuir* 1998, 14, 2606
- 108 O. Marti, S. Hild, In *Microstructure and Microtribology of Polymer Surface ACS Symposium Series 741*; Tsukruk, V.V.; Wahl, K., Eds.; ACS Publications,
- 109 J.P. Aimé, Z. Elkaakour, C. Odin, T. Bouhacina, D. Michel, J. Curely, A. Dautant; "Comments on the use of the force mode in atomic force microscopy for polymer films". *J. Appl. Phys.* 1994, 76, 754
- 110 J. Doshi, D.H. Reneker; "Electrospinning Process and Applications of Electrospun Fibers". *Journal of Electrostatics* 1995, 35, 151
- 111 D.H. Reneker, I. Chun; "Nanometre diameter fibres of polymer, produced by electrospinning". *Nanotechnology* 1996, 7, 216
- 112 Z.M. Huang, Y.Z. Zhang, M. Kotaki, S. Ramakrishna; "A review on polymer nanofibers by electrospinning and their applications in nanocomposites". *Composites Science and Technology* 2003, 63, 2223
- 113 D. Li, Y. Xia; "Electrospinning of Nanofibers: Reinventing the Wheel?". *Adv. Mater.* 2004, 16, 1151

-
- 114 G. Decher, J.D. Hong, J. Schmitt; "Buildup of ultrathin multilayer films by a self-assembly process: III. Consecutively alternating adsorption of anionic and cationic polyelectrolytes on charged surfaces". *Thin Solid Films* 1992, 210/211, 831
- 115 G. Decher; "Fuzzy Nanoassemblies: Toward Layered Polymeric Multicomposites". *Science* 1997, 277, 1232
- 116 S.T. Dubas, J.B. Schlenoff; "Factors Controlling the Growth of Polyelectrolyte Multilayers". *Macromolecules* 1999, 32, 8153
- 117 W. Chen, T.J. McCarthy Schmitt; "Layer-by-Layer Deposition: A Tool for Polymer Surface Modification". *Macromolecules* 1997, 30, 78
- 118 D. Zimnitsky, V.V. Shevchenko, V.V. Tsukruk; "Perforated, Freely Suspended Layer-by-Layer Nanoscale Membranes". *Langmuir* 2008, 24, 5996
- 119 M. Schonhoff; "Layered polyelectrolyte complexes: physics of formation and molecular properties". *Journal of Physics: Condensed Matter* 2003, 15, R1781
- 120 J.B. Schlenoff, S.T. Dubas; "Mechanism of Polyelectrolyte Multilayer Growth: Charge Overcompensation and Distribution". *Macromolecules* 2001, 34, 592
- 121 PT Hammond; "Recent explorations in electrostatic multilayer thin film assembly". *Current Opinion in Colloid & Interface Science* 2000, 4, 430
- 122 PT Hammond, "Form and Function in Multilayer Assembly: New Applications at the Nanoscale". *Adv. Mater.* 2004, 16, 1271
- 123 G.B. Sukhorukov, E. Donath, S. Davis, H. Lichtenfeld, F. Caruso, V.I. Popov, H. Mohwald; "Stepwise polyelectrolyte assembly on particle surfaces: a novel approach to colloid design". *Polym Adv Technol* 1998, 9, 759
- 124 M. Houska, E. Brynda, K. Bohata; "The effect of polyelectrolyte chain length on layer-by-layer protein/polyelectrolyte assembly—an experimental study". *Journal of Colloid and Interface Science* 2004, 273, 140
- 125 C. Jiang, V.V. Tsukruk; "Freestanding Nanostructures via Layer-by-Layer Assembly". *Adv. Mater.* 2006, 18, 829

-
- 126 Z. Tang, Y. Wang, P. Podsiadlo, N. Kotov; “Biomedical Applications of Layer-by-Layer Assembly: From Biomimetics to Tissue Engineering”. *Adv. Mater.* 2006, 18, 3203
- 127 Rovner, J. S. & Barth, F. G. “Vibratory Communication Through Living Plants by a Tropical Wandering Spider”. *Science* 1981, 214, 464.
- 128 Barth, F. G. 1985 Neuroethology of the spider vibration sense. In *Neurobiology of Arachnids* (ed. F. G. Barth), pp. 203–229. Berlin, Heidelberg, New York, Tokyo: Springer.
- 129 Barth, F. G. 2002 *A Spider’s world: senses and behavior*. Berlin, Heidelberg, New York: Springer.
- 130 Barth, F. G., Geethabali; “Spider vibration receptors. Threshold curves of individual slits in the metatarsal lyriform organ”. *J. Comp. Physiol. A* 1982, 148, 175.
- 131 Chen, X., Vlassak, J. J.; “Numerical study on the measurement of thin film mechanical properties by means of nanoindentation”. *J. Mater. Res.* 2001, 16, 2974.
- 132 Kovalev, A., Shulha, H., LeMieux, M., Myshkin, N. & Tsukruk V. V.; “Nanomechanical probing of layered nanoscale polymer films with atomic force microscopy”. *J. Mater. Res.* 2004, 19, 716.
- 133 Bliznyuk, V. N., Assender, H. E. & Briggs, G. A. D. “Surface Glass Transition Temperature of Amorphous Polymers. A New Insight with SFM”. *Macromolecules* 2002, 35, 6613.
- 134 Tsui, O. K. C., Wang, X. P., Ho, J. Y. L, Ng, T. K. & Xiao, X.; “Studying Surface Glass-to-Rubber Transition Using Atomic Force Microscopic Adhesion Measurements”. *Macromolecules* 2000, 33, 4198.
- 135 Kaliappan, S. N., Capella, B.; “Temperature dependent elastic–plastic behaviour of polystyrene studied using AFM force–distance curves”. *Polymer* 2005, 46, 11416.
- 136 Chaudhuri, O., Parekh S. H. & Fletcher, D. A.; “Reversible stress softening of actin networks”. *Nature* 2007, 445, 295.
- 137 Tsukruk, V. V. & Reneker, D. H.; “Scanning probe microscopy of organic and polymeric films: from self-assembled monolayers to composite multilayers”. *Polymer* 1995, 36, 1791.

-
- 138 Tsukruk, V. V.; "Scanning probe microscopy of polymer surfaces". *Rubber Chem. Technol.* 1997, 70, 430.
- 139 Tsukruk, V. V., Sidorenko, A., Gorbunov, V. V. & Chizhik, S. A.; "Surface Nanomechanical Properties of Polymer Nanocomposite Layers". *Langmuir* 2001, 17, 6715.
- 140 Gibson, C. T., Watson, G. S. & Myhra, S.; "Determination of the spring constants of probes for force microscopy/spectroscopy". *Nanotechnology* 1996, 7, 259.
- 141 Torii, A., Sasaki, M., Hane, K. & Okuma, S. "A method for determining the spring constant of cantilevers for atomic force microscopy". *Meas. Sci. Technol.* 1996, 7, 179.
- 142 Sviridenok, A. I., Chizhik, S. A. & Petrokovets, M. I. 1990 *Mechanics of a discrete friction contact*. Minsk: Nauki I Tekhnika.
- 143 Johnson, K. L., Kendall, K. & Roberts, A. D.; "Surface Energy and the Contact of Elastic Solids". *Proc. R. Soc. Lond. A* 1971, 324, 301.
- 144 Sneddon, I. N.; "The relation between load and penetration in the axisymmetric boussinesq problem for a punch of arbitrary profile". *Int. J. Eng. Sci.* 1965, 3, 47.
- 145 Leclere, P., Bredas, J. L., Moineau, G., Minet, M., Dubois, P., Jerome, R. & Lazzaroni, R.; In *Microstructure and microtribology of polymer surfaces* (ed. V. V. Tsukruk & K. J. Wahl), pp. 356–368. Washington D.C.: American Chemical Society.
- 146 Barth, F. G.; "Die Feinstruktur des Spinneninteguments". *Cell and Tissue Research* 1969, 97, 137.
- 147 Johnson, K. L. 1985 *Contact Mechanics*. Cambridge: Cambridge University Press.
- 148 Gingl, E., Burger A.-M. & Barth F. G.; "Intracellular recording from a spider vibration receptor". *J. Comp. Physiol. A* 2006, 192, 551.
- 149 LeMieux, M. C., Lin, Y. H., Cuong, P. D., Ahn, H. S., Zubarev, E. R. & Tsukruk, V. V.; "Microtribological and Nanomechanical Properties of Switchable Y-Shaped Amphiphilic Polymer Brushes". *Adv. Funct. Mater.* 2005, 15, 1529.
- 150 Sperling, L. H. *Polymeric multicomponent materials: an introduction*. John Wiley & Sons, Inc. New York, NY, 1997

-
- 151 Tsukruk, V. V., Gorbunov, V. V., Huang, Z. & Chizhik, S. “Dynamic microprobing of viscoelastic polymer properties”. *Polym. Int.* 2000, 49, 441
- 152 Barth, F. G. 1998 The vibrational sense of spiders. In *Comparative hearing: insects* (ed. R. R. Hoy, A. N. Popper & R. R. Fay), pp. 228–278. New York et al.: Springer.
- 153 Barth, F. G., Bleckmann, H. Bohnenberger, J. & Seyfarth E.-A. “Spiders of the genus *Cupiennius* Simon 1891 (Araneae, Ctenidae)”. *Oecologia* 1988, 77, 194.
- 154 Barth, F. G., Seyfarth, E.-A., Bleckmann, H. & Schüch, W. 1988 Spiders of the genus *Cupiennius* Simon 1891 (Araneae, Ctenidae) I. Range distribution, dwelling plants, and climatic characteristics of the habitats. *Oecologia* 1988, 77, 187.
- 155 Barth, F. G. 2000. “How To Catch the Wind: Spider Hairs Specialized for Sensing the Movement of Air”. *Naturwissenschaften* 87, 51.
- 156 Humphrey, J. A. C. & Barth, F. G. 2008 Medium flow-sensing hairs: biomechanics and models. In *Insect mechanics and control. Advances in insect physiology* 34 (eds J. Casas & S. J. Simpson), pp. 1–80. Amsterdam: Elsevier.
- 157 Barth, F. G., Wastl, U., Humphrey, J. A. C. & Devarakonda, R. “Dynamics of Arthropod Filiform Hairs. II. Mechanical Properties of Spider Trichobothria (*Cupiennius salei* Keys.)”. *Phil. Trans. R. Soc. Lond. B* 1993, 340, 445.
- 158 Bathellier, B., Barth, F. G., Albert, J. T. & Humphrey, J. A. C. “Viscosity-mediated motion coupling between pairs of trichobothria on the leg of the spider *Cupiennius salei*”. *J. Comp. Physiol. A* 2005, 191, 733.
- 159 Humphrey, J. A. C., Devarakonda, R., Iglesias, I. & Barth, F. G. “Dynamics of Arthropod Filiform Hairs. I. Mathematical Modelling of the Hair and Air Motions”. *Phil. Trans. R. Soc. Lond. B* 1993, 340, 423.
- 160 Humphrey J. A. C., Devarakonda, R., Iglesias, I. & Barth, F. G. “Errata re. Humphrey et al. 1993”. *Phil. Trans. R. Soc. Lond. B* 352, 1995.
- 161 Humphrey, J. A. C., Barth, F. G. & Voss, K. 2001 The motion-sensing hairs of arthropods: using physics to understand sensory ecology and adaptive evolution. In *The Ecology of Sensing* (eds F. G. Barth & A. Schmid) pp. 105–125. Berlin, Heidelberg, New York: Springer.

-
- 162 Humphrey, J. A. C., Barth, F. G., Reed, M. & Spak, A. In *Sensors and sensing in biology and engineering* (eds F. G. Barth, J. A. C. Humphrey & T. W. Secomb), pp. 129–144. 2003 Wien, New York: Springer.
- 163 Devarakonda, R., Barth, F. G. & Humphrey, J. A. C. “Dynamics of Arthropod Filiform Hairs. IV. Hair Motion in Air and Water”. *Phil. Trans. R. Soc. Lond. B* 1996, 351, 933.
- 164 Tsukruk, V. V., Gorbunov, V. V., Huang, Z. & Chizhik, S. A.; “Dynamic microprobing of viscoelastic polymer properties”. *Polymer International* 2000, 49, 441–444.
- 165 Fuchigami, N., Hazel, J., Gorbunov, V. V., Stone, M., Grace, M. S. & Tsukruk, V. V. “Biological Thermal Detection in Infrared Imaging Snakes. 1. Ultramicrostructure of Pit Receptor Organs”. *Biomacromolecules* 2001, 2, 757.
- 166 Gorbunov, V., Fuchigami, N., Stone, M., Grace, M. & Tskukruk, V. V. “Biological thermal detection: micromechanical and microthermal properties of biological infrared receptors”. *Biomacromolecules* 2002, 3, 106–115.
- 167 McConney, M. E., Schaber, C. F., Julian, M. D., Barth, F. G. & Tsukruk, V. V.; “Viscoelastic nanoscale properties of cuticle contribute to the high-pass properties of spider vibration receptor (*Cupiennius salei* Keys)”. *J R Soc Interface* 2007, 4, 1135.
- 168 Peleshanko, S., Julian, M. D., Ornatska, M., McConney, M. E., LeMieux, M. C., Chen, N., Tucker, C., Yang, Y., Liu, C., Humphrey, J. A. C. & Tsukruk, V. V.; “Hydrogel-Encapsulated Microfabricated Haircells Mimicking Fish Cupula Neuromast”. *Adv. Mater.* 2007, 19, 2903.
- 169 Cappella, B. & Dietler, G.; “Force-distance curves by atomic force microscopy”. *Surf. Sci. Report.* 1999, 34, 1.
- 170 LeMieux, M., Usov, D., Minko, S., Stamm, M., Shulha, H. & Tsukruk, V. V.; “Reorganization of Binary Polymer Brushes: Reversible Switching of Surface Microstructures and Nanomechanical Properties”. *Macromolecules* 2003, 36, 7244.
- 171 Kovalev, A., Shulha, H., LeMieux, M., Myshkin, N. & Tsukruk, V. V.; “”. *J. Materials Res.* 2004, 19, 716.
- 172 Hutter, J. L. & Bechhoefer, “Calibration of atomic-force microscope tips”. *J.; Rev. Sci. Instrum.* 1993, 64, 1868.

-
- 173 Hutter, J. L. & Bechhoefer, "Erratum: ``Calibration of atomic-force microscope tips" [Rev. Sci. Instrum. 64, 1868 (1993)]".J.; Rev. Sci. Instrum. 1993 64, 3342.
- 174 Hazel, J. L. & Tsukruk, V. V.; "Friction Force Microscopy Measurements: Normal and Torsional Spring Constants for V-Shaped Cantilevers".J. Tribol. 1998, 120, 814.
- 175 Hazel, J. L. & Tsukruk, V. V.; "Spring constants of composite ceramic/gold cantilevers for scanning probe microscopy".Thin Solid Films 1999, 339, 249.
- 176 Tsukruk, V. V., Huang, Z., Chizhik, S. A. & Gorbunov, V. V.; "Probing of Micromechanical Properties of Compliant Polymeric Materials".J. Materials. Sci. 1998, 33, 4905–4909.
- 177 Flügge, W. 1967 Viscoelasticity. Waltham, MA: Blaisdell Publishing Company.
- 178 Fung, Y. C. 1993 Biomechanics, 2nd edn. New York: Springer.
- 179 Barth, F. G.; "Die Feinstruktur des Spinneninteguments". Cell and Tissue Research 1969, 97, 137.
- 180 Blickhan, R. & Barth, F. G.; "Strains in the exoskeleton of spiders".J. Comp. Physiol. A 1985, 157, 115.
- 181 Barth, F. G. & Höller, A.; "Dynamics of arthropod filiform hairs. V. The response of spider trichobothria to natural stimuli".Phil. Trans. R. Soc. Lond. B 1999, 354, 183.
- 182 Shimozawa, T., Kumagai, T. Baba, Y.; "Structural scaling and functional design of the cercal wind-receptor hairs of cricket".J Comp Physiol A 1998, 183, 171.
- 183 Shimozawa, T., Murakami, J. & Kumagai, T. Sensors and sensing in biology and engineering (eds F. G. Barth, J. A. C. Humphrey & T. W. Secomb), pp. 145–157. 2003, Wien, New York: Springer.
- 184 Shimozawa, T. & Kanou, M.; "The aerodynamics and sensory physiology of range fractionation in the cercal filiform sensilla of the cricket *Gryllus bimaculatus*".J Comp Physiol A 1984, 155, 495.
- 185 Shimozawa, T. & Kanou, M. "Varieties of filiform hairs: range fractionation by sensory afferents and cercal interneurons of a cricket".J Comp Physiol A 1984, 155, 485.

-
- 186 Casas, J., Steinmann, T. & Dangles, O.; “The Aerodynamic Signature of Running Spiders”. PLoS ONE 2008, 3, e2116.
- 187 Findley, W. N., Lai, J. S. & Onaran, K. 1976 Creep and relaxation of non-linear viscoelastic materials. New York: Dover Publications.
- 188 Wineman, A. & Shaw, “influence of thermally induced chemorheological changes on the torsion of elastomeric circular cylinderS”. J. Continuum Mech. Thermodyn. 2006, 17, 477.
- 189 Gosline, J., Lillie, M., Carrington, E., Guerette, P., Ortlepp, C. & Savage, K. “Elastic proteins: biological roles and mechanical properties”. Phil. Trans. R. Soc. Lond. B 2002, 357, 121.
- 190 Anton, S.; Dissertation, Universität Wien. 1991
- 191 Barth, F. G., Humphrey, J. A. C., Wastl, U., Halbritter, J. & Brittinger, W.; “Dynamics of Arthropod Filiform Hairs. III. Flow Patterns Related to Air Movement Detection in a Spider (*Cupiennius salei* KEYS.)”. Phil. Trans. R. Soc. Lond. B 1995, 347, 397.
- 192 Klopsch, C., Barth, F. G. & Humphrey, J. A. C. In Fifth international symposium on turbulence and shear flow phenomena (eds R. Friedrich, N. A. Adams, J. K. Eaton, J. A. C. Humphrey, N. Kasagi & M. A. Leschziner), pp. 1023–1028. 2007, Garching, TU München.
- 193 F. G. Barth, A Spider' s World: Senses and Behavior, Springer-Verlag, New York, 2002.
- 194 Infrared Receptors and the Trigeminal Sensory System, (Eds.: S. Terashima, R. C. Goris), Harwood Academic Publishers, 1999.
- 195 G. Dehnhardt, B. Mauck, H. Bleckmann, “Seal whiskers detect water movements”. Nature 1998, 394, 235.
- 196 S. Coombs, J. Montgomery, “Fibers Innervating Different Parts of the Lateral Line System of an Antarctic Notothenioid, *Trematomus bernacchii*, Have Similar Frequency Responses, Despite Large Variation in the Peripheral Morphology.”. Brain, Behav. Evol. 1992, 40, 217.
- 197 M. Schrope, “Whale deaths caused by US Navy's sonar”. Nature 2002, 415, 106.

-
- 198 T. Teyke, "Morphological Differences in Neuromasts of the Blind Cave Fish *Astyanax hubbsi* and the Sighted River Fish *Astyanax mexicanus*". *Brain, Behav. Evol.* 1990, 35, 23.
- 199 S. M. van Netten, K. K. Karlsson, S. M. Khanna, A. Flock, "Effects of quinine on the mechanical frequency response of the cupula in the fish lateral line". *Hear. Res.* 1994, 73, 223.
- 200 N. Chen, J. Chen, J. Engel, S. Pandya, C. Tucker, C. Liu, in Proceedings of the 12th Solid State Sensors, Actuator, and Microsystems Workshop, Hilton Head, SC 2006.
- 201 S. Peleshanko, M. D. Julian, M. Ornatska, M. E. McConney, M. C. LeMieux, N. Chen, C. Tucker, Y. Yang, C. Liu, J. A. C. Humphrey, V. V. Tsukruk, "Hydrogel-Encapsulated Microfabricated Haircells Mimicking Fish Cupula Neuromast". *Adv. Mater.* 2007, 19, 2903.
- 202 S. A. Chizhik, Z. Huang, V. V. Gorbunov, N. K. Myshkin, V. V. Tsukruk, "Micromechanical Properties of Elastic Polymeric Materials As Probed by Scanning Force Microscopy". *Langmuir* 1998, 14, 2606.
- 203 V. V. Tsukruk, Z. Huang, "Micro-thermomechanical properties of heterogeneous polymer films". *Polymer* 2000, 41, 5541.
- 204 V. V. Tsukruk, A. Sidorenko, V. V. Gorbunov, S. A. Chizhik, "Surface Nanomechanical Properties of Polymer Nanocomposite Layers". *Langmuir* 2001, 17, 6715.
- 205 V. V. Tsukruk, V. V. Gorbunov, Z. Huang, S. A. Chizhik, "Dynamic microprobing of viscoelastic polymer properties". *Polymer Intern.* 2000, 49, 441.
- 206 V. V. Tsukruk, Z. Huang, S. A. Chizhik, V. V. Gorbunov, "Probing of Micromechanical Properties of Compliant Polymeric Materials". *J. Mater. Sci.*, 1998, 33, 4905.
- 207 V. S. Sukumar, S. T. Lopina, "Network Model for the Swelling Properties of End-Linked Linear and Star Poly(ethylene oxide) Hydrogels". *Macromolecules* 2002, 35, 10189.
- 208 L. D. Landau, E. M. Lifshitz, *Fluid Mechanics*, Pergamon Press, Oxford, 1959.

-
- 209 W. W. Graessley, *Polymeric Liquids and Networks: Structure and Properties*, Garland Science, New York, N. Y., 2003.
- 210 P. G. De Gennes, *Scaling Concepts in Polymer Physics*, Cornell University Press, Ithaca, NY, 1979.
- 211 J. N. Israelachvili, *Intermolecular and Surface Forces: With Applications to Colloidal and Biological Systems*, Academic Press, London, UK, 1985.
- 212 J. D. Ferry, *Viscoelastic Properties of Polymers*, Wiley-Intersciences, New York, NY, 1970.
- 213 R. Tharmann, M. M. Claessens, A. R. Bausch, "Viscoelasticity of Isotropically Cross-Linked Actin Networks". *Phys. Rev. Lett.* 2007, 98, 088103.
- 214 N. Wisniewski, M. Reichert, "Methods for reducing biosensor membrane biofouling". *Coll. Surf. B: Biointerf.* 2000, 18, 197.
- 215 S. Sharma, K. C. Papat, T. A. Desai, in *Handbook of Nanostructured Biomaterials and Their Applications in Nanobiotechnology*, 2005, 2, 299.
- 216 A.B.A. Kroese, J.M. Van der Zalm and J. Van der Berken, "Frequency response of the lateral-line organ of *Xenopus laevis*". *Pflug. Arch. Eur. J. Phy.*, 1978, 375, 167
- 217 S. Coombs and J. Janssen, in *The Mechanosensory Lateral Line: Neurobiology and Evolution*, eds. S. Coombs, P. Görner and H. Münz, Springer-Verlag, NY, 1989, pp.299-319
- 218 S. Coombs and J.C. Montgomery, In *Comparative Hearing: Fishes and Amphibians*, eds. A.N. Popper and R.R.Fay, Springer-Verlag, New York, 1st edn., 1999, vol. 11, pp. 319-362.
- 219 S. Coombs, "Smart Skins: Information Processing by Lateral Line Flow Sensors". *Auton. Robot.*, 2001, 11, 255.
- 220 T. Teyke, J. "Collision with and avoidance of obstacles by blind cave fish *Anoptichthys jordani* (Characidae)". *Comp. Physiol. A*, 1985, 157, 837.
- 221 E. Hassan, "On the discrimination of spatial intervals by the blind cave fish (*Anoptichthys jordani*)". *J. Comp. Physiol. A*, 1986, 159, 701.

-
- 222 M.J. McHenry and S.M. van Netten, "The flexural stiffness of superficial neuromasts in the zebrafish (*Danio rerio*) lateral line". *J. Exp. Biol.*, 2007, 210, 4244.
- 223 C. Liu, "Micromachined biomimetic artificial haircell sensors". *Bioinsp. Biomim.*, 2007, 2, S162.
- 224 J.C. Montgomery, C.F. Baker and A.G. Carton, "The lateral line can mediate rheotaxis in fish". *Nature*, 1997, 389, 960
- 225 Reneker DH, Chun I. "Nanometre diameter fibres of polymer, produced by electrospinning". *Nanotechnology* 1996, 7, 216
- 226 Frenot A, Chronakis I.S. "Polymer nanofibers assembled by electrospinning". *Curr Opin Colloid* 2003, 8, 64
- 227 Deitzel JM, Kleinmeyer JD, Hirvonen JK, Beck Tan NC., "Controlled deposition of electrospun poly(ethylene oxide) fibers". *Polymer* 2001, 42, 8163.
- 228 Reneker DH, Kataphinan W, Theron A, Zussman E, Yarin AL. "Nanofiber garlands of polycaprolactone by electrospinning". *Polymer* 2002, 43, 6785.
- 229 J. Doshi, D. H. Reneker, "Electrospinning process and applications of electrospun fibers". *Journal of Electrostat.* 1995, 35, 151.
- 230 Z. M. Huang, Y. Z. Zhang, M. Kotaki, S. Ramakrishna, "A review on polymer nanofibers by electrospinning and their applications in nanocomposites". *Compos. Sci. Technol.* 2003, 63, 223.
- 231 D. Li, Y. Xia, "Electrospinning of Nanofibers: Reinventing the Wheel?". *Adv. Mater.* 2004, 16, 1151.
- 232 A. Rogalski, "Infrared detectors: status and trends". *Prog. Quant. Electron.* 2003, 27, 59.
- 233 A. Rogalski, *Infrared Detectors-Electrocomponent Science Monographs Vol. 10*, Gordon and Breach Scientific Publishers, Amsterdam, 2000.
- 234 W. G. Evans, "Infra-red Receptors in *Melanophila acuminata* DeGeer". *Nature* 1964, 202, 211.
- 235 W. G. Evans, "Perception of infrared radiation from forest fires". *Ecology* 1966, 47, 1061.

-
- 236 W. Gronenberg, H. Schmitz, "Afferent projections of infrared-sensitive sensilla in the beetle *Melanophila acuminata* (Coleoptera: Buprestidae)". *Cell Tissue Res.* 1999, 297, 311.
- 237 D. X. Hammer, D. Dave, T. E. Milner, B. Choi, H. G. Rylander, A. J. Welch, "Investigation of the transduction mechanism of infrared detection in *Melanophila acuminata*: photo-thermal-mechanical hypothesis". *Comp. Biochem. Phys. A.* 2002, 132, 381.
- 238 H. Schmitz, H. Bleckmann, "The photomechanic infrared receptor for the detection of forest fires in the beetle *Melanophila acuminata* (Coleoptera: Buprestidae)". *J. Comp. Physiol. A.* 1998, 182, 647.
- 239 H. Schmitz, H. Bleckmann, "Fine structure and physiology of the infrared receptor of beetles of the genus *Melanophila* (Coleoptera: Buprestidae)". *Int. J. Insect Morphol. & Embryol.* 1997, 26, 205.
- 240 H. Schmitz, M. Murtz, H. Bleckmann, "Responses of the infrared sensilla of *Melanophila acuminata* (Coleoptera: Buprestidae) to monochromatic infrared stimulation". *J. Comp. Physiol. A.* 2000, 186, 543.
- 241 T. Vondran, K.-H. Apel, H. Schmitz, "The infrared receptor of *Melanophila acuminata* De Geer (Coleoptera: Buprestidae): ultrastructural study of a unique insect thermoreceptor and its possible descent from a hair mechanoreceptor". *Tissue & Cell* 1995, 27, 645.
- 242 J. Hazel, N. Fuchigami, V. Gorbunov, H. Schmitz, M. Stone, V. V. Tsukruk, "Ultramicrostructure and Microthermomechanics of Biological IR Detectors: Materials Properties from a Biomimetic Perspective". *Biomacromolecules* 2001, 2, 304.
- 243 H. Bleckmann, H. Schmitz, G. Von der Emde, "Nature as a model for technical sensors". *J. Comp. Physiol. A* 2004, 190, 971.
- 244 J. Cho, K. Char, J.D. Hong, K.B. Lee; "Fabrication of Highly Ordered Multilayer Films Using a Spin Self-Assembly Method". *Adv. Mater.* 2001, 13, 1076.
- 245 Jiang, C., S. Markutsya, V.V. Tsukruk; "Compliant, Robust, and Truly Nanoscale Free-Standing Multilayer Films Fabricated Using Spin-Assisted Layer-by-Layer Assembly". *Adv. Mater.* 2004, 16, 157.

-
- 246 Jiang, C., S. Markutsya, and V.V. Tsukruk; “Collective and Individual Plasmon Resonances in Nanoparticle Films Obtained by Spin-Assisted Layer-by-Layer Assembly”. *Langmuir* 2004, 20, 882.
- 247 K.-t. Wan, K. Liao; “Measuring mechanical properties of thin flexible films by a shaft-loaded blister test”. *Thin Solid Films*, 1999, 352: 167
- 248 S. Jayaraman, R.L. Edwards, K.J. Hemker; “Relating mechanical testing and microstructural features of polysilicon thin films”. *J Mater Res* 1999, 14, 688
- 249 S. Markutsya, C. Jiang, Y. Pikus, V.V. Tsukruk, “”. *Adv Mater* 2005, 15, 771
- 250 S. Timoshenko, “Theory of Plates and Shells, 2nd Ed.” McGraw-Hill Book Company, New York, 1959
- 251 C. Poilane, P. Delobelle, C. Lexcellent S. Hayashi, H. Tobushi; “Analysis of the mechanical behavior of shape memory polymer membranes by nanoindentation, bulging and point membrane deflection tests”. *Thin Solid Films* 2000, 370, 156.
- 252 M.J.E. Golay, “Theoretical Consideration in Heat and Infra-Red Detection, with Particular Reference to the Pneumatic Detector”. *Rev. Sci. Instrum.* 1947, 18, 347.
- 253 C. Jiang, S. Markutsya, Y. Pikus, V. V. Tsukruk, “Freely suspended nanocomposite membranes as highly sensitive sensors”. *Nature Mater.* 2004, 3, 721.
- 254 C. Jiang, B. M. Rybak, S. Markutsya, P. E. Kladitis, V. V. Tsukruk, “Self-recovery of stressed nanomembranes”. *Appl. Phys. Lett.* 2005, 86, 121912.
- 255 C. Jiang, M. E. McConney, S. Singamaneni, E. Merrick, Y. Chen, J. Zhao, L. Zhang, V. V. Tsukruk, “Thermo-Optical Arrays of Flexible Nanoscale Nanomembranes Freely Suspended over Microfabricated Cavities as IR Microimagers”. *Chem. Mater.* 2006, 18, 2632.
- 256 K. Yamashita, A. Murata, M. Okuyama, “Miniaturized infrared sensor using silicon diaphragm based on Golay cell”. *Sens. Actuators A* 1998, 66, 29.
- 257 S. Singamaneni, M. C. LeMieux, H. P. Lang, C. Gerber, Y. Lam, S. Zauscher, P. G. Datskos, N. V. Lavrik, H. Jiang, R. R. Naik, T. J. Bunning, V. V. Tsukruk, “Bimaterial Microcantilevers as a Hybrid Sensing Platform”. *Adv. Mater.* 2008, 20, 653.

-
- 258 H. M. James, E. Guth, "Theory of the Elastic Properties of Rubber". *J. Chem. Phys.* 1943, 11, 455.
- 259 R. H. Baughman, "Negative thermal expansion in crystalline linear polymers". *J. Chem. Phys.* 1973, 58, 2976.
- 260 S. Singamaneni, M. C. LeMieux, H. Jiang, T. J. Bunning, V. V. Tsukruk, "Negative Thermal Expansion in Ultrathin Plasma Polymerized Films". *Chem. Mater.* 2007, 19, 129.
- 261 N. Bowden, S. Brittain, A. G. Evans, J. W. Hutchinson, G. M. Whitesides; "Spontaneous formation of ordered structures in thin films of metals supported on an elastomeric polymer". *Nature* 1998, 393, 146.
- 262 C. Jiang, S. Singamaneni, E. Merrick, V. V. Tsukruk; "Complex Buckling Instability Patterns of Nanomembranes with Encapsulated Gold Nanoparticle Arrays". *Nanolett.* 2006, 6, 2254.
- 263 C. M. Stafford, C. Harrison, K. L. Beers, A. Karim, E. J. Amis, M. R. Vanlandingham, H. Kim, W. Volksen, R. D. Miller, E. E. Simonyi, "A buckling-based metrology for measuring the elastic moduli of polymeric thin films". *Nat. Mater.* 2004, 3, 545.
- 264 M. R. Begley, M. Utz, U. Komaragiri, "Chemo-mechanical interactions between adsorbed molecules and thin elastic films". *J. Mech. Phys. Solids* 2005, 53, 2119.
- 265 M. Utz, M. R. Begley, "Scaling theory of adsorption-induced stresses in polymer brushes grafted onto compliant structures". *J. Mech. Phys. Solids* 2008, 56, 801.
- 266 M. R. Begley, N. S. Barker, "Analysis and design of kinked (bent) beam sensors". *J. Micromech. Microeng.* 2007, 17, 350.
- 267 M. R. Begley, M. Utz, "Multiscale Modeling of Adsorbed Molecules on Freestanding Microfabricated Structures". *J. Appl. Mech.* 2008, 75, 021008.
- 268 A. Ettouhami, A. Essaid, N. Ouakrim, L. Michel, M. Limouri, "Thermal buckling of silicon capacitive pressure sensor". *Sens. Actuators A* 1996, 57, 167.
- 269 N. Wisniewski, M. Reichert, "Methods for reducing biosensor membrane biofouling". *Coll. Surf. B: Biointerf.* 2000, 18, 197.

270 S. Sharma, K. C. Papat, T. A. Desai, in Handbook of Nanostructured Biomaterials and Their Applications in Nanobiotechnology, 2005, 2, 299-321.

VITA

MICHAEL E. MCCONNEY

Michael Edward McConney was born to Ruth Monica Stedman and Charles Edward McConney on December 1, 1980. He and his sister, Catherine Elizabeth McConney, grew up in Los Angeles, California. He attended Mar Vista Elementary for first grade. Then he went to St. Martin of Tours for grades 2-8. For High School he left Los Angeles, attending Westtown School, a Quaker co-ed boarding school in Pennsylvania. Graduating High School in 1999, he then moved to Iowa City, Iowa to pursue undergraduate studies at the University of Iowa. Michael met his future wife, Stephanie Leone Mann, at the University of Iowa. He obtained a Bachelor of Science and Engineering in Chemical Engineering from the University of Iowa in 2004. He started his graduate studies in the summer of 2004 with Professor Vladimir Tsukruk at the Materials Science and Engineering department at Iowa State University. Stephanie was pursuing a graduate degree in veterinarian medicine at the time. In 2006, after two years of studies at Iowa State University, he moved with Professor Tsukruk to Georgia Institute of Technology, where he pursued a Ph.D. in Polymer Engineering at the School of Polymer, Textile and Fiber Engineering. Stephanie and Michael were married on May 12, 2007 and had a daughter, Madeline Joy Leone McConney on June 4, 2008. Michael will begin a job working for Dr. Timothy Bunning in the Materials Directorate at Wright-Patterson Air Force Base in Dayton, Ohio as a post-doctorate in August 2009.